Analysis and Optimization of Stress Wave Propagation in Two-Dimensional Granular Crystals with Defects

Thesis by

Ivan Michel Nicolas Szelengowicz

In Partial Fulfillment of the Requirements
for the Degree of
Doctor of Philosophy

California Institute of Technology
Pasadena, California

2013
(Defended April 24, 2013)

To my family and friends.

Acknowledgements

A PhD is hardly the work of a single person and it is with great pleasure that I thank the people who were next to me, physically and in spirit, in this adventure.

I would first like to acknowledge and thank my advisor and mentor, Chiara Daraio. Chiara, I am forever grateful that you believed in me and gave me all these chances. I have learned many things from you, both as a scientist and a human being. Thank you for making these past five years possible, thank you for your endless excitement and your effortless ability to communicate it to the people around you. It was a pleasure to be part of your group and I greatly appreciate the guidance, freedom and support that you generously gave me.

I thank the members of my thesis committee: Guruswami Ravichandran, Oscar Bruno and Dennis Kochmann. I also thank the members of my candidacy committee: Guruswami Ravichandran, Michael Ortiz, and Oscar Bruno.

I would like to thank Caltech and the GALCIT for welcoming me and providing all the resources that directly and indirectly helped me carry out this work. It was both impressive and an honor to be part of this intensely creative community. I cannot forget to thank Joe Haggerty, Brad St. John, and Ali Kiani, Linda Miranda, Christine Ramirez, and Jennifer Stevenson for always coming through for me when I needed your help.

I thank my collaborators: Mariana Silva, Dan Tortorelli, Arif Hasan, Yuli Starosvetski, Alexander Vakakis, Panayotis Kevrekidis, Fernando Fraternali and Nancy Wu. Mariana, thank you so much for all the time that you spent working with me and teaching me, your patience, and your smile. You are a great mentor and I greatly appreciate your collaboration. I thank all the people who welcomed me when I was

visiting U.I.U.C.

My deepest graditude goes to my best friends at Caltech: Esperanza Linares, Michio Inoue, Vahe Gabuchian, Andrea Leonard, and Joseph Lyndon. Michio, Vahe and Esperanza, you were great companions during the Masters year (and after) and I wish we could spend more time together. Andrea, we started and finished this PhD program together, and my experience would have been a lot different without you. Thank you for so many good memories. Joseph, your energy and positive attitude grew on me and I consider you a great friend. I enjoyed very much being your roommate for a short but eventfull three months. Do not give up climbing please!

I thank my officemates and the Daraio lab group members, in particular: Terry Gdoutos, Nick Boechler, Paul Anzel, Hayden Burgoyne, Jordan Raney, Jinkyu Yang, Sebastian Liska, Duc Ngo, Georgios Theocharis, Namiko Yamamoto, Carly Donahue, Ludovica Lattanzi, Stephane Griffiths, Abha Misra, Claudio Silvestro and Devvrath Khatri.

Thank you Thomas Coquil for being such a good friend and for never failing to ask for news when I'm so bad at sending any myself. I wish you could have stayed in California longer. Thank you Lou Valentini for a much needed correspondence. I would love to fast foward time a few years and see where you are in your life. Thank you to all the people who decided to occupy my thoughts from abroad and made me smile: in particular Coline Gauci, Pauline and Clemence Sinault.

Thank you to the amazing people that I met in California who made me want to stay: Dan Coatta, Colin Parker, Colin Loveness, Ryan Tomaz, Pru Thein, Antha Mack, Shazam Rahmanian, Maaaax Cederroth, Keane Anderson, Melani Garcia-Stutedja and Brian Cornelius . The Cocolins, you are wonderful friends and I would have too much to say to even start here. Ryan, you know what I think of you, and I still remember exactly how I felt after “Whodunit”. Max, you are just awesome. Wether it is about science, nature, the mind or the meaning of your life, I love the fact that you all are extremely curious people and you inspired me.

To Jeannette Torres, you have been of so much support during this last year. Thank you for being here for me and for keeping it real. I cannot wait to see you succeed and live the life that you want, you certainly deserve it.

From far away but with much love, I thank my little sister Chloé, my mom, and my dad, who always have been supportive in all my endeavours. I am aware that Life has maybe been a little nicer to me than it has been to you and hope that you will recognize this achievement as a direct success of yours too. Chloé, ma petite soeur, je suis chanceux de t'avoir et je suis fier de toi. Maman, Papa, vous ne pouvez pas savoir à quel point il est important pour moi de vous savoir chacun heureux. Merci d'être là pour moi.

Abstract

Granular crystals are compact periodic assemblies of elastic particles in Hertzian contact whose dynamic response can be tuned from strongly nonlinear to linear by the addition of a static precompression force. This unique feature allows for a wide range of studies that include the investigation of new fundamental nonlinear phenomena in discrete systems such as solitary waves, shock waves, discrete breathers and other defect modes. In the absence of precompression, a particularly interesting property of these systems is their ability to support the formation and propagation of spatially localized soliton-like waves with highly tunable properties. The wealth of parameters one can modify (particle size, geometry and material properties, periodicity of the crystal, presence of a static force, type of excitation, etc.) makes them ideal candidates for the design of new materials for practical applications. This thesis describes several ways to optimally control and tailor the propagation of stress waves in granular crystals through the use of heterogeneities (interstitial defect particles and material heterogeneities) in otherwise perfectly ordered systems. We focus on uncompressed two-dimensional granular crystals with interstitial spherical intruders and composite hexagonal packings and study their dynamic response using a combination of experimental, numerical and analytical techniques. We first investigate the interaction of defect particles with a solitary wave and utilize this fundamental knowledge in the optimal design of novel composite wave guides, shock or vibration absorbers obtained using gradient-based optimization methods.

Contents

List of Figures

List of Tables

Chapter 1

Introduction

The work presented in this thesis describes new ways to control and tailor the mechanical energy associated with the propagation of stress waves in granular crystals through the optimal use of heterogeneities (interstitial defect particles, material heterogeneities) in otherwise perfectly ordered systems. We primarily focus on square packed two-dimensional (2D) granular crystals with interstitial spherical intruders and composite hexagonal packings. In this introduction, we describe the motivation behind this work, our goals and achievements, provide a general description of granular crystals followed by a brief historical review of the previous work in the field, and finally present the organization of this thesis.

1.1 Motivation

Mechanical waves, defined as waves propagating through a medium, are omnipresent in our world and part of our daily lives. For instance, oscillations of a string and stress and seismic waves are common examples of mechanical waves. Their form varies and depends on the medium that hosts them (e.g., acoustic waves in fluids and elastic waves in solids). A large variety of different waves can also exist within a same medium: surface oscillations of a membrane, torsional wave in a cylindrical rod, or the various body and surface waves involved in the propagation of an earthquake. Present in the natural world, mechanical waves are also used in a wide range of engineering applications. It is consequently of great importance to understand their underlying mechanisms and to be able to control them.

Environmental forces such as wind or earthquakes acting on a structure or the simple walking or stomping of crowds in a building can cause unwanted vibrations potentially resulting in the damage or failure of the structure. Vibrations are sometimes directly associated with the functioning of an engineering device (e.g. vibrations in heavy machinery). Explosions, falls, or any source of shock creation can similarly damage a structure, object, or engineering device. These are a few of many applications for which the development of shock- and vibration-absorbing devices operating at macroscopic wavelenghts is crucial. Some of the most common ways currently used to mitigate shocks and vibrations include cushioning (including but not limited to the use of polymeric foams) [1], harmonic absorbers [2] and viscous dampers (as in a typical door closer for instance) among other examples. Most of these techniques are based on the passive methods of dissipating the wave energy (e.g., dampers), absorbing part of the wave energy (transmitted to tuned oscillating structures), or dispersing the wave energy between a wider range of frequencies.

Granular materials, defined as large conglomerations of discrete macroscopic particles have been widely used as passive devices for impact and vibration absorption [3]. Their strong absorbing power is based on the large number of inelastic (dissipative) collisions between neighboring grains and hence originates from a collective behavior of the particles. Examples of applications include packaging fillers, recoiless hammers or Hacky Sacks [4]. The properties of granular materials have been a subject of active research for centuries, and this goes back to Coulomb who initially stated his friction law for such materials. Faraday and Reynolds also took part in the initial development of this field [5, 6]. Their complicated static and dynamic behavior makes it impossible to attribute to them a single phase of matter as they combine properties reminiscent of solids, liquids and gas [4]. The physics of granular materials is still relatively poorly understood despite their being heavily represented both in nature and industrial applications (sand, cereals, rice, fertilizers, and ball bearings being only a few examples). The behavior of disordered granular materials is distinct from granular crystals, a subcategory defined as compact arrays of elastic particles in contact.

Granular crystals are nonlinear lattices, and have been an area of intense research ever since they have been shown to support the formation and propagation of a new type of solitary wave [7], among other unique properties. The main advantage of working with granular crystals as opposed to "random" comglomerations of particles is the possibilty to take advantage of their interesting dynamics in a controlled and optimal fashion, leading to the design of new engineered materials with potentially application-specific properties, as evidenced in [8–12] for example.

In this thesis, we investigate new ways to control the wave propagation in granular crystals by the progressive inclusion of heterogeneities and by taking advantage of their dispersing abilities. We make use of multi-disciplinary optimization techniques originally developed for structural optimization and compliance minimization problems [13] in the last 30 years, which are now widely used in the aeronautical, car and turbomachinery industries. The discoveries and methods presented in this thesis will help to develop practical crystal-based devices and are expected be applicable to more complex or analogous settings (3D granular crystals, different dynamical regimes or in other discrete nonlinear systems).

1.2 Goals and achievements

This section summarizes the objectives pursued in this study. As part of this thesis, we developed ad-hoc experimental and numerical techniques combined with simple analytical models. We applied these approaches to the analysis and characterization of new phenomena occuring in compact 2D assemblies of spherical particles. The main goals of this work were to:

- gain a fundamental understanding of the effect of a single defect particle and its interaction with a solitary wave, and investigate the mechanisms of interaction of several defects;

- apply this fundamental knowledge to the numerical design of complex composite materials via optimization techniques;

- extend the study to a different kind of inhomogeneity introduced by material mismatch;
- assess the performance of both the designs and the method;
- evaluate the feasibility of the practical implementation of our results through experimental validation.

The effect of impurities in linear media is well understood. P.W. Anderson showed in his landmark publication [14] the absence of diffusion in an impure linear medium provided that the degree of randomness of the impurities is sufficiently large, and explained the relation of disorder to strong localization. Several studies focused on the presence of defects in 1D granular crystals [15–18]. In weakly nonlinear 1D granular crystals, Theocharis et al. showed that the inclusion of light mass intruders is necessary to observe energy localization under the form of discrete breathers (extrinsic localization through disorder) [18]. In highly nonlinear crystals, defect particles have been shown to localize energy when interacting with a solitary wave [15]. When reached by a shock wave [17], a light intruder acts as a secondary source of solitary waves, whereas a heavy one will be shifted by the shock and causes the transmission of a train of waves of decreasing amplitudes.

Here, we conducted systematic numerical simulations and experiments to investigate the effect of the material properties (elastic modulus and mass) of an interstitial spherical intruder placed in the center of a 2D square packing submitted to an impact. The number of intruders was progressively increased to study the interaction of two intruders and we showed that one can effectively transfer half of the impact energy into the chain adjacent to the one impacted through the nonlinear coupling introduced by a line of intruders, passively redistributing half of the impact energy into different areas of the crystal.

We extended this work to the study of the optimal placement of an arbitrary numbers of defects into the same 2D granular crystal and the obtention of wave mitigating and wave redirecting designs able to minimize or maximize the energy or reaction force reaching a given part of the crystal. A gradient-based topology optimization was developed in order to solve these optimization problems, building on the first step made towards the design of optimal granular crystals realized in [9].

The same method was adapted to the problem of material optimization in 2D hexagonal packings and the design of optimized crystals in which every particle can be made of either a soft or a stiff phase. The energy dispersion taking place in the crystal is due in this case to a material property mismatch responsible for the progressive decomposition of an initial pulse into a train of waves, as previously investigated in 1D crystals for mass defects for example [7]. We established that the numerical designs are much more effective at dispersing or focusing the input energy than the analogous homogeneous crystals and other disordered configurations.

Several optimization methods were available which can be categorized into two families:

- gradient-based methods employing local search strategies and termination criteria;
- heuristic (also refered to as population or non gradient-based) methods.

A breeder genetic algorithm (BGA), heuristic method that uses selection schemes inspired from natural selection and breeding [19], was chosen in an earlier work [9]. The advantages and shortcomings of the gradient-based methods over the heuristic ones are discussed in [20]. In this thesis, we compared the designs of selected granular crystals obtained using a BGA and a gradient-based scheme and justified the choice of the selected gradient-based scheme based on computational efficiency and performance of the optimized design (see details in chapter 6 of this thesis).

For practical applications, it was important to be able to reproduce the numerical results in real systems. To this end, and as will be described in detail in the next chapter, we designed several experimental setups as well as a measurement technique allowing us to directly and successfully compare the acceleration of any particle in the real crystal to the numerical signals.

1.3 Granular Crystals

Granular crystals are compact arrays of elastic particles in contact and can be modeled as point masses interacting nonlinearly via the so-called Hertzian potential (see Eq. 1.1). They arguably are the most important example of the Fermi-Pasta-Ulam class of nonlinear lattices (a review of the studies of the principal nonlinear lattices, Discrete Nonlinear Schrödinger Equation, Klein-Gordon and Fermi-Pasta-Ulam can be found in [21]). The next sections focus on the origin of nonlinearity in these systems, how it affects the dynamics of organized assemblies of spherical particles (we base our explanation on the theory initially developed by Nesterenko for 1D homogeneous crystals [7]) and give an overview of the previous works carried out on granular crystals in the past 30 years.

1.3.1 Hertzian Contact and Nonlinearity

Hertzian contact relates the compression force F_{ij} between two spherical particles i and j to their relative displacement δ_{ij} as follows:

$$F_{ij} = A_{i,j}[\delta_{ij}]_+^{3/2}, \tag{1.1}$$

where $[X]_+$ denotes the positive part of X.

It is important to point out that this dependance of F in the form $\delta^{3/2}$ is valid for contacts between bodies of different shapes (not necessarily spherical) [22].

For the specific case of spherical particles, $A_{i,j} = \frac{4E_iE_j\sqrt{R_iR_j/(R_i+R_j)}}{3\left(E_i\left(1-\nu_j^2\right)+E_j\left(1-\nu_i^2\right)\right)}$. E_i, ν_i, R_i represent the Young's modulus, Poisson's ratio and radius of particle i respectively.

The above interaction law is valid for linear elastic particles with elliptical contact area, and the following assumptions were made by Hertz in its original derivation [23, 24]:

1. the contact area is small with respect to the radii of curvature of each particle,

2. the contact surface is frictionless and only supports forces normal to it,

3. the interaction is quasi-static (i.e. the characteristic time of the problem is much longer than the oscillation period of a particle).

The validity of the Hertz law for spheres of different materials is discussed in detail in [24, 25] as well as more recently in [26] and was confirmed for a range of materials including tungsten carbide, steel, brass, glass and nylon.

The nonlinearity in this case arises from the geometry of the contact and the dramatic increase of the contact area with the compression force. The $3/2$ power law is softer than the harmonic case for small overlaps but becomes rapidly steeper as compression increases, which makes it energetically expensive to sustain contact for too long. Another unusual feature of granular crystals is the absence of tensile strength which introduces an additional nonlinearity by breaking the symmetry of the potential.

It is this intrinsic nonlinearity of the contact interaction that explains the nonlinearity of the granular crystals described in this thesis. These systems have drawn considerable attention during the past years and this broad interest has emerged, to a considerable extent, due to the unique ability to tune their dynamic response from linear to essentially nonlinear by the addition of a static precompression force, as will be described in the next section. This remarkable feature, along with the wide variety of shapes, sizes and materials that one can consider, has allowed for a wide range of studies that include the investigation of fundamental nonlinear phenomena in discrete systems such as solitary waves [3, 27], shock waves [28], discrete breathers [29, 30] and defect modes [18] or the design of new materials for practical engineering applications.

1.3.2 Dynamical Regimes and Example of the 1D Homogeneous Chain

The mathematical development of such systems is still relatively limited and we focus in this section on the simplest granular crystal that one can encounter. The case of a 1D chain of identical spheres was first investigated by Nesterenko [7] and is described in detail in [3]. Because the stiffness of each contact is much lower than the bulk stiffness of the particles composing the crystal, we can model it by a spring-mass system and using the expression for the force from Eq. 1.1 write the particle equation of motion:

$$\ddot{u} = \frac{A}{m}[(\delta_0 - u_i + u_{i+1})^{3/2} - (\delta_0 - u_{i+1} + u_i)^{3/2}], \tag{1.2}$$

with $A = \frac{\sqrt{2R}E}{3(1-\nu^2)}$. We denote by m, R, E and ν the mass, radius, elastic modulus and Poisson's ratio of a particle respectively, u_i represents the displacement of particle i, and δ_0 is the initial displacement caused by the applied precompression force F_0 (see Fig. 1.1).

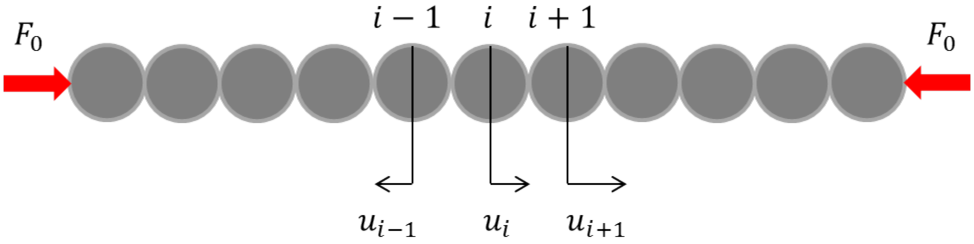

Figure 1.1: 1D homogeneous chain of spherical particles statically precompressed.

For a strongly compressed chain the dynamic displacement of a particle is small with respect to the one caused by the static precompression, $\frac{|u_{i+1}-u_i|}{\delta_0} << 1$, and one can expand Eq. 1.2 into an anharmonic approximation [7]. Further assuming that the characteristic spatial size of the propagating perturbation is large with respect to the size of a particle (long wavelength approximation), it is possible to show that the dynamics of these systems is described by the Korteweg-de Vries (KdV) nonlinear wave equation [31] of which Russel's soliton [32] was later proved to be a solution for the strain $\xi = -u_x$:

$$\xi_t + c_0\xi_x + \gamma\xi_{xxx} + \frac{\sigma}{2c_0}\xi\xi_x = 0, \tag{1.3}$$

where $c_0^2 = 6\frac{A}{m}\sqrt{\delta_0}R^2$, $\gamma = \frac{c_0R^2}{6}$ and $\sigma = \frac{c_0^2R}{\delta_0}$.

They are usually qualified as weakly nonlinear as the wave equation contains both a linear part and a nonlinear part. When the compression load is much greater than any disturbance, the crystal becomes fully linear and one can derive its classical dispersion relation [33]. Physically, one can understand it as the creation by the static load of a continuous channel along the chain of beads in which small sound oscillations can propagate.

However, when the compression load becomes of the order of the dynamic forces created by the propagating signal ($\frac{|u_{i+1}-u_i|}{\delta_0} \gtrsim 1$), a completely new highly nonlinear regime describes the behavior of the granular crystal. The approach taken by Neserenko in 1983 consisted of applying the long wavelength approximation previously mentioned and expanding the displacement of particle $i-1$ and $i+1$ as a function of u, displacement of particle i, and its space derivatives:

$$u_{i\pm 1} = u \pm \frac{2R}{1!}u_x + \frac{(2R)^2}{2!}u_{xx} \mp \frac{(2R)^3}{3!}u_{xxx} + \frac{(2R)^4}{4!}u_{xxxx}\ldots \tag{1.4}$$

Replacing each term in Eq. 1.2, he obtained the strongly nonlinear wave equation:

$$u_{tt} = -c^2\left[(-u_x)^{3/2} + \frac{a^2}{10}\left[(-u_x)^{1/4}\left((-u_x)^{5/4}\right)_{xx}\right]\right]_x, \tag{1.5}$$

with $c^2 = \frac{2E}{\pi\rho_0(1-\nu^2)}$ and $a = 2R$, for which he found an exact stationary solution (i.e. solution of the form $u(x-Vt)$):

$$\xi = \left(\frac{5V^2}{4c^2}\right)^2 \cos^4\left(\frac{\sqrt{10}}{5a}(x-Vt)\right). \tag{1.6}$$

V is the velocity of the highly nonlinear solitary wave. Unlike harmonic waves traveling in linear media, the velocity of a solitary wave depends on its amplitude, and larger amplitude waves move faster than those with smaller amplitudes [34]. In this specific case, the wave velocity is nonlinearly related to the ratio of the maximum dynamic contact force F_d divided by the static preload F_0, noted f_r:

$$V = 0.9314\left(\frac{4E^2F_0}{a^2\rho^3(1-\nu^2)^2}\right)^{1/6}\frac{1}{f_r^{2/3}-1}\left(\frac{4}{15}\left[3+2f_r^{5/3}-5f_r^{2/3}\right]\right)^{1/2}, \tag{1.7}$$

which simplifies to the well known relation:

$$V = 0.6802 \left(\frac{2E}{a\rho^{3/2}(1-\nu^2)} \right)^{1/3} F_d^{1/6}, \tag{1.8}$$

which expresses the weak dependance of the phase velocity of the solitary on its amplitude in the absence of static preload ($F_0 = 0$) [35].

1.3.3 Historical Review

1.3.3.1 1D Granular Crystals

The study of packed granular crystals was initiated by Nesterenko in 1983 when he theoretically and numerically predicted the existence of a new kind of highly nonlinear soliton-like wave in uncompressed 1D homogeneous granular crystals [7] that otherwise do not support the propagation of sound vibrations (appropriately naming them "sonic-vacua"). Experimental confirmation of these new phenomena was provided soon after in a subsequent study carried out with Lazaridi [36]. Following his pioneering work, he published several other studies related to solitary wave and shock propagation in these systems, looking at phenomena such as the transmission of solitary waves at the interface between two granular crystals, the effect of the randomization of the radii of the particles or the thermalization of impulses, which are described in his book "Dynamics of Heterogeneous Materials" [3]. Granular crystals, and the phenomena occuring in them not only in the highly nonlinear regime, but also in the weakly nonlinear or linear regimes, have since then received considerable attention and are today an extremely active area of research.

The initial derivation, which approach is described in the previous section, was extended to homogeneous systems with the general nonlinear interaction $F \alpha \delta^n$ [3] and later to heterogenous diatomic crystals [37, 38]. MacKay published a rigorous mathematical proof of the existence of the predicted solitary wave [39] based on the existence theorem of Friesecke and Wattis for localized traveling waves in 1D lattices with nearest-neighbor interactions [40]. This proof was later extended to the general case of arbitrary power-law type contact interaction [41]. Other approaches were also taken: A. Chatterjee, for instance, developed an asymptotic solution for the solitary wave [42] and S. Sen derived an iteratively exact solution [43] with better accuracy than the original approximate solution.

In the early 1990's, a few studies using experimental techniques focused on sound propagation in sand [44, 45], a granular material far more complex than granular crystals due to the complexity of the individual properties of each grain. For the ideal case of 1D granular crystals submitted to a static force, Hertz theory predicts that the sound speed is related to the pressure in the chain by the following relation: $c_0 \, \alpha \, P^{1/6}$. When studying 3D pilings, Goddard observed deviations from the Hertzian behavior ($c_0 \, \alpha \, P^{1/4}$) and attributed them to the presence of roughness in real systems, conical interactions or the possible buckling of the chains [46]. De Gennes developed models taking into account the effect of a small oxide layer [47] and plasticity at the microcontacts [48] that both give the value 1/4 for the power-law relation sound speed and pressure. Coste and Gilles reviewed alternate models to the Hertz theory and showed with experiments that the propagation of waves in highly nonlinear and precompressed (weakly nonlinear) 1D granular crystals was in agreement with the Hertzian theory for a wide range of materials (elastic, elastic-plastic, oxidized, varying the roughness among other factors) [26].

S. Sen and collaborators studied the vertical propagation of weak and strong impulses in deep gravitationally loaded granular columns [49, 50] and studied the formation, propagation and crossing of solitary waves in 1D highly nonlinear crystals [51–53]. Several other studies consisted of numerical investigations of the interaction of a solitary wave with a mass defect with potential applications for detecting burried impurities [53–55] (E. Hascoët and H. Herrmann numerically studied the related problem of the interaction of a shock impulse with a mass defect in an unloaded 1D granular chain [17]) . They provided the first study of tapered chains using numerical simulations and suggested that these systems could be used as efficient granular protectors able to thermalize impulses by breaking them down into trains of waves of lower amplitude [56]. This early work motivated a series of publications focusing on analytical, numerical and experimental studies of uncompressed tapered chains, some based on the independent-collision model of D. Wu [10, 57–61]. J. Hong and collaborators also studied gravitationally loaded 1D chains [62] and revisited the idea of identifying impurities by observing the signal backscattered from light or heavy defects [63]. His later work consists of a numerical study in which he demonstrates the power-law decay of impulses traveling in uncompressed "granular containers" composed of granules of different shapes and masses, making them excellent candidates for new granular protectors [12].

C. Coste and collaborators analytically studied highly nonlinear 1D granular chains and provided one of the earliest experimental verifications of the formation of solitary waves in these crystals [27].

More recently, S. Job and collaborators studied different aspects of the propagation of highly nonlinear solitary waves in 1D granular crystals. They performed experiments, numerical analyses and analytical techniques to describe the interaction of a solitary wave with a boundary [64], with a mass defect [15], and at an interface between two granular crystals [65] and studied the effect of a viscous fluid surrounding the contacts [65] (in addition to the work on tapered chains previously mentioned [60]).

K. Lindenberg and collaborators published several studies describing the response of uncompressed 1D granular crystals through models including friction [66] and dissipation [67] and developed a binary collision model in which the transfer of energy along the chain is assumed to occur via a succession of two-particle collisions [68], applied to the analysis of tapered and decorated chains [69, 70].

Additionally, it was shown that homogeneous granular media can support families of strongly nonlinear traveling and standing waves [71], whereas heterogeneous media can exhibit resonance and anti-resonance phenomena [72].

As one can see, extensive work has been carried out relating to highly nonlinear 1D granular crystals, the propagation of highly nonlinear solitary waves or shocks and the effect of impurities, interfaces or boundaries. This was continued by C. Daraio and collaborators who investigated with numerical simulations and experiments the propagation of highly nonlinear solitary waves in 1D chains of PTFE or polymer coated steel particles [73, 74], their tunability [35], the propagation of solitary waves in periodic crystals of higher dimensionality [37, 38], the coupling of highly nonlinear solitary waves with a linear elastic medium [75] and the effect of dissipation on the propagation of solitary waves [76]. Specific studies focused on how to better control the energy propagation in 1D granular crystals by taking advantage of properties specific to these systems, such as the anomalous reflection phenomenon occuring at the interface of two 1D granular crystals [8], the ability to trap energy in a soft section of a 1D crystal [11], the splitting and recombination of pulses in y-shaped crystals [77] (with numerous potential engineering applications including new shock absorbing devices [9, 11], sound scramblers [8, 73], actuator devices [75] or acoustic lenses [78]).

More recently, increased attention was given to the study of 1D granular crystals when operating in the linear or weakly nonlinear regime. Using concepts from linear dynamics, several studies experimentally and numerically investigated highly compressed (linearized) 1D granular crystals, the existence of band gaps in their dispersion relation, and the possibility of tuning them [33, 79–82]. Intrinsic localized modes or discrete breathers, originally theoretically predicted to exist in anharmonic lattices [83–86], are time-periodic, spatially localized (typically exponentially) solutions numerically and experimentally observable in weakly nonlinear crystals (see for example the studies realized on monoatomic crystals with defect [18] in which nonlinear breathing modes were obtained as a continuation of the linear modes induced by the presence of such defects, diatomic crystals [29] or at the interface between a monoatomic and diatomic crystal [87]). Understanding these phenomena and the localization of energy in crystals is important to further the understanding of the nonlinearity of these systems and could lead to the design of novel energy-harvesting or filtering devices [88, 89].

1.3.3.2 2D Granular Crystals

The study of higher dimension (2D and 3D) granular crystals is far less developed and no general theoretical framework is yet available. The investigation of 2D and 3D granular crystals is experimentally challenging due in large part to the difficulty of assembling "perfect" crystals: a slight tolerance on the radius of the particles can disrupt the contact network by creating local precompressions or gaps. A. Shukla and collaborators performed some of the earliest experimental work on 1D and 2D uncompressed crystals using photoelasticity techniques combined with high speed photography [90, 91] and qualitatively looked at various aspect of the wave propagation in assemblies of photoelastic disks and elliptical beads including the effect of the packing geometry [92], the role of the shape of the particle [93], and the presence of cracks in the particles [94]. S.G. Bardenhagen and J. U. Brackbill performed numerical experiments to investigate the stress localization in 2D square packings of polydisperse cylinders, comparing static and dynamic loading, and looked at the effect of an interstitial material [95]. In 2002 B. Velický and C. Caroli provided a theoretical mean-field description of 2D hexagonal crystals composed of Hertz-Mindlin balls [96] whose diameters exhibit mild dispersion, and studied the dependence of an external pressure field on the sound velocity [97]. Soon after, C. Coste and B. Gilles conducted some of the earliest numerical and experimental studies on wave propagation in highly compressed 2D hexagonal packed granular crystals [98, 99], looking at the effect of the strength of the static prestress on the behavior (Hertzian or non-Hertzian) of the system and interpreted the recovery of the Hertzian behavior at high stress in terms of the progressive activation of contacts. M. Nishida and collaborators investigated the absorbing abilities of 2D layered granular crystals using Discrete Element Method (DEM) simulations and experiments [100, 101].

Very recently, Leonard and Daraio used numerical and experimental techniques to describe the wave propagation in 2D uniform square packings (pseudo-1D systems) and observed the formation and propagation of highly nonlinear solitary waves [102]. In a subsequent study, they showed how cylindrical intruders and their material properties affect the shape of the 2D wave front [103].

While much work has been done on 1D highly nonlinear granular crystals (including the interaction of solitary waves with defects), and some on 1D weakly nonlinear or linear granular crystals, the behavior of higher dimension crystals, both submitted to a static precompression force or in the highly nonlinear regime, is still relatively poorly understood. This thesis will focus on uncompressed homogeneous and heterogeneous 2D granular crystals and several phenomena related to the presence of defect particles in otherwise perfectly organized packings.

1.4 Conceptual Organization of This Thesis

The remainder of the thesis is organized as follows: in chapter 2, we describe in detail the various experimental and numerical setups developed and used to carry out the projects presented in the next chapters.

In chapter 3 we investigate the effect of spherical interstitial intruders placed in a 2D uncompressed square packing on the wave propagation. We show the first experimental and numerical demonstration of the dispersion caused by one spherical intruder, study how its scattering power is related to its material properties (stiffness principally) and look at the interaction of two spherical intruders depending on their relative positions in the packing. Analytical rigid body collision models were derived that corroborate the experimental and numerical results.

Chapter 4 presents a continuation of this work where we show with experiments and simulations how a line of light spherical intruders redistributes the energy input in the impacted chain into the adjacent chain until an equilibrium is reached where two signals of same amplitude travel down the two chains (this is the first observation of an equipartition phenomenon in a nonlinear granular crystal). This fully 2D system is compared with a simplified 1.5D system in which the transverse motions of the particles are neglected.

In chapter 5, we apply a gradient-based optimization method to the design of novel granular materials in which the positions (topology optimization) and material properties (material optimization) of the particles are optimized in order to best mitigate, redirect or focus the impact energy. We first optimize the locations of stiff interstitial intruders in 2D square packings and optimize the material properties of each bead in a hexagonal packing. A wide range of optimization methods are available to perform such optimizations which can be divided into two families: gradient-based and non gradient-based (or heuristic), with specific advantages and inconveniences (discreteness of the solutions, implementation, computational time, required knowledge of the design space etc.).

In the numerical work of chapter 6, we compare two conceptually different approaches: we apply a Breeder Genetic Algorithm to some of the problems investigated in chapter 5 and mainly focus on the performance of the optimized designs obtained via each method as well as the computational times required in each case.

Chapter 2

Experimental and Numerical Setups

2.1 Experimental Setups

Several experimental setups were designed to test the dynamic response of uncompressed 2D granular crystals arranged in square and hexagonal configurations. When studying square packings, custom-made intruder particles were located in some of the interstitial sites. The particles composing the granular crystals are $R = 9.52$ mm $\pm\, 0.01$ mm radius particles made of 316 stainless steel or polytetrafluoroethylene (PTFE). The spherical intruders are custom-made particles provided by [104] and have radius $Rd = 3.943$ mm $\pm\, 0.001$ mm (note that $Rd \approx \left(\sqrt{2}-1\right) R$) in order to fit exactly in the interstitial sites: each intruder particle is barely in contact with all of its four neighbors. Four different materials were investigated to study the effect of the stiffness of such spherical intruders: PTFE, 260 alloy brass, 316 stainless steel and tungsten carbide (TC).

Even though the particle configurations and the materials used are different for each experiment, the measurement method and the experimental procedure are the same in each case, and the different setups share common features. A steel particle of radius R and initial velocity v_0 (typically in the [0 m/s ; 0.25 m/s] range) impacts the granular crystal on one side, and the acceleration-time history of the propagating excitations is visualized using calibrated custom-made sensor particles consisting of a

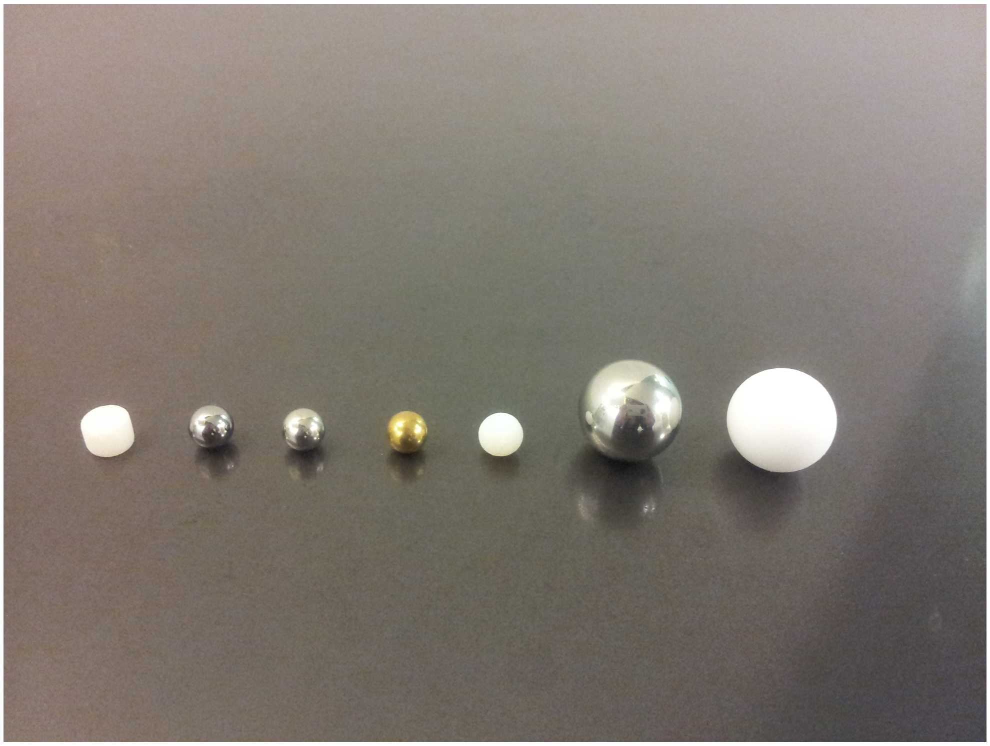

Figure 2.1: Particles used in the various experiments. From left to right: PTFE cylindrical stand, tungsten carbide 3.943 mm radius spherical intruder, steel 3.943 mm radius spherical intruder, brass 3.943 mm radius spherical intruder, PTFE 3.943 mm radius spherical intruder, steel 9.52 mm radius and PTFE 9.52 mm radius.

	TC	stainless steel	brass	PTFE
(kg/m^3) ρ	15800	8000	8500	2200
(GPa) E	400	193	103	1.26
ν	0.28	0.30	0.37	0.46

Table 2.1: Densities, Young's moduli and Poissons's ratios of the different materials used in our experiments and numerical simulations.

triaxial accelerometer embedded in a spherical particle placed in a location of interest in the crystal. The impact velocity is measured using an optical interruptor connected to an oscilloscope (TEKTRONIC 2024B) and the experimental impact velocity is used as an input for the numerical simulations. The acceleration data is sent to a signal conditioner (PCB 481A02) and a data acquisition board (NI BNC-2110 and NI PCI-6123) and passed to MATLAB (R2010a) for post-processing and visualization. The boundaries ("walls") and supporting plane are made of a polymer (PTFE or Delrin for the walls, polycarbonate for the supporting plane) or coated with a PTFE layer. Polymers were chosen (over metals) for several reasons. First of all, the reflection of a solitary wave against a soft wall will be delayed (if compared with a stiffer wall) due to the longer time needed for the last stiff particle to penetrate the wall. This is important as we do not consider reflected signals in this work and hence want to minimize boundary effects. Another reason is that they have a low coefficient of friction in contact with the particles composing the crystal which diminishes the role of dissipation caused by dry friction. Lastly, they are electrically insulating which prevents cross-talk between sensor particles.

The following sections describe in further detail the various experimental setups, sensor particles and data acquisition equipment.

2.1.1 Square Packings, Equipartition Experiment and Hexagonal Packings

2.1.1.1 Experimental Setup 1: Square Packing

A first experimental setup was designed to investigate the propagation of stress waves in a 2D square packing with defect particles. It is presented in Fig. 2.2. The setup was designed to be adjustable and can accomodate many different granular crystal configurations and sizes. One can vary the particle type and size, and the location of the impact site and sensor particles. It is composed of a flat polycarbonate base (square base 762 × 762 mm^2, thickness 12.7 mm) and four movable delrin walls (length 584 mm, height 50.8 mm, thickness 25.4 mm) to support and enclose the packing.

All four walls can slide along their length and two of them can also be adjusted in the direction perpendicular to their length. An opening (25.4 mm diameter circular opening) was machined in one of them in order to impact the crystal. Typically, packings of 20 × 20 stainless steel particles (nonmagnetic, 316 type) were assembled, which is sufficiently large to ensure the formation of stable solitary pulses [3, 105] as well as avoiding boundary effects. For the experiments presented in chapters 3,4 and 5, custom-made PTFE cylindrical stands (radius $Rd = 3.943$ mm, height 5.58 mm) were designed to support the small defect particles in order to have the centers of mass of all the particles (square packing and interstitial defects) in the same horizontal plane. PTFE was selected in order to minimize friction between the stands and the intruders.

2.1.1.2 Experimental Setup 2: Equipartition

For some of the equipartition experiments presented in chapter 4, a longer setup was needed that exceeds the maximum capacity of the previous one and requires only two rows of particles. A modular setup was designed and is shown in Fig. 2.3. It was designed using SolidWorks and printed using the Objet Connex 500 3D printer available at the GALCIT facilities. We selected the printing material "Vero White" which is the stiffest polymer available and coated the surfaces in contact with the particles with a PTFE layer. Each part consists of a channel of width 38.1 mm, depth 19.05 mm, length 45.72 mm and a line of cylindrical stands of radius $Rd = 3.943$ mm and height 5.580 mm, $2R = 38.1$ mm apart from each other on the center line of the channel. Each module can contain 2 × 24 particles of radius R and several modules can be connected to each other to attain any desired length.

2.1.1.3 Experimental Setup 3: Hexagonal Packing

Finally, a third experimental setup was designed and printed to assemble the hexagonal packings studied in chapters 5 and 6. It is shown in Fig. 2.4 and consists of a hexagonal wall ($10R = 9.52$ cm per side, height 31.75 mm, thickness 25.4 mm) that encloses a hexagonal packing of 61 $2R$ diameter particles (five particles per side). The wall is made of “Vero Clear”, material possessing properties similar to “Vero White”, coated with PTFE and has a circular opening (25.4 mm diameter) located at the center of one of the faces for impact.

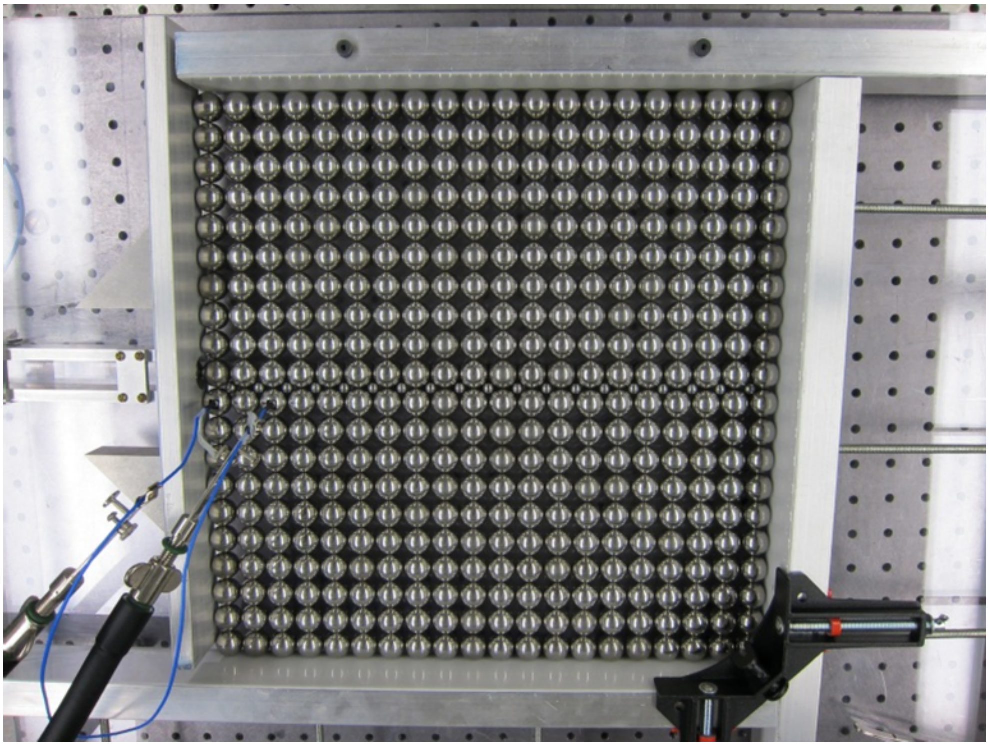

Figure 2.2: Experimental setup designed for 2D granular crystals (chapters 3, 4 and 5).

2.1.2 Custom-Made Accelerometer Sensors

Previous experiments on 1D crystals measured the 1D force component applied on a sphere using piezoelectric disks embedded into two half particles [15, 35, 73] or measured the response at the edge of the granular crystal with force sensors [27, 36]. The latter technique was also used in the study of 2D granular crystals [99, 101] and other groups performed whole-field 2D measurements involving high speed photography and photoelastic particles [90, 93, 106].

We fabricated in-situ accelerometer sensors to quickly and accurately measure the response of individual particles in the granular crystal, as shown in Fig. 2.5. The

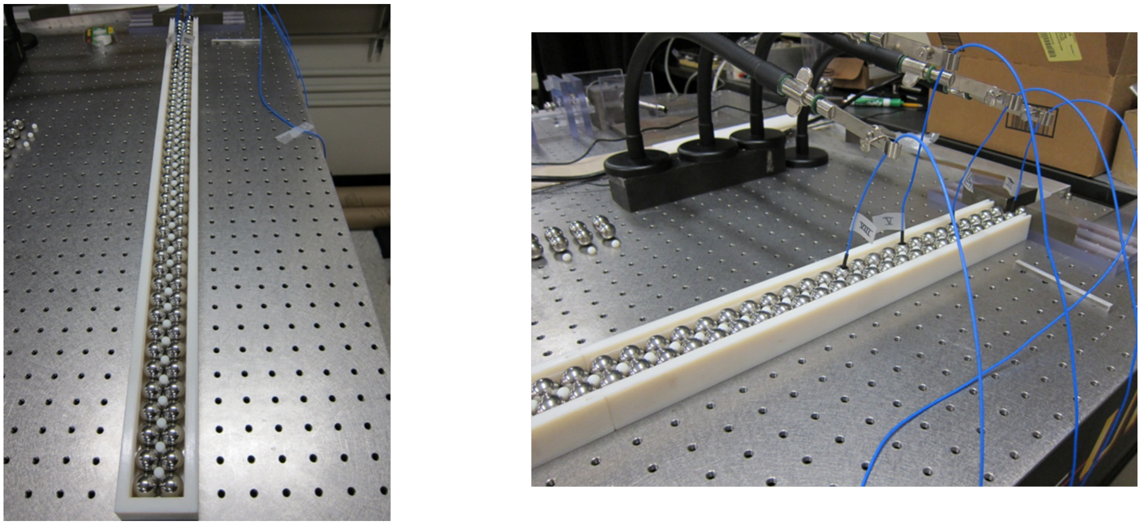

Figure 2.3: Experimental setup designed for the equipartition experiment (chapter 4).

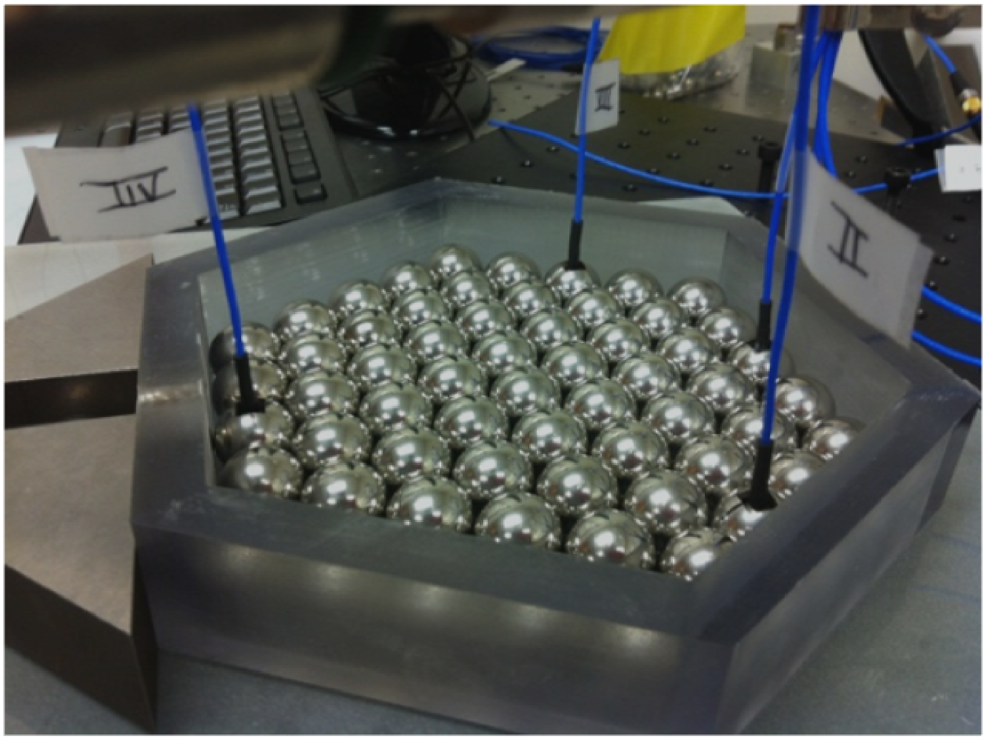

Figure 2.4: Experimental setup designed for the study of 2D hexagonal packings (chapters 5 and 6).

sensors are composed of a mini triaxial accelerometer (PCB Piezotronics 356A01, $6.35 \times 6.35 \times 6.35$ mm^3, sensitivity 0.51 mV/(m/s^2), commercially pre-calibrated) embedded in a particle in which a square hole was drilled. It was shown in [102] that the mass difference of the sensor particle does not significantly affect the wave propagation in the crystal as the small mass mismatch (26.52 g for the steel sensor particles versus 28.79 g for the solid steel particles in average) accounts for a signal amplitude mismatch of approximately 1%, potentially near the experimental noise level. The depth of the hole is 12.70 mm which ensures that the center of mass of the accelerometer coincides with the center of the original spherical particle and consequently avoids perturbations caused by the rotation of the particle. A stiff epoxy was used to glue the accelerometer into the drilled particle in order to maintain the bulk stiffness of the sensor particle. The resonant frequency of the accelerometer is $f_r = 50$ kHz and is well above the maximum frequency composing the measured pulses for our range of impact velocities ($F_{max} \approx 30$ kHz, measured taking the Fast Fourier Transform of a solitary wave propagating in a 1D granular crystal made of steel particles). It can measure signal frequencies as low as $F_{min} = 2$ Hz. This number should be compared to the lowest frequency component of our signal, which can be approximated by the inverse of the time width of a solitary wave $\frac{1}{\Delta t}$. The typical velocity of a solitary wave propagating in a 1D chain of 19.05 mm steel particles is around $v = 400$ m/s, and the space width of such a solitary wave is approximately five particles [7]. This yields $\Delta t = \frac{v}{10D} = 0.238$ ms in the time domain and consequently $\frac{1}{\Delta t} \approx 4$ kHz, which is much greater than F_{min}.

The vertical acceleration of the particles was not measured as we do not expect the propagating signals to have a non-zero component in the out-of-plane direction. Both in-plane directions of the accelerometer were aligned with the axes of reference of the numerical setups and we directly compared the numerical output acceleration with the experimental one. The next section describes in detail the method of acquiring the acceleration data.

Figure 2.5: In-situ accelerometer sensor. (left) Photograph of the accelerometer. (right) Photograph of a steel sensor particle (accelerometer embedded in a drilled steel sphere).

2.1.3 Data Acquisition and Post-Processing Apparatus

A Data Acquisition Board (DAQ board) was used to acquire the acceleration data. The sensor particles are connected to a signal conditioner (PCB Piezotronics 481A02) which powers the accelerometer and amplifies the signal at the source. The signal is then passed to a connector block (National Instrument BNC-2110) and a PCI card (National Instrument model PCI-6123) inside a PC driven by MATLAB via the Data Acquisition Toolbox. A schematic diagram of the assembly is presented in Fig. 2.6. The main factors involved in the selection of the DAQ board are the sampling frequency f_s which defines the maximum measurable frequency ($f_s/2$ given by the Nyquist criterion), and the number of analog inputs which determines the maximum number of sensors that can be placed in the experiment as well as the resolution of the converted digital signal. The DAQ board selected offers a 500 kS/s simultaneous sampling rate over eight channels with a 16 bits resolution.

The sampling frequency is high enough to avoid aliasing phenomena that cause frequency components above the Nyquist frequency to appear as low frequency components in the measured signal. A digital filter was used to cut off frequency content

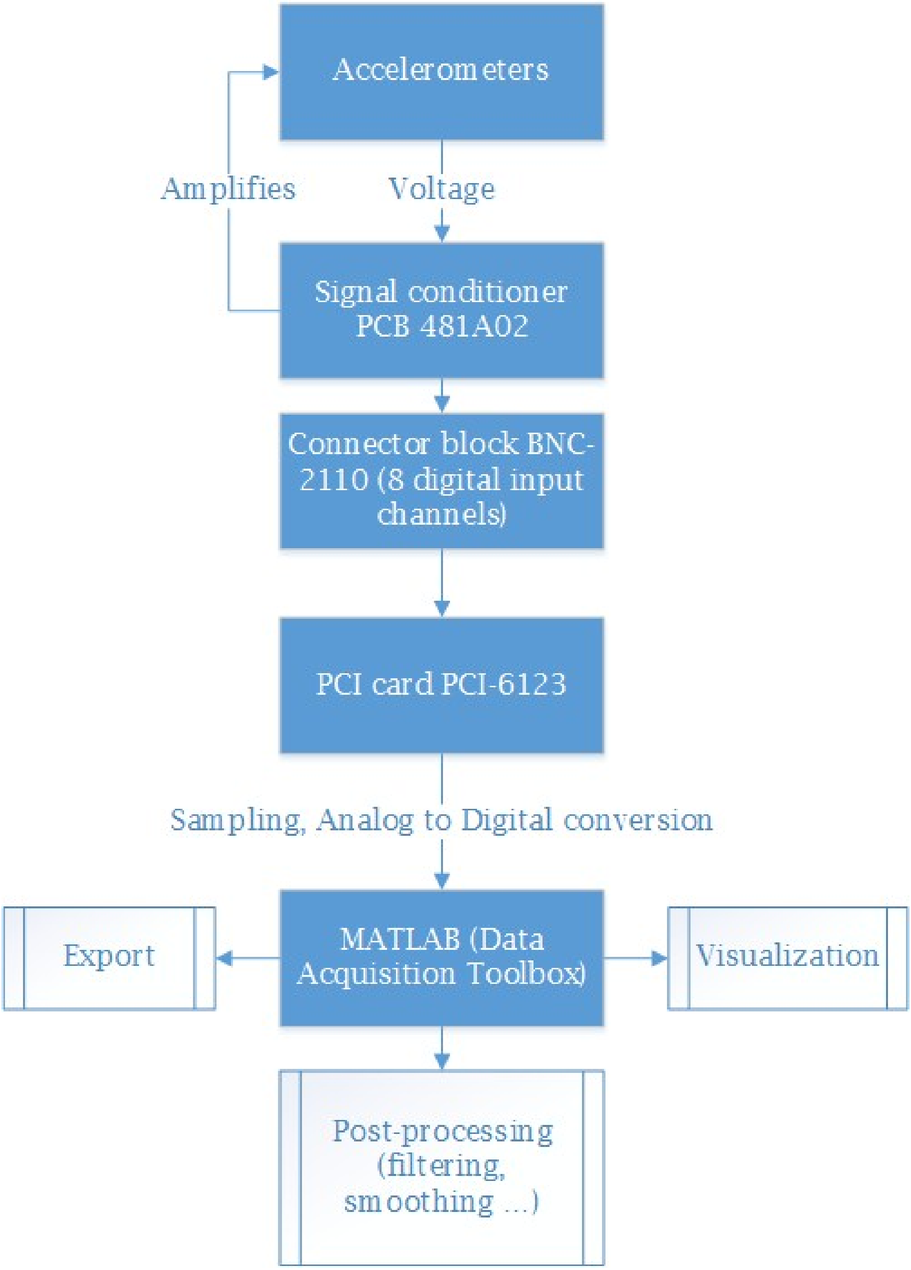

Figure 2.6: Block diagram of the organization of the data acquisition devices.

between $1/(\Delta t)$ and $f_s/2$. In 2D experiments, we can access the acceleration at four locations simultaneously (each channel corresponding to the x or y acceleration component of a sensor particle). Accessing wave propagation data at more than four locations at a time (see chapter 4 for example) requires to perform several runs with the same time reference. This is achieved by keeping one sensor location fixed and moving the other three. Lastly, the maximum voltage range [-10 V +10 V] of the DAQ board was selected in every experiment. This allows us to measure acceleration signals with an amplitude as high as $\frac{10}{0.51e-3} \approx 20000$ m/s^2 (twice as much as the measurement range of the accelerometer) with a high resolution ($\approx$ 0.3 mV or 0.6 m/s^2).

2.2 Numerical Setups

Several numerical setups and tools were used and developed in order to predict and/or confirm our experimental observations and perform topology and material optimizations. In this section, we describe the modeling of our 2D granular crystals as well as the numerical methods selected for the simulations. The optimization techniques are presented in detail in the chapters of interest (chapters 5 and 6).

2.2.1 Numerical Modeling and Integration Schemes

We model our 2D granular crystal as coplanar point masses lying in the x-y plane connected by nonlinear springs (see Fig. 2.7).

Each point mass possesses the material properties of the bead it represents (radius, mass or density, stiffness and Poisson's ratio). The boundaries are modeled by spherical particles of infinite radius and their displacements are prescribed and set to zero. The compressive force applied by a particle interacting with its neighbors is given by the Hertz law [23, 24] presented in Eq. 1.1.

We restrict our study to conservative systems only and neglect any dissipation phenomena (dry friction, viscoelasticity, plasticity). A justification for this assumption is provided in section 2.2.3. The rotation of the particles is also not taken into account

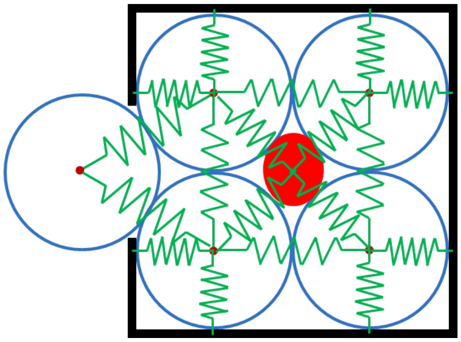

Figure 2.7: Schematic diagram of the numerical setup for a simplified 2 by 2 square packing. A spherical interstitial intruder is placed in the middle of the packing and the system is impacted from the left by a striker particle. Each (green) nonlinear spring represents a 2-node element connecting the point masses (red dots).

and no external forces are applied on the system. Finally, the loading condition is set by giving the striker particle some initial velocity v_0.

2.2.2 Integration Schemes

The early simulations were run using an explicit fourth order Runge-Kutta integration scheme to solve the nonlinear equations of motion:

$$\ddot{u}_i = -\sum_{\langle j \rangle} A_{i,j}[(u_i - u_j).\vec{e_{ij}}]_+^{\frac{3}{2}} \vec{e_{ij}}, \tag{2.1}$$

where u_i is the vectorial displacement of the i^{th} particle from its equilibrium uncompressed position and $\vec{e_{ij}}$ is the unit vector connecting the centers of beads i and j, oriented from i to j; the symbols $\langle j \rangle$ denote that j needs to be a nearest neighbor to i. $[X]_+$ denotes the positive part of X as no interaction exists between particles when they lose contact. Runge-Kutta schemes are widely used for their high order accuracy and stability (at the expense of integration speed). We chose a time step of 5×10^{-8} s, which ensures conservation of the total energy with an accuracy better than 3×10^{-7}%.

A second numerical setup was later developed in which a finite element approach was taken. The crystal is composed of two-node elements that connect the centers of every pair of adjacent particles and we write the governing equation of motion under the following semi-discrete matrix form:

$$R(u, \ddot{u}) = M\ddot{u} + S(u) - F_{ext} = 0, \tag{2.2}$$

where R is the residual vector, M is the positive definite symmetric mass matrix, u and $\ddot{u}$ are the displacement and acceleration nodal vectors, F_{ext} is the external nodal force vector and $S(u)$ represents the internal nodal force vector. To obtain the fully discrete form, we use a discrete implicit Newmark time integration scheme [107, 108]:

$$\begin{cases} K_2^{(n)}\Delta a & = -R\left(a^{(n)}, u^{(n)}\right) = -Ma^{(n)} - S\left(u^{(n)}\right) + F_{ext}^{(n)} \\ a^{(n+1)} & = a^{(n)} + \Delta a \\ u^{(n+1)} & = u^{(n)} + \Delta t v^{(n)} + \frac{1}{2}\Delta t^2\left((1-2\beta)a^{(n)} + 2\beta a^{(n+1)}\right) \\ v^{(n+1)} & = v^{(n)} + \Delta t(1-\gamma)a^{(n)} + \Delta t\gamma a^{(n+1)} \end{cases} \tag{2.3}$$

where $K_2^{(n)} = \frac{\partial R}{\partial a^{(n)}} = \left(M + \beta\Delta t^2 \frac{dS\left(u^{(n)}\right)}{du^{(n)}}\right)$ is the stiffness tangent at time step n, $u^{(n)}$, $v^{(n)}$ and $a^{(n)}$ are the approximations of the displacement, velocity and acceleration at time step n and the parameters β and γ are the usual Newmark parameters.

This Newmark scheme ($\beta = 1/4$ and $\gamma = 1/2$) was implemented in a Newton-Raphson iterative loop to solve for the root of the residual at every time step as the residual R depends nonlinearly on the acceleration:

$$\begin{cases} K_2^{(n)}\Delta a = R \\ a^{(n)} = a^{(n-1)} + \Delta a. \end{cases} \tag{2.4}$$

The external forces, included in Eq. 2.2 for generality, are equal to zero in this study as the only external force, gravity, does not play a role. A time step of 1×10^{-6} s is enough to ensure conservation of the total energy with a similar accuracy as the Runge-Kutta solver.

2.2.3 Effect of Dissipation

The acceleration values measured experimentally are compared to the values obtained from numerical simulations. However, when comparing numerical results with experiments, several factors can account for discrepancies. The most important one is the presence of dissipation in real systems. Dissipation itself can be attributed to a large number of factors including (naming the most important mechanisms only):

- friction (between the granular crystal and the boundaries as well as between each pair of interacting particles),
- viscolelasticity and plasticity of the particles,
- transfer of energy to internal or rotational modes of the particles.

Thermal fluctuations for example are completely negligible in granular media if compared to the potential energy of each grain [4].

A first approach considers inelastic collisions via a restitution coefficient. Early studies considered only a constant restitution coefficient [109, 110] and were later improved in more realistic models taking into account the velocity dependence of the restitution coefficient in viscoelastic processes [111, 112], plastic processes, or both [113]. Lindenberg and collaborators produced several studies investigating the effect of kinetic friction on the collision of two granules [114] and the pulse dynamics of an entire chain [66]. Using analytical models and simulations, they showed that friction increases the backscattering of the particles and is responsible for an overall decay of the pulse energy which causes it to slow down while retaining its shape and width.

Dissipation is typically modeled by the addition of a linear or nonlinear viscous damping term proportional to the relative velocity of neighboring particles [76, 115] or simply proportional to the velocity of the particle [66, 116]. The inclusion of friction is necessary in order to investigate the effect of rotation of spherical particles with normal contacts. Mindlin theory for frictional balls [96, 117], which extends Hertz contact theory by taking tangential frictional forces into account, was used by several groups for the study of 2D granular materials [97, 118].

In this thesis, experimental conditions were selected so as to minimize the effects of dissipation: we chose polymer materials for the walls and supporting planes in the different experimental setups in order to minimize friction, impact velocities were low enough to ensure that the particles did not undergo plastic deformation [3, 24] and most of the studies were conducted using metals for which viscoelasticity is limited. Although observable in the experimental data, dissipation effects are reasonably low for the selected materials and dimensions of the crystals presented in this thesis (≤ 20 particles) and the modeling of dissipation is not included in the scope of this thesis.

Chapter 3

Wave Propagation in Square Granular Crystals with Spherical Interstitial Intruders

We investigate the propagation and scattering of highly nonlinear waves in granular systems composed of spheres in contact and arranged in a square packing, and study how the presence of small and light spherical interstitial defects, also referred to as intruders, affects the wave propagation. The effects of a single defect are investigated experimentally and compared to numerical simulations, showing very good quantitative agreement. Transmitted and scattered waves are formed, whose characteristics depend on the material properties of the defect in relation to the properties of the particles in the lattice. Experiments and numerical simulations reveal that stiffer defects are more efficient at redistributing energy outside the impacted chain and soft defects induce a localization of the energy at the defect. Finally, the effects of the presence of two defects, placed diagonally or aligned in the square packing, are also investigated, as well as how their interaction depends on their relative positions.

3.1 Introduction

Several past studies focused on analyzing the interaction of a solitary wave with defects in a 1D system [15, 17, 53], as well as the interaction of a solitary wave with different interfaces [8, 11, 12, 63, 64, 87, 119, 120]. Interesting phenomena have been shown to occur when impurities are present in an otherwise homogeneous highly nonlinear chain of spheres, and mass defects in particular have drawn significant attention [15, 17, 53]. M. Manciu, S. Sen and A.J. Hurd [53] studied the backscattering of a soliton-like wave as it encounters a lighter or heavier defect and suggested that the propagation of acoustic pulses could be used to detect impurities burried in granular media. The elementary interaction of light or heavy intruders with shock waves has been investigated numerically [17]. Hascoët et al. showed that a light defect acts as a secondary source of solitary waves, whereas a heavier defect is simply translated, creating a train of solitary waves forward and a stable reflected wave. When reached by a shock wave, a light defect will start oscillating between its two neighbors. Those oscillations are damped as the defect becomes a secondary source of solitary waves, and one can observe trains of solitary waves of decreasing amplitudes in both directions as the defect collides with its nearest neighbors. A heavy impurity will behave very differently: instead of exciting the defect, the shock will simply shift it in its moving direction and the chain will be halved in two parts. A stable reflected wave will propagate to the left of the defect, while the forward propagating solitary wave will be decomposed in a train of pulses. Recently, it was experimentally shown that the presence of a lighter mass defect can induce mechanical energy localization [15] associated with a local linearization of the system around the defect. When interacting with the solitary wave, the impurity starts oscillating with a frequency which increases nonlinearly with the amplitude of the propagating pulse and decreases with the size of the impurity. The inclusion of multiple defects has also shown interesting dynamic effects [11, 12, 62, 63] and symmetry breaking phenomena [18]. 1D "tapered" chains have been studied in detail and have been proposed for the design of granular protecting devices based on the redistribution of the initial energy input [10, 56–58, 60, 61].

Nesterenko numerically studied the effects of disorder in 1D systems consisting of spheres of same material whose diameters were randomly assigned, and showed how disorder is responsible for the attenuation and decomposition of shock waves and solitary waves [3, 7]. In a more recent study by Ponson et al. [16], the propagation and scattering of highly nonlinear waves in disordered 1D composite granular media was investigated. They studied a dimer chain composed of alternating stainless steel and aluminum spheres in which defects were introduced by switching the positions of neighboring particles, locally disrupting the symmetry of the crystal. It was shown that two regimes exist depending on the level of disorder. In low-disordered chains, they observed numerically and experimentally the propagation of a solitary pulse with exponentially decaying amplitude. As the disorder increases, the dispersion capacity of the system saturates and the wave becomes fully delocalized. Genetic algorithm methods were used to optimize the distribution of defects in a 1D granular chain of particles in order to reduce the maximum amplitude of the transmitted signal [9].

The natural extension to the study of 1D crystals is to explore the dynamic response of simple 2D square packings (pseudo 1D systems) [102]. Leonard and Daraio showed that, depending on the type of excitation imparted on the system (location, number of particles impacted, temporal duration of the impact), solitary waves can form in one or several different chains within the square array. The presence of interstitial particles uniformly distributed in the packing (i.e., effectively forming a centered squared granular lattice) has been shown to force the system to distribute stress in 2D fronts, whose properties can be tailored by the selection of the particles' material properties [103, 122].

It is important to note that the presence of defects in 1D chains is limited to the presence of particles of different sizes, materials, or shapes placed in the chain in contact with neighboring particles [15, 17, 53]. In 2D, this definition needs to be extended as it is also possible to add particles on off-grid positions. In addition, 2D systems allow for the presence of vacancies (i.e., lattice points with no particles) without completely disrupting the wave propagation. In this chapter, we describe the interaction of highly nonlinear solitary waves with a single interstitial defect particle, using experiments and numerical simulations to study the effects of force and energy redirection, reflection and trapping, as a function of the defect's material properties. We also describe the interaction between two defects as a function of their relative position in the lattice.

Our presentation is structured as follows. In section 3.2, we present the experimental and numerical setup at hand. In section 3.3, we examine the case of a single defect (also of different stiffness and density characteristics). It is seen that the stiffer the defect, the more it favors the redistribution of the energy in the system. A rigid body collision model is also used based on the energy and momentum conservation to establish a reasonable approximate estimate of the resulting distribution of the relevant energy fractions. Finally, the case of two interstitial defects is considered in section 3.4, both in the special setting where they are in contact with the same particle, enhancing the number of directions that receive an observable fraction of the pre-collision energy, and in that where they are more separated. In the latter case, the intruders can be thought of as acting independently. Finally, in section 3.5, we present some conclusions and possibilities for further study.

3.2 Experimental and Numerical Setups

Our 2D experimental setup is composed of a flat polycarbonate base and four movable delrin walls to support the particles as shown in Fig. 2.2, and is described in detail in section 2.1.1.1. We assemble a 20 by 20 square packing using $2R = 19.05$ mm diameter stainless steel spheres (nonmagnetic, 316 type). The defect particles consist of custom-made spheres that fit exactly in the interstitial sites. We studied the effects of several different materials for the defect particles: tungsten carbide (TC), 316 stainless steel, brass alloy 260 and polytetrafluoroethylene (PTFE). The material properties of the defect particles studied are summarized in Table 2.1. The system is impacted on one side by a single striker particle identical to the particles forming the square packing and its velocity is measured with the use of an optical velocimeter. The different particle arrangements considered in this study are reported in Fig. 3.1.

Custom-made sensor particles were built to access the acceleration at local positions in the setup and are described in section 2.1.2. The data was collected using the equipment and procedure described in section 2.1.3.

We numerically model the square packing of 400 spherical beads plus one or two

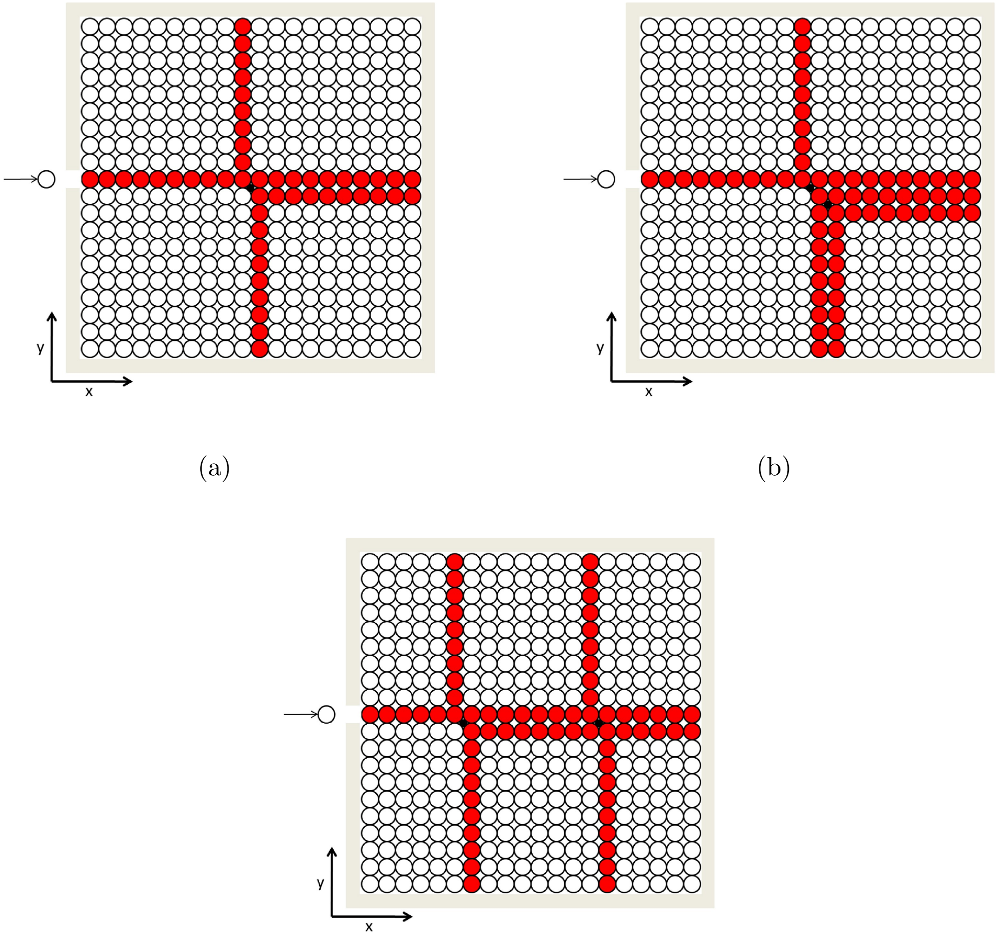

(a)

(b)

(c)

Figure 3.1: Schematic diagrams of the different system configurations studied. 3.1(a) Single defect case: a spherical intruder (black particle) is included in the center of a 20 by 20 square packing composed of stainless steel spheres confined by four delrin walls. The system is impacted by a steel particle identical to the other particles in the lattice, exciting a single row of spheres from the left side. 3.1(b) Configuration including two defects placed diagonally, adjacent to the same particle. 3.1(c) Configuration including two defects placed along the same row of particles. In all panels, the red (grey) color identifies the particles involved in the wave propagation (reflections not taken into account).

interstitial spherical defects and a striker bead with (conservative) Hertzian interactions between particles (see Eq. 2.1). Numerical simulations are run using a fourth order Runge-Kutta integration scheme to solve the equations of motion of all the particles (see section 2.2) and we directly compare the numerical accelerations to the experimental ones.

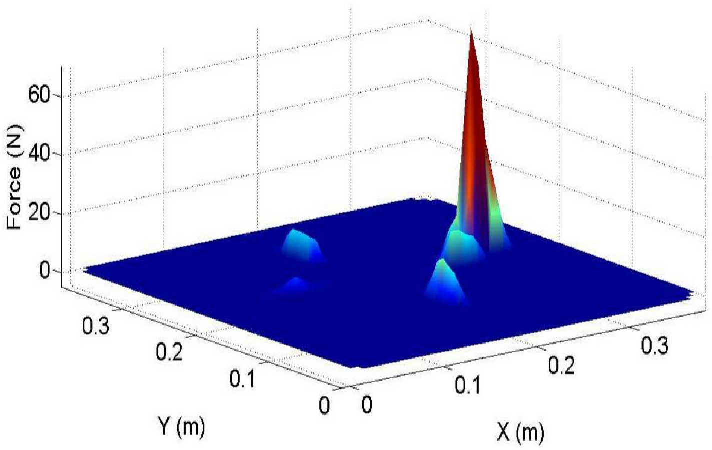

Figure 3.2: Force versus position map obtained from the simulation of the dynamics of a system composed by a steel intruder in a steel square packing at $t = 0.6$ ms. The origin of time is the impact of the system at coordinates ($X = 0.0$ m, $Y = 0.2$ m) by a steel striker particle with initial velocity 0.2 m/s. After interaction of the incoming solitary wave with the defect, the transmitted, reflected and scattered solitary waves are evident.

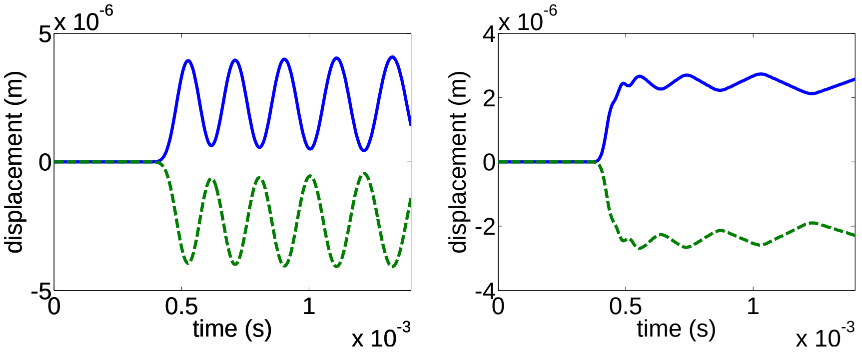

(a)

(b)

Figure 3.3: Numerical results showing the displacement of the defect particle as a function of time when it is made of 3.3(a) PTFE and 3.3(b) stainless steel. In both cases, the solid blue curve represents the displacement of the defect particle in the x direction and the dashed green curve represents the the displacement of the same particle in the y direction.

3.3 Single Defect

The first system studied is presented in Fig. 3.1(a). A spherical defect is placed in the center of a uniform steel square packing, and a horizontal chain in contact with the defect is impacted by a steel sphere. Without the presence of the intruder, the system would behave as an effectively 1D system, i.e., one in which the excitation only propagates along its initial direction. However, the presence of the defect adjacent to the impacted chains modifies the dynamic response of the system: after the incoming solitary wave interacts with the defect, we observe one reflected, one transmitted and three scattered waves (see Fig. 3.2), whose properties depend on the material properties of the defect. A single solitary wave is always transmitted down the impacted chain after the defect. This is due to the fact that the first bead after the intruder in the impacted chain loses contact with both its left neighbor and the intruder. We numerically evaluate the scattered energy by calculating the difference between the input energy and the energy carried by the transmitted solitary wave. We refer to the chains in which waves are propagating as “impacted”, “adjacent”, “top” and “bottom” chains, colored in red on Fig. 3.1(a). After the incoming wave

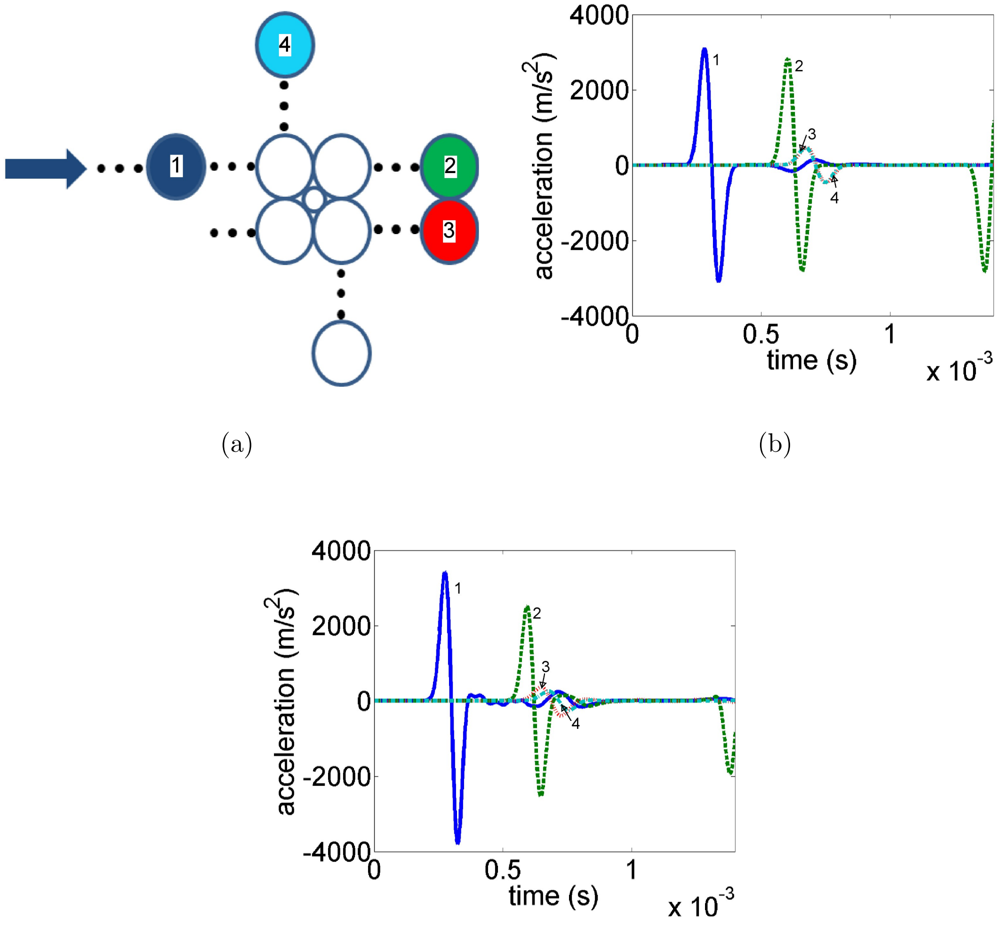

(a)

(b)

(c)

Figure 3.4: Single stainless steel defect configuration, impacted by a stainless steel sphere of diameter 19.05 mm, with initial velocity 0.19 m/s. 3.4(a) Simplified schematic diagram representing the particles located around a single spherical intruder. The colors and labels of the particles correspond to the colors and labels of the acceleration curves in panels 3.4(b) and 3.4(c). The arrow on the left represents the impact direction. 3.4(b) Numerical results showing the particles' acceleration as a function of time for the incoming and reflected wave (solid dark blue curve labeled "1", four particles away from the defect), the transmitted wave (dashed green curve labeled "2", five particles away from the defect) and the scattered waves (dotted red and turquoise labeled "3" and "4", five particles away from the defect). 3.4(c) Experimental results corresponding to 3.4(b).

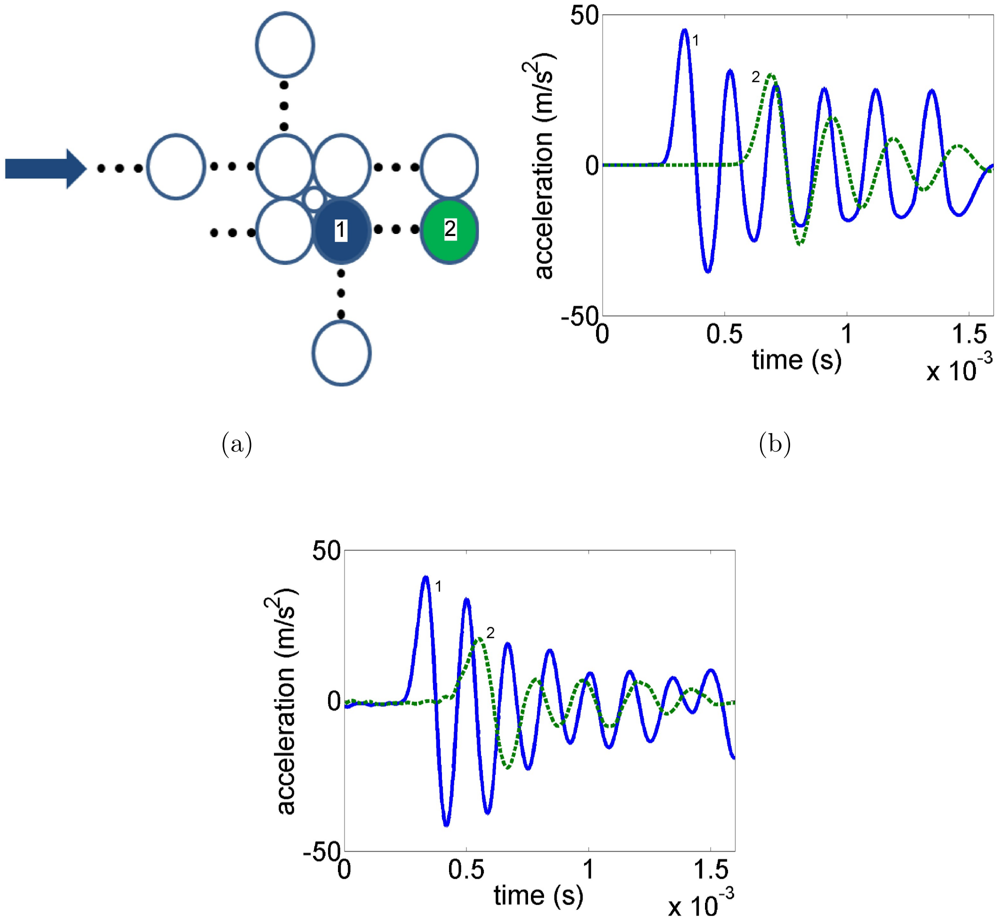

(a)

(b)

(c)

Figure 3.5: Single PTFE defect configuration, impacted by a stainless steel sphere of diameter 19.05 mm, with initial velocity 0.23 m/s. 3.5(a) Simplified schematic diagram representing the particles located around a single spherical intruder. The colors and labels of the particles correspond to the colors and labels of the acceleration curves in panels 3.5(b) and 3.5(c). The arrow on the left represents the impact direction. 3.5(b) Numerical results showing the particles' acceleration as a function of time for a particle immediately adjacent to the defect (solid blue curve labeled "1") and five particles away (dashed green curve labeled "2"). 3.5(c) Experimental results corresponding to 3.5(b).

reaches the defect particle, the defect's motion is observed to be identical in the x and y directions. This is shown in Fig. 3.3 where on can see that the two components of the displacements of the defect particle are equal and opposite. This is due to the fact that the center of mass of the intruder is placed along the line connecting the centers of mass of its top-left and bottom-right neighbors (at a 45° angle with the x-axis). We consequently observe, both experimentally and numerically, identical signals propagating down the "adjacent" and "bottom" chains. When the transmitted waves are reflected back from the boundaries they excite the intruder again, and cause its motion to become disordered. In this study, we limit our analysis to the interaction of the defect with the incoming wave, neglecting the effects of reflections.

First, we numerically investigated the effect of variations of the defect's mass and stiffness on the energy redirection through the crystal, for different impact velocities. We showed that the defect's mass has very little effect on the maximum amplitude of the signal transmitted beyond the defect particle in the direction of impact, relative to the input energy. However, the defect's stiffness can play a nontrivial role in the interactions: the stiffer the defect, the more energy is redirected from the impacted chain to other parts of the system.

3.3.1 Single Steel Defect

The results obtained for a lattice composed of stainless steel particles and a single stainless steel defect are shown in Fig. 3.4. It is evident that the system supports the formation and propagation of a single solitary wave, and that the solitary wave's interaction with the defect results in a small amount of energy redirected from the impacted chain to two solitary waves propagating sideways and, partially, to a single solitary wave reflected backward. We find excellent agreement between numerical and experimental results (compare Fig. 3.4(b) with Fig. 3.4(c)). However, the presence of dissipative losses in experiments is evident from the decreasing wave amplitude of the traveling waves. For this configuration, numerical calculations show that 14.32% of the input energy is transmitted to other parts of the system and does not travel along

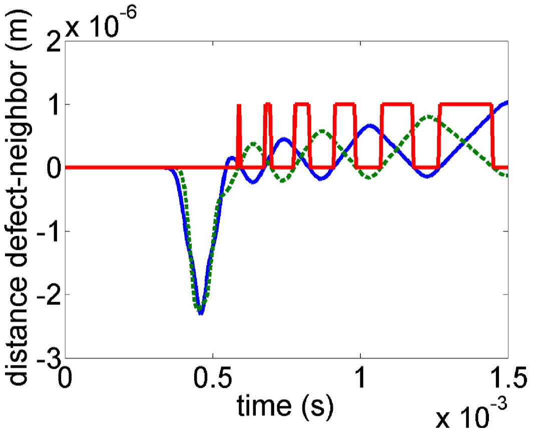

(a)

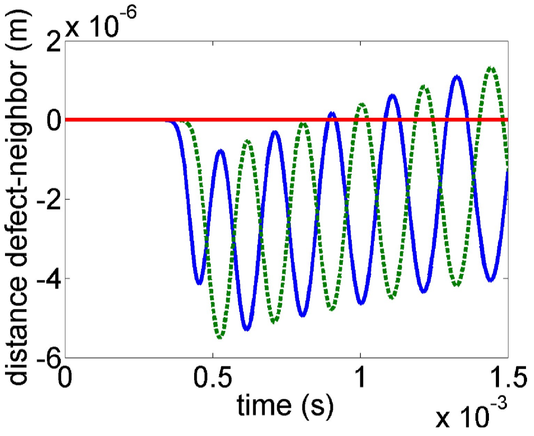

(b)

Figure 3.6: Numerical results showing the horizontal displacement of the defect particle for the 3.6(a) stiff (steel) and 3.6(b) soft (PTFE) defect configurations, relative to its two active neighbors (top left and bottom right particles adjacent to the defect particles). The solid blue curve represents the relative displacement in the x direction of the defect particle with respect to its top-left neighbor and the dashed green line with respect to its bottom-right neighbor. Note that we do not show the relative displacement in the y direction since it is equal to the relative displacement in the x direction. The two particles are compressed against each other when the curves are negative and they are not in contact when positive. The red step-curve is non zero when a complete loss of contact occurs between the defect and its two active neighbors.

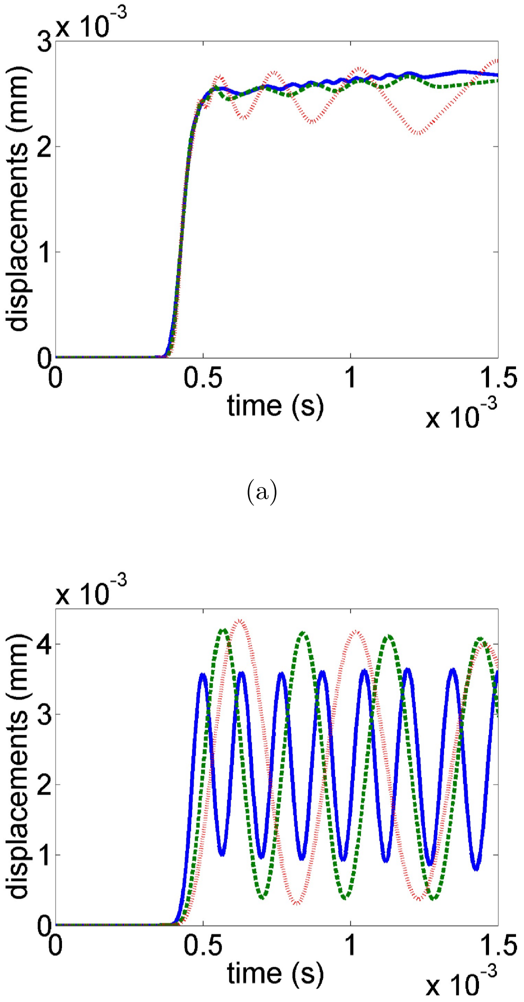

(a)

(b)

Figure 3.7: Numerical results showing the effect of density variation on the defect particle's displacement in the horizontal direction (along the striker direction). Note that we do not show the displacement in the y direction since it is equal to the displacement in the x direction. The numerical results are obtained from idealized particles in which the elastic modulus (E) is kept constant, and the density is varied arbitrarily. 3.7(a) stiff (E = 193 GPa) and 3.7(b) soft (E = 1.26 GPa) case. The density values considered in both panels are: $d = 1000$ Kg/m^3 (solid blue), $d = 4000$ Kg/m^3 (dashed green) and $d = 8000$ Kg/m^3 (dotted red) curves.

the impacted chain after the intruder (4.15% is deflected up, 4.30% down, 4.30% in the adjacent chain and 1.57% reflected).

3.3.2 Single PTFE Defect

The results obtained for the lattice composed of stainless steel particles and a single PTFE defect are shown in Fig. 3.5. In this case, the interaction of the incoming solitary wave traveling in the impacted chain with the soft intruder leads to the formation of trains of solitary waves of decreasing amplitudes in the "top", "bottom" and "adjacent" chains, and we also observe a train of solitary waves of small amplitude reflected backward. When reached by the incoming solitary wave, the PTFE intruder is strongly compressed between its top-left and bottom-right neighbors, and starts oscillating between them. As it oscillates, the PTFE intruder slowly pushes its neighboring particles away from it, bouncing back and forth. The energy of the intruder progressively decreases as multiple solitary waves are formed in all four directions, resulting in the trains of waves observed numerically and experimentally. For this configuration, numerical calculations show that only 1.23% of the input energy is transmitted to other parts of the system and does not travel along the impacted chain after the intruder. For comparison, a stiffer tungsten carbide intruder deflects 17.7% of the total input energy, while a softer brass intruder deflects 11.33% of the input energy.

3.3.3 Relative Displacements

The relative displacements of the defect particle with its neighbors are shown in detail in Fig. 3.6 for the particle configurations analyzed in Fig. 3.4 and Fig. 3.5. For the packing including a single steel defect (Fig. 3.6(a)), it is evident that the top-left neighbor compresses the defect particle, which in turn compresses its bottom-right neighbor, and all three particles are translated (at time = 0.4-0.6 ms). After this translation the intruder loses contact, first with its first neighbor, and quickly thereafter also with its second, and then bounces back and forth between the two. The two neighbors slowly become more and more distant from each other and the defect also carries less velocity having imparted progressively more of it through subsequent collisions. This leads eventually to “individual” interactions of the defect with one neighbor at a time, mediated by longer travel times during which the defect is in contact with neither of its neighbors. The relative displacement between the defect and its neighboring particles is always small (0.2 microns) and these interactions give rise to small secondary waves propagating laterally and in the row of particles adjacent to the impacted one. This picture (of a sequence of collisions with top left and bottom right neighbors) will also form the basis for our rigid body collision model theoretical analysis of the relevant phenomenology presented below. For a soft PTFE intruder (Fig. 3.6(b)), we observe that the first interaction with the first neighbor causes the intruder to be strongly compressed between the two bigger and stiffer steel spheres. The intruder oscillates between the two particles with a frequency of oscillation being a nonlinearly increasing function of the amplitude of the incoming wave. The two stiff neighbors are slowly pushed away by the intruder, and a train of solitary waves is transmitted after the defect in the row of particles adjacent to the impacted one.

3.3.4 Effect of Density

Numerical simulations were run to investigate the role of density independently of the role of stiffness of the defect particles. We created idealized particles, in which we varied the particle density while maintaining a constant stiffness value. For these cases, we plot the displacement of the intruder particle to show the variations in the dynamics of the systems. Because of the symmetry of the system, the x- and y-displacements of the intruder have equal norms. In Fig. 3.7 we present the x-displacement (i.e., horizontal displacement) of the defect particle for both a stiff ($E = 193$ GPa, Fig. 3.7(a)) and a soft ($E = 1.26$ GPa, Fig. 3.7(b)) material, varying the density in each case. We note that as the incoming solitary wave reaches a stiff defect from its top left neighbor, the defect is forced to translate laterally. This translation is followed by small oscillations of the defect between its top left and bottom right neighbors, during which the defect alternately loses contact between them. In this scenario, the incoming solitary wave is decomposed into transmitted, reflected and scattered solitary waves, and the secondary oscillations result in small amplitude trailing waves. When the incoming solitary wave reaches the softer defect, we observe a transition to a different dynamic regime in which the defect particle starts oscillating immediately, without a lateral translation (see Fig. 3.7(b)). In this case, the defect is compressed between its two active neighbors (top left and bottom right) and the large amplitude of oscillations is due to the larger deformations of the soft intruder between the steel particles. Energy is localized similarly to what was observed in 1D systems [15], and the defect particle excites secondary solitary waves. The formation of transmitted trains of solitary waves, observed both numerically and experimentally, are shown in Fig. 3.5.

3.3.5 Rigid Body Collision Model

For the case of stiff defects where we observe transmitted, scattered and reflected solitary waves (as opposed to trains of solitary waves for soft defects), a natural model has been developed to estimate the percentages of the input energy traveling in the top, bottom, impacted and adjacent chains after interaction of the intruder with the incoming solitary wave. We assume the spherical particles (see numbering in Fig. 3.8) to be rigid bodies undergoing elastic collisions. This approach is a simplification of the interaction of a multi-particle wave with the interstitial defect. A similar approach was taken in the independent collision model of [57]. This approach is exact for perfectly rigid spheres and a good approximation when the collision durations are short in comparison to the time between two collisions, and was later used in [10, 58] for the description of tapered chains. The analytical results obtained with this approximation were found to be in very good agreement with the full field numerical model (which considered energy and momentum exchanged between all the particles in the system).

We first consider the interactions between particles 1, 2 and 3, and denote by m and m_d the masses of the particles in the packing and the defect respectively. The

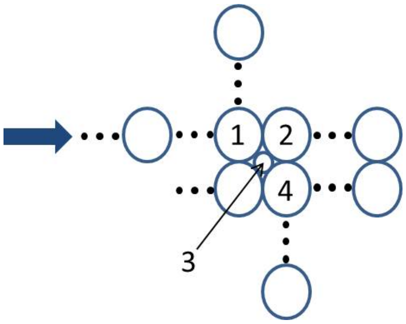

Figure 3.8: Numbering of the particles involved in the calculation of the rigid particle model.

superscripts i, t, r and u represent the incoming, transmitted, reflected, and scattered in the up direction velocities respectively. Using the conservation of momentum and kinetic energy, we obtain the following system of equations:

$$\begin{aligned} mv^{(1i)} &= -mv^{(1r)} + mv^{(2t)} + \frac{\sqrt{2}}{2} m_d v^{(3t)} \\ mv^{(1u)} &= \frac{\sqrt{2}}{2} m_d v^{(3t)} \\ \frac{1}{2} m {v^{(1i)}}^2 &= \frac{1}{2} m {v^{(1r)}}^2 + \frac{1}{2} m {v^{(1u)}}^2 + \frac{1}{2} m {v^{(2t)}}^2 + \frac{1}{2} m_d {v^{(3t)}}^2 . \end{aligned} \tag{3.1}$$

We numerically observe that the amplitude of the reflected wave is small with respect to the other scattered and transmitted waves (see Fig. 3.4). This is due to the fact that m_d is small with respect to m and we consequently neglect $v^{(1r)}$ in our analysis. Eq. 2 then yields:

$$\begin{aligned} v^{(1u)} &= \frac{m_d}{m + m_d} v^{(1i)} \\ v^{(2t)} &= \frac{m}{m + m_d} v^{(1i)} \\ v^{(3t)} &= \sqrt{2} \frac{m}{m_d + m} v^{(1i)} . \end{aligned} \tag{3.2}$$

Assuming that all the energy of $v^{(2t)}$ forms the transmitted part in the direction of the initial excitation, we obtain the transmitted energy fraction for the homogeneous

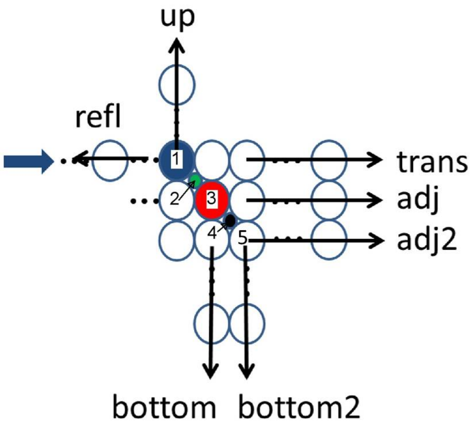

(a)

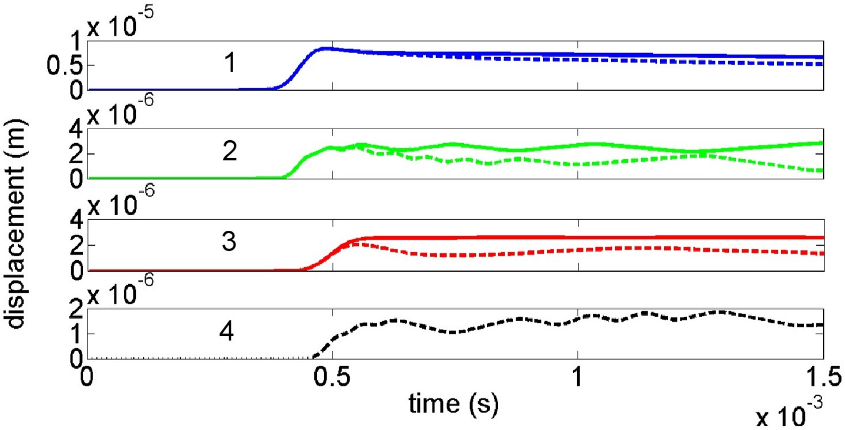

(b)

Figure 3.9: Numerical results showing the horizontal displacement of the particles involved in the impulse redirection when two stainless steel intruders are located in a square packing of stainless steel spheres impacted from the left by a steel particle. 3.9(a) Schematic diagram of the particles' configuration. The arrows indicate the labeling of the different chains of interest (where a signal is propagating). 3.9(b) Displacements of the four numbered (and colored) particles in 3.9(a). On each plot, the solid line corresponds to the results obtained when only a single defect is present in the packing, and the dotted lines correspond to the results obtained when two defects are present in the packing. The colors and labels of the particles correspond to the colors and labels of the displacement curves in panel 3.9(b).

case as:

$$\frac{E_t}{E_i} = \frac{\frac{1}{2}mv^{(2t)^2}}{\frac{1}{2}mv^{(1i)^2}} = \left(\frac{1}{1+(\sqrt{2}-1)^3}\right)^2 = 87.17\%. \tag{3.3}$$

This is in good agreement with the numerical results for the same case (85.68%). The contribution to the energy deflected up is $\frac{\frac{1}{2}mv^{(1u)^2}}{\frac{1}{2}mv^{(1i)^2}} = \left(\frac{(\sqrt{2}-1)^3}{1+(\sqrt{2}-1)^3}\right)^2 = 0.44\%$.

We consider thereafter the interactions of the defect (which has velocity $v^{(3t)}$) with particles 1 and 4. We remind the reader that the motion of the intruder being along the diagonal, it is unnecessary to consider the interactions with particle 2 and also with the intruder's bottom-left neighbor. We model the transmission of the energy from the intruder to its two active neighbors by an infinite series of instantaneous elastic collisions. Denoting by $v^{(3tr)}$ and $v^{(4t)}$ the velocity of the intruder and the velocity transmitted to particle 4 after their first collision, conservation of momemtum and kinetic energy yields:

$$\begin{aligned} v^{(4t)} &= \frac{2m_d}{m_d+m}v^{(3t)} \\ v^{(3tr)} &= \frac{m_d-m}{m_d+m}v^{(3t)}. \end{aligned} \tag{3.4}$$

After this first interaction of the intruder with particle 4, another collision happens between the intruder and particle 1, and so on. Notice that this is exactly in line with the observations of Fig. 3.6(a). Summing the contributions of all the collisions, one can calculate the energy fractions transmitted to particle 1 and 4:

$$\begin{aligned} \frac{E_4}{E_i} &= \frac{8(mm_d)^2}{(m_d+m)^4}\sum_{k=0}^{\infty}\left(\frac{m_d-m}{m_d+m}\right)^{4k} \\ \frac{E_1}{E_i} &= \frac{8(mm_d)^2}{(m_d+m)^4}\sum_{k=0}^{\infty}\left(\frac{m_d-m}{m_d+m}\right)^{4k+2}. \end{aligned} \tag{3.5}$$

We finally assume that the energy transmitted to particle 4 will be split equally between the adjacent and the bottom chains. Similarly, the energy transmitted to particle 1 by the intruder is assumed to be split equally between the top chain and the impacted one (before the intruder). Hence, adding the contributions of the first

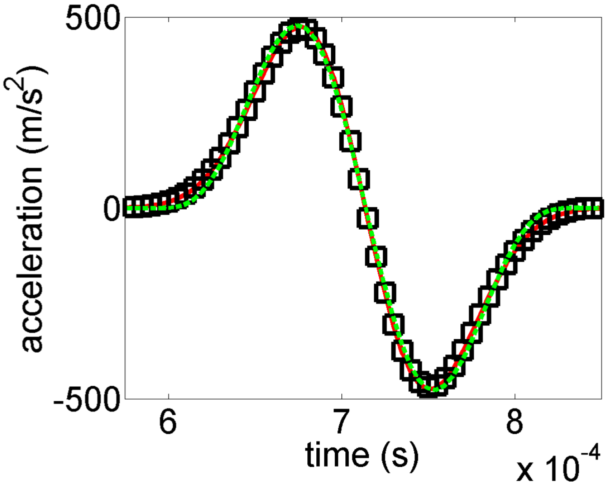

Figure 3.10: Comparison of the shape of the acceleration signals propagating in the "adjacent" chain after the defect particle with the analytical solution obtained by Nesterenko for 1D homogeneous systems. The solid red curve (resp. black square makers) represents the signal observed five (resp. nine) particles after the intruder. The green dashed curve shows Nesterenko's analytical solution.

	up	refl	adj	bottom	trans
Rigid particle model	3.10	2.66	3.54	3.54	87.17
Numerical	4.15	1.57	4.30	4.30	85.68

Table 3.1: Comparison of the percentages of the input energy redirected in the system in the rows and columns of spheres adjacent to the defects for the rigid particle model and numerical calculations. We define energy "up" as the energy redirected upward in the column of particles above the first defect, "reflected" as the energy reflected back in the impacted chain, "adjacent" as the energy redirected in the right direction in the row adjacent to the impacted chain, "bottom" as the energy redirected downward in the column of particles below the first defect, and "transmitted" as the energy transferred in the impacted chain after the defect.

part of the calculation, we can find the transmitted, scattered and reflected energy fractions, in fairly good agreement with the numerical simulations. The results from this calculation as well as the numerical ones are summarized for the case of a stainless steel intruder in Table 3.1.

Understanding how a single spherical intruder interacts with a solitary wave is the first step towards the understanding of more complex dynamics that appear when several defects are present. In the next section, we investigate the interaction of two spherical intruders when placed in a square packing, for two different configurations.

3.4 Two Defects

We study the effects of the presence of two defects in the lattice as a function of their relative position. As seen in the first part of this manuscript, when a single solitary wave interacts with a single defect, the energy is redistributed only along the few chains adjacent to the defect. If two defects are located sufficiently far apart from each other in the granular crystal, we expect their individual behavior to be independent of each other, and similar to that of a single defect, without any dynamic interactions between them. However, when the two defects are sufficiently close to each other, the dynamic behavior of the granular crystal is expected to be dependent on the interaction between the two defects.

3.4.1 Two Defects in Contact with the Same Particle

In this section, we study the effect of two defects placed diagonally to each other, but adjacent to the same particle in the crystal (Fig. 3.1(b)). Similarly to the case where one defect only is present, the positions of the intruders with respect to their direct neighbors will cause them to move along the diagonal connecting the centers of mass of particles 1 and 3 (see Fig. 3.9(a)). The x-displacement and y-displacement of the first intruder are hence equal, as are the x-displacement and y-displacement of the second intruder. It is important to remember that this symmetric behavior is preserved only before the waves reflected from the boundary of the system reach the intruders, after which their motions become disordered. Similarly to the analysis performed for the single defect case, we numerically calculate the total energy redirected from the impacted chain by subtracting the energy carried by the solitary wave in the impacted chain after the defects from the input energy. We restrict our analysis to the case of stiff intruders. We show that the dynamic behavior of the first defect is very similar to the dynamic behavior observed in a lattice with a single defect of the

Case	up	refl	adj	adj2	bottom	bottom2	trans
Steel (num)	4.15	1.57	4.30	0.00	4.30	0.00	85.68
Steel/TC (num)	4.69	2.05	2.53	1.28	2.53	1.28	85.65
Steel/steel (num)	4.64	2.00	2.86	1.00	2.86	1.00	85.65
Steel/steel (model)	3.98	3.54	1.16	1.50	1.16	1.50	87.17

Table 3.2: Percentages of the input energy redirected in the system in the rows and columns of spheres adjacent to the defects. We define energy "up" as the energy redirected upward in the column of particles above the first defect, "reflected" as the energy reflected back in the impacted chain, "adjacent" as the energy redirected in the right direction in the row adjacent to the impacted chain , "adjacent2" as the energy redirected in the right direction two rows below the impacted chain, "bottom" as the energy redirected downward in the column of particles below the first defect, "bottom2" as the energy redirected downward in the row below the second defect and "transmitted" as the energy transferred in the impacted chain after the defect. The first three rows of the table show the numerical results for three different cases: the single steel defect case, the cases where a second tungsten carbide defect is placed diagonally with respect to the first one, or the case where a steel defect is placed diagonally with respect to the first one. The last row corresponds to the semi-analytical rigid body collision model for the case of two steel defect particles.

same material. This can be seen comparing the displacement of the first intruder in the x direction with the displacement of a single defect occupying the same interstice (see Fig. 3.9). However, the presence of a second active defect provides extra stiffness in the system, resulting in a reduction of the amplitude of oscillations.

The addition of a second defect placed diagonally with respect to the first one does not have a significant effect on the energy dispersion. We calculate numerically how the input energy is redistributed in the different chains of the system. For the sake of simplicity, we consider only the cases with stiff defects - stainless steel and tungsten carbide (TC) - for which energy localization can be neglected. The two additional chains in which solitary waves are going to propagate due to the second defect are referred to as "adjacent2" and "bottom2". Because a second defect stiffens the contact between the first defect and its bottom right neighbor, more energy is scattered upward and reflected backward. The results for the steel/steel and steel/TC are presented in Table 3.2.

3.4.2 Rigid Body Collision Model

For this entire section, we use the numbering depicted in Fig. 3.9(a). While this configuration appears to be only slightly more complicated than the single defect configuration, adapting the rigid body collision model presents significant challenges. This is because of the intricate effects of backscatter of beads 2 and 4 and their interplay, especially with bead 3. The begining of the calculation is similar to what was done for the modeling of the interaction of a single defect with a solitary wave: particle 1 first interacts with its right neighbor in the impacted chain and particle 2, and we once again make the assumption to neglect any reflected energy during this first interaction. The transmitted energy is identical to the single defect case (87.17% of the input energy) as this model does not include any stiffening of the contact between the first defect particle and its bottom right neighbor. Particle 2 then interacts with 3 (and 1) which subsequently partitions its energy between 4 and the "adjacent" and "bottom" chains. In order to describe the following collisions, it is useful to look at the numerical results presented in Fig. 3.9(b). After the first interaction of particle 2 with particle 1, the former starts oscillating between particles 3 and 1 (green dashed curve labeled "2" between 0.6 and 0.8 ms) as particle 3 is being pushed towards the second defect. The second defect then starts to oscillate between particles 3 and 5 and particle 3 is pushed back towards the second defect (see black curve labeled between 0.8 and 1.3 ms), and so on. We consequently consider that the two defects are interacting independently and in an alternative fashion with particle 3, for about four oscillations each time (inferred from Fig. 3.9(b)). We also assume that the energy of particle 1 is evenly distributed in the "up" and "reflected" chains, whereas the energy of particle 5 is split between the "adjacent2" and "bottom2" chains (see Fig. 3.9(a)). The results are presented in the last row of Table 3.2 along with the numerical simulation data, and are in fairly good agreement with one another. This approach clearly underestimates the input on the "adjacent" and "bottom chains", as the only contribution in our model comes from the first collision of particle 3 with particle 4 and these two chains, yet is the best we can presently do without using too much feedback from the numerical simulations. We find the relevant analysis to be instructive as a lower bound of the corresponding energy partition complementing the transmitted portion of 87.17%.

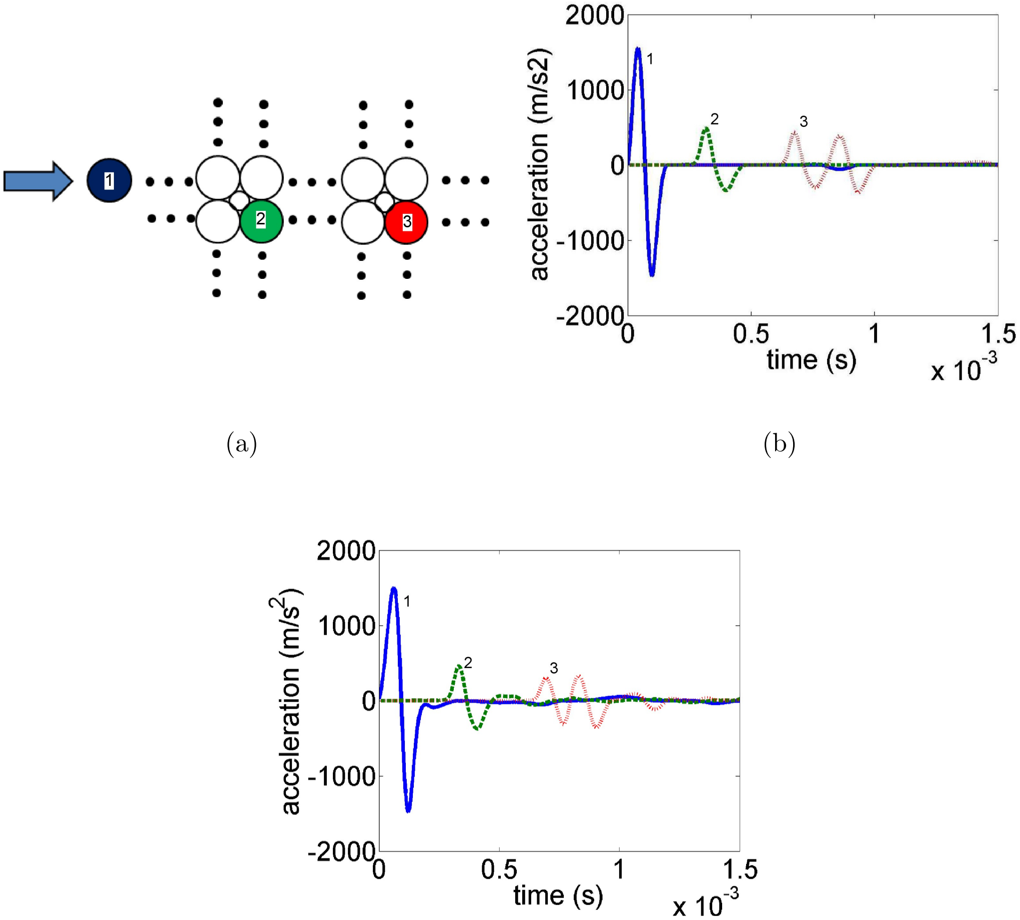

(a)

(b)

(c)

Figure 3.11: Comparison of the output accelerations observed experimentally 3.11(c) and numerically 3.11(b) for the configuration 3.11(a) when two tungsten carbide intruders are located eight interstitial sites apart in a steel square packing impacted by a steel particle. After the incoming solitary wave (blue solid curve labeled "1") interacts with the first defect, two waves travel towards the second defect: a transmitted wave in the impacted chain, and a redirected wave (green dashed curve labeled "2") in the adjacent chain. The red dotted curve labeled "3" shows the two waves propagating after the second defect in the adjacent chain. The colors and labels of the particles correspond to the colors and labels of the acceleration curves in panels 3.11(c) and 3.11(b).

3.4.3 Two Defects in a Line

We study the dynamic response of the granular system, when two defects are placed along the same row of spheres, parallel to the impacted chain. The schematic diagram of this configuration is presented in Fig. 3.1(c). We restrict our study to the case of a steel square packing with two tungsten carbide intruders, impacted by a steel particle. We note that the response of the system is dependent on the relative distance of the defects in the packing: if the two defects are located far from each other, the behavior of the system is similar to that observed for a single defect. In this case, after an incoming solitary wave interacts with the first defect, two solitary waves propagate towards the second defect: a transmitted wave traveling in the row of particles impacted by the striker, and a redirected wave, traveling in the row of particles parallel to it (and immediately below it). According to what was shown in the single defect case, these two waves have different amplitudes, and hence different velocities. Consequently, these waves reach the second defect separately, and the two defects act independently of each other. The energy redirection properties of the system are greatly improved as we observe a geometrical decrease of the leading traveling energy in the impacted chain: as shown in the single defect study, a TC intruder deflects 17.7% of the total input energy. This corresponds to 82.3% of the total initial energy propagating in the impacted chain after the first intruder. 67.7% (or 82.3% of the remaining energy) of the total initial energy will propagate in the impacted chain after the second TC intruder, and so on if more intruders are present. Hence, it is possible, for sufficiently many well separated intruders to obtain a transmitted energy fraction as small as desired according to the following prescription. To ensure that the transmitted fraction is smaller than α, then the number of intruders N that must be used is $N \geq [\log(\alpha)/\log(0.823)]$, where the bracket stands for the integer part.

If the two defects are sufficiently close, the waves transmitted in the impacted chain after the first intruder and in the chain parallel to it will not reach the second intruder separately. This leads to more complex dynamics of the second intruder as it interacts with two solitary waves of different amplitudes at the same time. Moreover, the two solitary waves reach the second intruder from different sides (which is also true when the two defects are far apart), inducing a disordered motion as the defect is simultaneously pushed up and down with different forces.

Numerical calculations and experiments were run to estimate the minimum spacing l necessary for two defects to be independent. This distance is expected to depend on the velocity of impact, as well as the material of the defect particles, which both affect the velocity of the transmitted and forward scattered solitary waves. We denote by r_t the force amplitude ratio between the amplitude of the wave transmitted in the impacted chain after the intruder and the amplitude of the incoming wave (in the impacted chain before the intruder), and by r_s the force amplitude ratio between the amplitude of the wave redirected in the chain parallel to the impacted chain and the amplitude of the incoming wave. Assuming that the force-velocity scaling relation $v \, \alpha \, F^{1/6}$ [3] is valid for effectively 1D systems [102], we obtain the following relationship relating the incoming signal velocity v to the transmitted wave velocity v_t and the redirected wave velocity v_s:

$$v_t - v_s = (r_t^{1/6} - r_s^{1/6})v. \tag{3.6}$$

In order to verify that the pulses detected in our system are solitary-like, we monitored the shape of the propagating signals before and after the interaction with the defect. We noted that the pulse shape remains constant as it travels down the various chains. An example is given in Fig. 3.10 where we compare the shapes of the acceleration signal in the “adjacent” chain five particles after the intruder (solid red curve) and nine particles after the defect (black square markers). As one can see, their shapes are identical and the two curves completely overlap. We also compared the shape of these two curves to the predicted analytical shape for a solitary wave (the Nesterenko’s solution obtained for 1D homogeneous systems - green dashed curve in Fig. 3.10). We observe that the shapes of the two signals (numerical solution and analytical solution) are very close. At the intuitive level, this can be justified as follows. For each row of the 2D chain, the traveling wave propagates without affecting the other rows (as an effectively 1D entity). Hence, both before and after the interstitial defect, we have effectively quasi-1D chains along which genuine traveling waves can propagate. The only redistribution of energy occurs at the defect, which routes that energy into transmitted (along the various directions, as explained by the particle model) and reflected. Once this routing process is completed, naturally the energy reorganizes itself into traveling waves along these effectively 1D directions. It is consequently justified to use the scaling relation previously mentioned.

Since the velocity of the incoming wave depends weakly on the force amplitude, and hence on the velocity of impact, we expect to see a small effect of the impact velocity on l. The two ratios r_t and r_s depend on the Young's modulus of the intruder E_{defect}, r_t being a decreasing function and r_s an increasing function of E_{defect}, so that l increases with E_{defect}. For the range of impact velocities experimentally investigated (0.05 to 0.2 m/s), l was found to be around nine to ten particle diameters. Numerical and experimental results are shown in Fig. 3.11 and Fig. 3.12, for the two cases where the defects are eight and ten interstices apart. As one can see, when located eight interstices away from each other, one cannot distinguish between the end of the first wave and the beginning of the second one (red curve). This becomes possible, however, when the spacing is set to ten interstices. When placed closer to each other, the two defects start to interact, and the behavior of the second defect becomes more complicated, as its interaction with the (fast) transmitted wave and the (slow) scattered wave in the adjacent chain overlap. Preliminary numerical and experimental results showed that in the extreme case where spherical defects are located in all interstitial spaces in a line, one can achieve coupling of the impacted and adjacent chain and equipartition of the input energy in those two chains.

3.5 Summary

In this chaper, the interaction of a solitary wave with spherical interstitial defects placed in an uncompressed, 2D square packing of stainless steel spheres is studied,

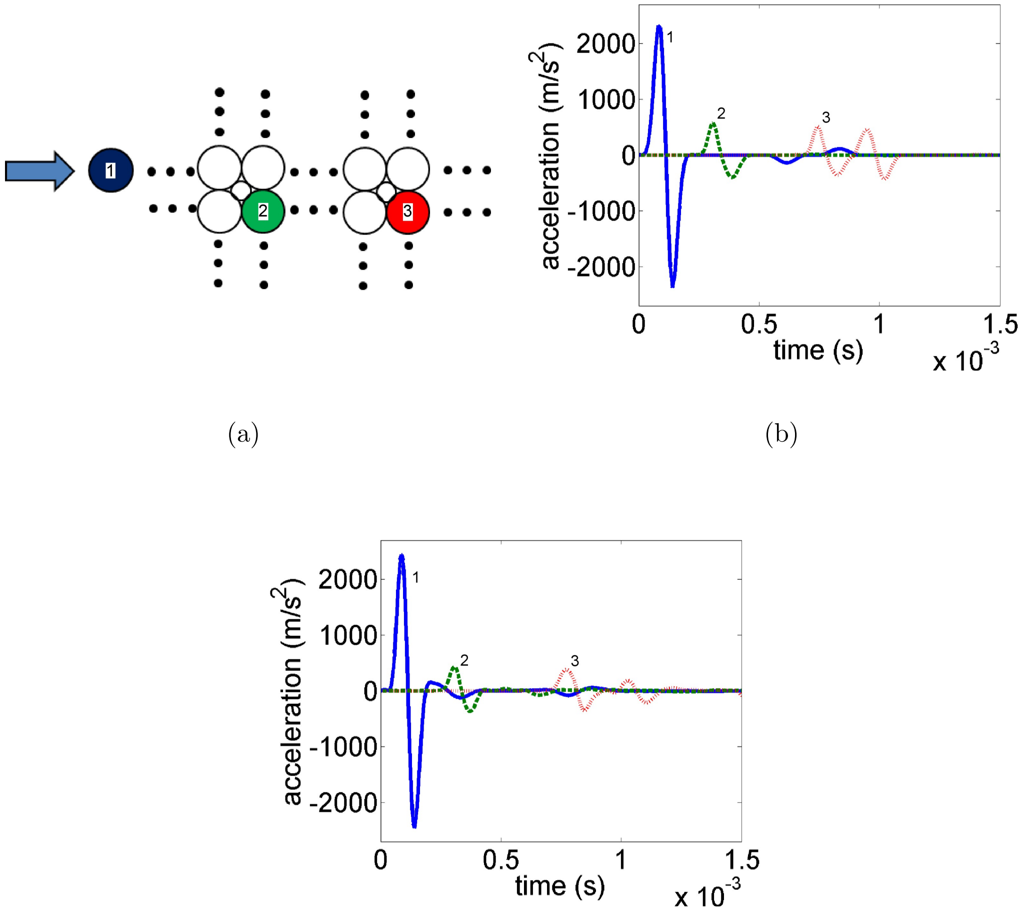

(a)

(b)

(c)

Figure 3.12: Comparison of the output accelerations observed experimentally 3.12(c) and numerically 3.12(b) for the configuration 3.12(a) when two tungsten carbide intruders are located ten interstitial sites apart in a steel square packing impacted by a steel particle. After interaction of the incoming solitary wave (solid blue curve labeled “1”) with the first defect, two waves travel towards the second defect: a transmitted wave in the impacted chain, and a scattered wave (green dashed curve labeled “2”) in the adjacent chain. The red dotted curve labeled “3” shows the two waves propagating after the second intruder in the adjacent chain. The colors and labels of the particles correspond to the colors and labels of the acceleration curves in panels 3.12(c) and 3.12(b).

investigating in a first time the effect of a single defect in the packing. The numerical calculations and experimental results show that spherical defects redirect part of the impact energy, in four directions along the rows and columns of particles in contact with the defect. The defect particle's stiffness plays an important role in the impact energy redirection in the system, and the mass of the defect and the velocity of impact have a much smaller effect on the impulse redirection. A soft defect particle spatially localizes a small percentage of the incoming energy in the crystals, as it oscillates between its nearest neighbors. A stiffer defect particle redirects part of the incoming energy into single deflected and reflected solitary waves, and a simple rigid particle collision calculation was constructed for this case which describes the reflected, scattered and transmitted energy fractions in good agreement with numerical simulations and experimental results. The setting of two defects placed in different configurations in the packing was also analyzed and it was noted that the energy redirection efficiency of the system, measured as the amount of input energy not traveling along the impacted chain, is greatly enhanced when placing multiple defects in a line. If the defect particles are located far enough from each other (around nine to ten particles in our study), then they act independently and their individual behavior is identical to a single defect isolated in a square packing. This enabled a specific prediction for ensuring that the transmitted fraction stays below a prescribed fraction of the original energy. If the defect particles are located close to each other, their dynamic response is influenced by the respective presence.

The work presented in this chapter provides a fundamental understanding of the effect of a single defect in 2D granular crystals, and paves the way to more complex analyses involving a larger number a defect particles and especially a deeper understanding of their complex interplay, as can be seen in the next chapters of this thesis, applying topology optimization techniques in particular [13].

Chapter 4

Energy Equipartition in Two-Dimensional Granular Systems with Light Spherical Intruders

We study the effects of a line of spherical interstitial particles (or intruders) placed between two adjacent uncompressed chains of larger particles in a square packing of spheres, using experiments and numerical simulations. We excite one of the chains of particles adjacent to the intruders with an impact and show how energy is transmitted across the system until equipartition is reached from the excited (or impacted) chain to the absorbing (or adjacent) chain. The coupling of the two chains, although a purely two-dimensional effect, is modeled by a simplified one-and-a-half-dimensional (1.5D) system in which transverse motions of the particles are neglected.

4.1 Introduction

Granular crystals have been proposed as new structured materials for the control and redirection of stress waves (see for example [12, 63, 103, 119, 123, 124]). The experiments reported in this chapter provide the first observation of energy equipartition between two adjacent and nonlinearly coupled chains of particles. In particular, we show that when one chain is excited by an impulse while the other is as rest, the energy is redistributed between the two chains within a short spatial distance. A similar equipartition phenomenon was studied numerically in an earlier work [125] for weakly coupled chains. This phenomenon is of interest in the creation of new acoustic wave guides, delay lines and stress mitigating materials. Energy transfer and equipartition phenomena in weakly coupled one-dimensional granular chains were studied [125, 126], and in [124] have been studied through a macroscopic realization of the Landau-Zener tunneling quantum effect. The energy equipartition principle is well known for elastic waves. Seismic waves for example have well known regimes where the P and S wave energy density equilibrates in a unique way that is independent of the details of the scattering. Interaction of solitons in coupled nonlinear lattices (scalar models) have been considered for various classical configurations such as coupled Toda lattices [127], coupled nonlinear Schrödinger equations [128, 129] or coupled Ablowitz-Ladik chains [130] for example. In the case of coupled Toda lattices, it was shown numerically that solitonic excitations supplied to each one of the coupled chains may result in the two distinct dynamical regimes (attractors) [127]. A non-uniform initial excitation (solitons with different amplitudes and/or phase mismatches) may lead to the formation of the identical solitons on each one of the chains, propagating with the same speed and zero phase mismatch (first attractor) as well as the formation of two unequal solitons (i.e. with different amplitudes and phases also propagating with the same speed, second attractor). Here, we report an extension of energy equipartition phenomena in 2D granular media perturbed by lines of intruders.

4.2 Experimental Setups

Two experimental setups were designed to study the response of a 2D square packing of elastic spheres with the presence of a line of interstitial defects (or intruders) for the two configurations presented in 4.1.

The first one (see Fig. 2.2) is presented in section 2.1.1.1 and consists of a polycarbonate base and four delrin walls that support and enclose a 20×20 granular crystal composed of 316 stainless steel spheres ($R = 9.52$ mm radius). A line of tungsten carbide spherical intruders ($R_d = 3.943$ mm ± 0.001 mm) was placed in between the excited and absorbing chains, lying on custom-made PTFE cylindrical stands to ensure that the centers of mass of all the particles are in the same horizontal plane.

The second one (see Fig. 2.3) is presented in section 2.1.1.2 and consists of a "Vero White" channel that contains two rows of steel particles (radius R) and built-in cylindrical stands to support the tungsten carbide intruders (radius R_d). Two modules were connected and we assembled a 40×2 square packing in which every other interstitial site was occupied by an intruder particle.

In both experiments, the system was impacted from one side by a steel striker particle identical to the ones composing the square packing, and custom-fabricated sensor particles were used to access the acceleration at every location of interest in the crystal (red particles in Fig. 4.1). The sensor particles and data acquisition equipment is described in detail in sections 2.1.2 and 2.1.3 respectively. The experimental accelerations were then directly compared with the ones obtained from numerical simulations.

4.3 Numerical Setup

We numerically model our square packing plus the intruders and one striker particle via the discrete particle model described in section 2.2. The nonlinear equation of motion (Eq. 2.1) is directly integrated using an explicit fourth order Runge-Kutta scheme.

4.4 Results and Discussion

4.4.1 Monomer Configuration

We first present the results obtained for the monomer configuration shown in Fig. 4.1(a) where tungsten carbide intruders are located in every interstitial site between the excited and absorbing chains. We study the temporal evolution of the transmitted acceleration along the x direction in the chains of particles adjacent to the intruders

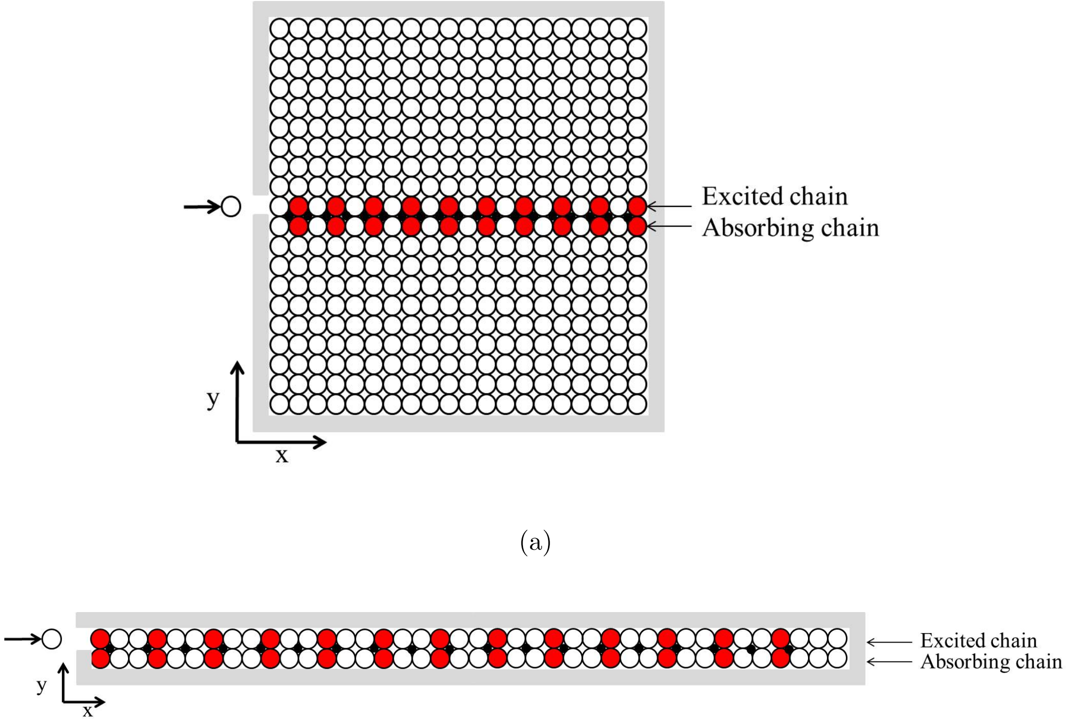

(a)

(b)

Figure 4.1: Schematic diagram of the experimental setups for 4.1(a) the monomer configuration and 4.1(b) the dimer configuration. The small (black) particles correspond to the spherical intruders. The red (gray) particles show the positions chosen for the placement of the sensor particles.

(Fig. 4.2). We compare results obtained from experiments (Fig. 4.2(a) and Fig. 4.2(b)) with the corresponding numerical simulations (Fig. 4.2(c) and Fig. 4.2(d)). Each curve corresponds to a different sensor location placed in all even particles in the impacted chain and in the chain adjacent to the intruders (Fig. 4.1(a)). Without the presence of the line of intruders, a solitary wave forms and propagates along the excited chain (pseudo 1D case, see [102]). The presence of intruders introduces a nonlinear coupling between the two chains, leading to reciprocal energy and momuntum transfer between them. We observe in experiments and numerical simulations that the input energy of the leading propagating pulse (minus what is radiated in the transverse chains) is equally split between the excited and absorbing chains after approximately eight particles, as two distinct pulses with similar velocity and am-

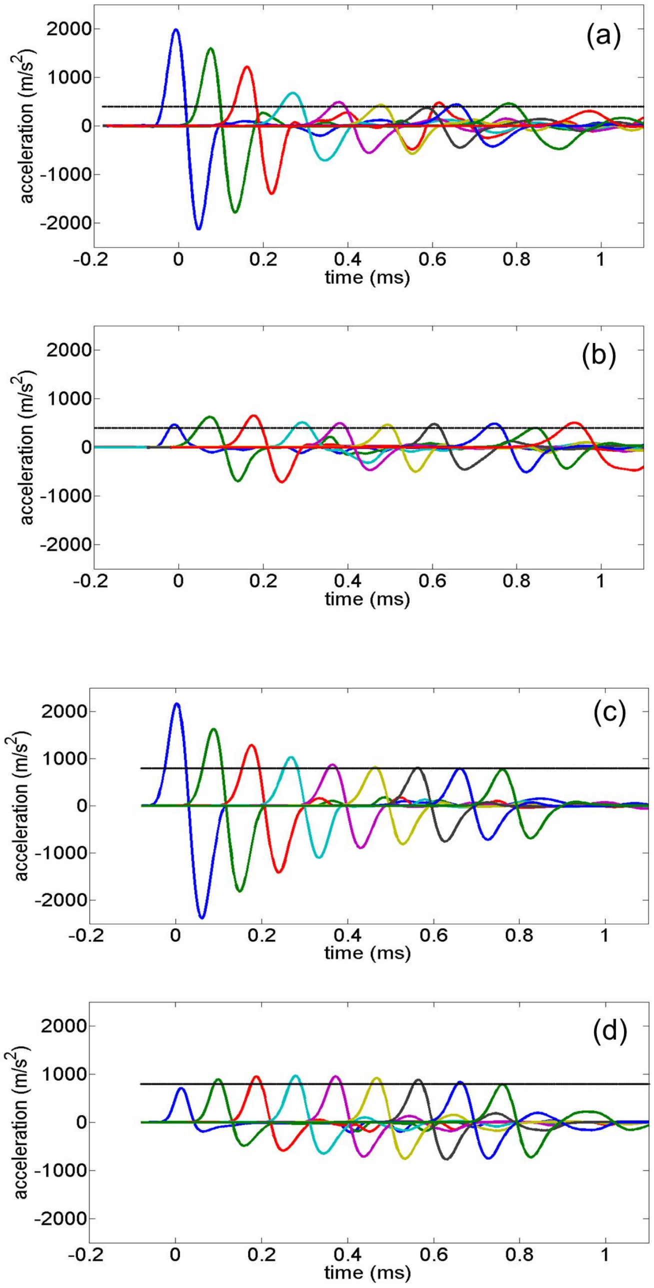

Figure 4.2: Acceleration-time diagrams showing the evolution of the transmitted signal in the two chains of particles adjacent to the line of intruders for the monomer configuration, along the x direction. (a) Experimental results in the excited chain (at all even particles in the chain). (b) Experimental results in the absorbing chain. (c) Numerical data corresponding to (a). (d) Numerical data corresponding to (b). In all panels, the system is impacted by a stainless steel sphere of radius 9.52 mm with initial velocity 0.147 m/s. The horizontal black lines show the stabilized amplitude of the leading acceleration pulse ($\approx$ 800 m/s^2 in the numerical simulations and 400 m/s^2 in the experiments).

plitude form and propagate down the two chains. We use the term "equipartition" to describe the phenomenon of equal division of energy and momentum between two adjacent granular chains, after one of the two is excited by an impulse.

The intruders are also responsible for the scattering of energy in the y direction, and we observe the formation of solitary waves travelling perpendicular to the excited and absorbing chains. For each particle in these two chains, the amplitude of the velocity in the y direction is small ($\approx 20\%$) in comparison to that in the x direction. This corresponds to $\approx 4\%$ of the kinetic energy, and we neglect the leakage of energy in the transverse direction.

The amplitude of the wave traveling in the excited chain decreases drastically within the first few particles as energy is transfered to the absorbing chain through each light intruder. It was shown in [121] that 82.3% of the energy of a solitary wave reaching a TC intruder is transmitted along the chain after interacting with the intruder. The rest of the energy is scattered in adjacent and perpendicular chains, or reflected. Reversely, the amplitude of the wave propagating in the absorbing chain increases from zero to the same level as the signal in the excited chain. It is important to note that these systems are tunable: the material selected for the intruders affects the speed of the energy transfer since weaker interactions between the line of intruders and the excited and absorbing chains will result in a slower transfer of energy. Numerical simulations and experiments were also performed for a line of Teflon defect particles (Young modulus 1.26 GPa) in order to evidence this effect (not shown here).

We find excellent agreement between our numerical and experimental results (compare Fig. 4.2(a) with Fig. 4.2(c) for the excited chain; Fig. 4.2(b) with Fig. 4.2(d) for the absorbing chain). The effect of dissipation is visible in the experimental data, and the stabilized amplitude reached in the two chains in experiments is smaller than in our numerical calculations. After equipartition, we observe in the numerical data a slow decrease of the amplitude of the two waves, due to radiations in the y direction, as the central light intruders push the heavy steel particles away from the centerline. Although we expect the same effect to be present in the experimental data, it is difficult to determine how much of the loss is accounted for by the radiations versus dissipation.

4.4.2 Dimer Configuration

Several extensions to this work are possible and we expect to observe similar equipartition phenomena with intruders made of different materials or between more than two chains for example. In this section, we present the experimental and numerical results obtained when tungsten carbide intruders are located in every other interstitial site between the excited and absorbing chains (Fig.4.1(b)). We refer to this configuration as the dimer configuration.

As for the monomer configutarion, we study the temporal evolution of the transmitted acceleration along the x direction in the chains of particles adjacent to the intruders (Fig. 4.3) and compare the results obtained from experiments (Fig. 4.3(a) and Fig. 4.3(b)) with the corresponding numerical simulations (Fig. 4.3(c) and Fig. 4.3(d)). The same observations can be made for the dimer configuration and these results show that equipartition is a robust phenomenon that is still observable when the density of intruders is decreased: the input energy is progressively transfered from the excited chain to the absorbing one, only at a slower rate. Equipartition is reached after approximately 16 particles or twice the distance needed for the monomer configuration.

In the next section, we present a new analytical model which explains how this fully 2D phenomenon can be described by a simplified 1.5D system, and compare this simplified theoretical model to our experimental and numerical results for the 2D system (similar in form to the one studied in [124–126]). We consider the monomer configuration only.

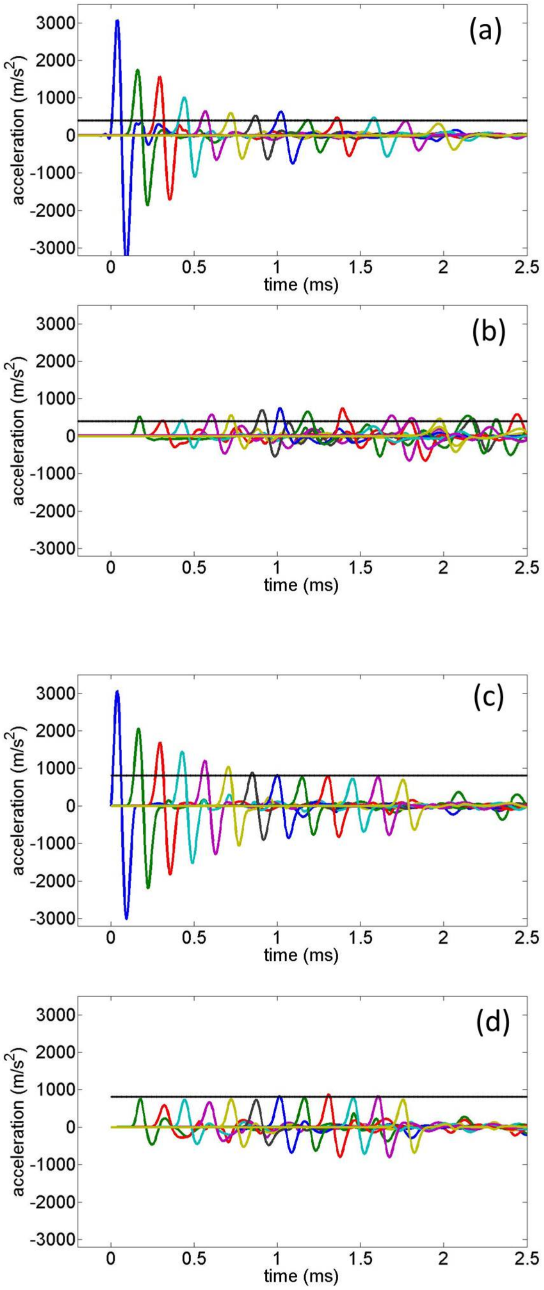

Figure 4.3: Acceleration-time diagrams showing the evolution of the transmitted signal in the two chains of particles adjacent to the line of intruders for the dimer configuration, along the x direction. (a) Experimental results in the excited chain (at all even particles in the chain). (b) Experimental results in the absorbing chain. (c) Numerical data corresponding to (a). (d) Numerical data corresponding to (b). In all panels, the system is impacted by a stainless steel sphere of radius 9.52 mm with initial velocity 0.161 m/s. The horizontal black lines show the stabilized amplitude of the leading acceleration pulse (≈ 800 m/s^2 in the numerical simulations and 400 m/s^2 in the experiments).

4.5 Simplified 1.5D Modelization and Comparison with Full 2D System

Upon arrival of the incoming pulse, the presence of each intruder induces a displacement of the two larger spheres located after it in both the x and y directions. However, the amplitude of the waves traveling in the y direction is small. In our model, we neglect the energy loss in the y direction, constraining the particles of the excited and absorbing chains, and the intruders, to move only horizontally. For simplicity, we limit our analysis to modeling the dynamics of the intruders and the particles of the excited and absorbing chains. Although all particles are contrained to move in the x direction, energy transfer between the excited and absorbing chains in the y direction is still possible due to the strongly nonlinear coupling induced by the line of intruder (1.5D system).

We denote by m, ν, E and ρ the mass, Poisson's ratio, Young's modulus and density of the heavy steel particles. The same quantities with subscript d correspond to the properties of the light TC defect particles. We then use the normalized displacement $x = \frac{X}{R}$ and time $\tau = t\sqrt{\frac{E}{\pi R^2 \rho}}$ to rewrite the set of equations (2.1) into the non-dimensional equations describing the motions of the intruders (4.1), the particles composing the excited chain (4.2) and particles composing the absorbing chain (4.3):

$$\begin{aligned} \epsilon x_i^{d\prime\prime} &= \beta\left[f(x_i^e - x_i^d) - f(x_{i+1}^a - x_i^d)\right] \\ &\quad + \beta\left[f(x_i^e - x_i^d) - f(x_{i+1}^e - x_i^d)\right], \end{aligned} \tag{4.1}$$

$$\begin{aligned} x_i^{e\prime\prime} &= \beta\left[f(x_i^e - x_{i-1}^d) - f(x_i^e - x_i^d)\right] \\ &\quad + \alpha\left[g(x_{i-1}^e - x_i^e) - g(x_i^e - x_{i+1}^e)\right], \end{aligned} \tag{4.2}$$

$$x_i^{a\prime\prime} = \beta\left[f(x_{i-1}^d - x_i^a) - f(x_i^a - x_i^d)\right] + \alpha\left[g(x_{i-1}^a - x_i^a) - g(x_i^a - x_{i+1}^a)\right], \tag{4.3}$$

where $\alpha = \frac{1}{2\sqrt{2}(1-\nu^2)}$, $\beta = \sqrt{\frac{2-\sqrt{2}}{2}}\frac{E_d}{E(1-\nu_d^2)+E_d(1-\nu^2)}$ and $\epsilon = \frac{m_d}{m}$ is our small parameter. We used $f(x) = \left(\sqrt{2}-\sqrt{x^2+1}\right)_+^{3/2}$ and $g(x) = (x+2)_+^{3/2}$, x is the scalar non-dimensional displacement of the particles (constrained in the x direction), and x'' represents the second derivative with respect to the normalized time τ. The superscript d corresponds to the defect particles, e corresponds to the particles in the excited chain, and a to the particles in the absorbing chain. The subscript i indicates the position of every particle in their chains, oriented along the positive x axis.

For the materials chosen in our study, $\epsilon = 0.134$, $\beta = 1.022$ and we assume the ratio $\frac{\epsilon}{\beta}$ to be small enough to neglect the inertia of the intruders. Equating the right term of Eq. (4.1) to zero leads to:

$$f(x_i^e - x_i^d) - f(x_i^d - x_{i+1}^a) = -[f(x_i^a - x_i^d) - f(x_i^d - x_{i+1}^e)]. \tag{4.4}$$

We numerically showed that the two sides of Eq. (4.4) are independently small and we can consequently assume:

$$\begin{aligned} f(x_i^e - x_i^d) &\approx f(x_i^d - x_{i+1}^a), \\ f(x_i^a - x_i^d) &\approx f(x_i^d - x_{i+1}^e). \end{aligned} \tag{4.5}$$

This means that, to a first order approximation, the diagonal forces applied on a defect particle are independent from each other. Eq. (4.5) yields:

$$x_i^d \approx \frac{x_i^e + x_{i+1}^a}{2} \approx \frac{x_i^a + x_{i+1}^e}{2}. \tag{4.6}$$

Further analytical treatment assumes that the right-hand side and left-hand side of Eqs. (4.5) and (4.6) are equal. We can replace x_i^d and x_{i-1}^d in Eqs. (4.2) and (4.3) to

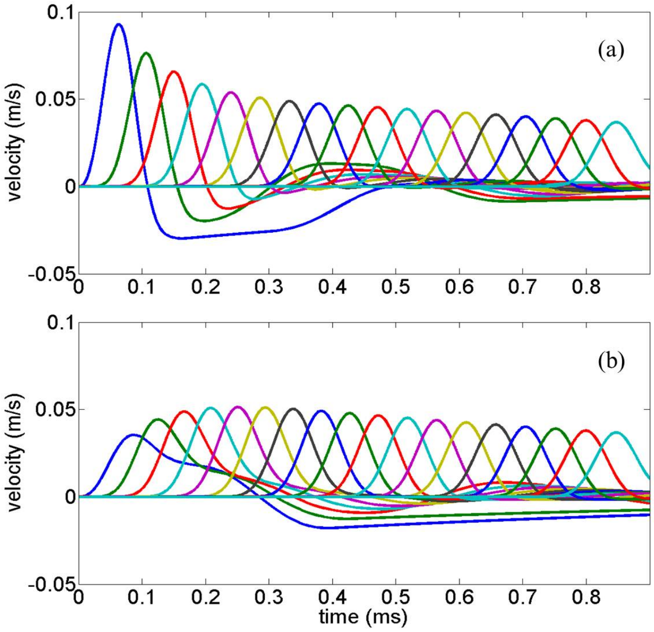

Figure 4.4: x-velocity *vs* time signals obtained for the 1.5D model with linear damping coefficient λ equal to 0.006. Each curve represents the velocity of every particle in the excited chain (a) and the absorbing chain (b). The system is impacted by a stainless steel sphere of radius 9.52 mm with initial velocity 0.147 m/s.

obtain a system of equations for the excited and absorbing chains only. To incorporate the radiation effect, we finally add a linear damping term in order to account for the decay caused by the energy leakage in the transverse direction:

$$\begin{aligned} x_i^{e\prime\prime} &= \beta \left[f\left(\frac{x_{i-1}^a - x_i^e}{2}\right) - f\left(\frac{x_i^e - x_{i+1}^a}{2}\right)\right] \\ &\quad + \alpha\left[g(x_{i-1}^e - x_i^e) - g(x_i^e - x_{i+1}^e)\right] - \lambda x_i^{e\prime}, \end{aligned} \tag{4.7}$$

$$\begin{aligned} x_i^{a\prime\prime} &= \beta \left[f(x_{i-1}^e - x_i^a) - f(x_i^a - x_{i+1}^e)\right] \\ &\quad + \alpha\left[g(x_{i-1}^a - x_i^a) - g(x_i^a - x_{i+1}^a)\right] - \lambda x_i^{a\prime}. \end{aligned} \tag{4.8}$$

We used a vectorized fourth order Runge-Kutta scheme to integrate this simplified set of equations. The numerical setup consists of two adjacent chains of 20 particles

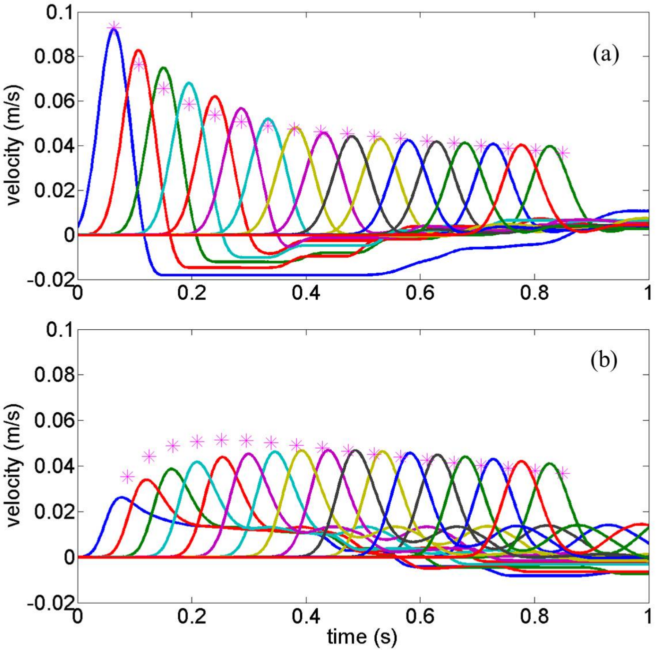

Figure 4.5: Comparison of the numerical x-velocity *vs* time signals obtained from the 2D and simplified 1.5D models (from Fig. 4.4). The results for the excited chain are shown in (a), and (b) shows the results for the absorbing chain. In both plots, the curves are obtained from the 2D model, whereas the (purple) stars indicate the peak amplitudes of the corresponding signals obtained from the 1.5D model.

each (absorbing and excited chains) and 19 interstitial intruders. Similarly as before, the walls are modeled as fixed spherical particles of infinite radius. The excited chain is impacted by a striker particle with initial velocity obtained from experiments. We show the numerical solution in Fig. 4.4. We clearly observe the energy equipartition previously evidenced in our experiments and in the fully 2D numerical simulations. Similarly to what observed earlier, also in the 1.5D model the velocity stabilizes in the two chains after approximately eight particles.

The results obtained from the simplified 1.5D model are compared with the fully 2D system in Fig. 4.5. The only fitting parameter used in the 1.5D model is the linear damping coefficient λ (dimensionless), which is taken to be 0.006. The results show that the 1.5D approximation captures very well the main features of the 2D system: the energy equipartition is reached after the same number of particles, and the amplitudes of the leading pulses are in very good agreement.

4.6 Summary

In this chapter we showed with experiments and numerical simulations that the mechanism of solitary wave equipartition previously observed in linearly coupled, nonlinear lattices persists in full 2D granular setups with a more complex type of coupling (strongly nonlinear, non-smooth, diagonal coupling via light interstitial intruders). This energy equipartition phenomenon could be used for the creation of novel acoustic delay-lines, wave guides and protective materials. The regime of the primary pulse transmission in the strongly-nonlinear, heterogeneous, 2D granular crystal is well captured by our simplified, reduced order model (granular scalar model). The results of the present work will pave way for further analytical, numerical and experimental studies of the mechanisms of energy transfer and wave redirection in higher dimensional granular crystals. Moreover, the mechanism of equipartition of solitary pulses in granular crystals realized through the placement of interstitial intruders is of great practical importance in the design of granular shock absorbers able to efficiently distribute the initially localized shock over the entire granular medium.

Chapter 5

Topology and Material Optimization of Two-Dimensional Granular Crystals Using Gradient-Based Methods

In this chapter, we apply gradient-based optimization methods to the design of new composite granular materials with interesting wave mitigating properties. In a first approach, we investigate the optimal distribution of spherical interstitial intruder particles in an uncompressed square packing of spheres (topology optimization). In a second approach, we optimize the material distribution in hexagonal packings where each particle can be composed of either a stiff or soft material. In both cases, our goal is to create designs that minimize or maximize a given objective function (e.g. total energy or reaction force) in a prescribed part of the system, when the latter is subject to an impact. Specific problems (e.g. dispersion, focusing, shielding) were studied to prove the efficiency of the design method and the numerically obtained optimized designs were compared to several benchmark cases. Finally, we successfully performed experimental verifications to validate the practical feasibility of such designs.

5.1 Introduction

Under normal conditions of impact, it was shown that a 2D square packing behaves as a pseudo-1D system [102]. However, as described in chapters 3 and 4, when an intruder (also referred to as defect particle) occupies an interstitial site in the wave propagation path, we observe the formation of reflected and scattered waves traveling in the various chains of particles in contact with this defect particle [121]. This highly directional response can be used as a basis to design granular crystals with predetermined wave propagation paths capable of mitigating stress wave energy.

To these ends, we propose a topology optimization scheme [13, 132] to tailor the energy propagation in 2D granular crystals under impact loads. Topology optimization, and more specifically gradient-based approaches, is a highly developed tool for structural optimization. We present the first application of this method to granular crystals. In our model, each interstitial site can be occupied by a spherical intruder. The presence (or absence) of the intruder is characterized by a volume fraction, and we use topology optimization to optimize the material distribution in these interstitial sites.

Our goal is to obtain optimized discrete (or 0/1) designs in which each interstitial site is either empty or occupied by an intruder, and we consequently investigate different approaches to penalize intermediate values for the volume fraction. One approach is to employ the Solid Isotropic Material with Penalization (SIMP) method, in which intermediate densities are suppressed by making them a “costly” design [133, 134]. Another approach is the Sum of Reciprocal Values (SRV) method, which uses an additional optimization constraint to remove intermediate densities in the domain [135, 136]. We also penalize intermediate density values by adding a penalty term in the objective function. To accomplish wave tailoring, we define two types of objective function: the total energy in a prescribed area of the domain and the interaction force between the beads and the enclosing walls. The goal of our transient topology optimization scheme is to find the distribution of intruders in the domain that minimizes (dispersion) or maximizes (focus) one or a combination of these given objective functions.

A second part of the work presented in this chapter consists of implementing a similar optimization scheme that optimally selects the material properties of each particle in a hexagonal packing. In this case, we intend to create designs with similar abilities by taking advantage of the material distribution instead of the particle location. Non discrete designs are easier to interpret physically, as we can potentially find an existing material corresponding to an in-between value selected by the optimizer, but are still less desirable for practical reasons and intermediate stiffnesses can again be penalized by adding a penalty term to the objective function.

We validate our numerical results with experimental data. New experimental setups were designed and experimental data was collected using mini tri-axial accelerometers embedded in selected beads. This provides us with local experimental accelerations that are then directly compared to the numerical outputs, with excellent agreement.

The work presented in this chapter illustrates how to optimally use multi-scattering and different material phases in organized granular crystals to mitigate or focus the energy originating from an impact and could lead to the creation of efficient designs for new composite structures with targeted wave tailoring applications: protection from explosives and impact pulses or wave guides for example.

The rest of this presentation is organized as follows. In Sec. 2, we present the model at hand. In Sec. 3, we describe in detail the optimization problem and numerical setup. The numerical results are presented in Sec. 4. We demonstrate the abilities of our numerical setup by looking at two sample problems for the topology optimizations (a dispersion problem in which we minimize the energy at the wall opposed to the impact and a deflection problem in which we maximize the energy redirected in the middle sections of the side walls) and three sample problems for the material optimization (minimization of the peak energy at the center of the system, at the wall opposed to the impact and maximization of the energy at the side walls). Sec. 5 contains a description of the experimental setups used to verify the numerical results as well as a comparison of numerically obtained optimized designs with real systems. Finally, in Sec. 6, we present some conclusions and possibilities for further studies.

5.2 Model

In this work, we investigate the dynamic response of square and hexagonal packings of spherical beads impacted on one side by a striker particle. A finite element approach described in section 2.2 is taken using two-node elements that connect the centers of every pair of adjacent particles. In the absence of body loads, the governing equations for the nonlinear elastodynamic is given in a semi-discrete form by Eq. 2.2, and $F_{ext} = 0$ in this study. A implicit Newmark integration scheme [107, 108] is used to time discretize the equations of motion and solve for the displacements, velocities and accelerations at every time step (see Eq. 2.3).

5.3 Optimization Problem

5.3.1 General Formulation of the Optimization Problem

We perform topology and material optimizations using a gradient-based approach. In the first case, we optimize the positions of intruder particles occupying the interstitial sites in a square packing in order to minimize or maximize a given physical cost (or objective) function. In the second case, we achieve the same goal optimizing the material properties of the particles composing a hexagonal packing. Topology optimization problems are by nature discrete problems, and are commonly relaxed to continuous ones. In both cases, we can write the general formulation of the continuous optimization problem as follows:

$$\min_{x} f(x)$$
$$s.t. \begin{cases} g_k(x) \le \overline{g}_k & k = 0, ..., M \\ x^{min} \le x_i \le x^{max} = 1 & i = 1, ..., N \end{cases}, \tag{5.1}$$

where x is the design variable vector, f is the cost function, M is the number of constraint functions g_k, and N is the number of design variables x_i, constrained to stay within the bounds $x^{min}$and x^{max}. The multiobjective cost function f is given by:

$$f(x) = \sum_{k=1}^{N_{obj}} \alpha_k \left[\sum_{j=1}^{Nt(k)} \left(\sum_{n=1}^{N_{step}} \left(\widehat{f}^{(k)}_{j,n}(x) \right)^T \right)^{S/T} \right]^{1/S}$$

$$\text{with } \widehat{f} = \begin{cases} \text{Total energy} \\ \text{Reaction force} \end{cases} . \tag{5.2}$$

As can be seen from Eq. 5.2, one can choose to optimize a combination of N_{obj} objective functions $\widehat{f}^{(k)}$, α_k taking the value 1 (resp. -1) if the user wants to minimize (resp. maximize) the objective function $\widehat{f}^{(k)}$. $Nt(k)$ represents the number of particles in the k^{th} target area and N_{step} is the total number of time steps for each simulation. The peak value of the total energy or interaction force in the target area over space and time is approximated by nested p-norms with large enough values of the exponents S and T (typically $S = T = 8$). The average value of the same function is obtained by setting $S = T = 1$.

5.3.2 Design Variable and Regularization Techniques

We define our design vector x as the particle volume fraction: a volume fraction equal to zero corresponds to a void (or absence of particle) whereas a volume fraction equal to one corresponds to the presence of a particle, the material of which can be chosen from several preselected ones. Our goal is to obtain discrete designs with only vacant sites, $x_i = x^{min} = 0.001$ or occupied by a particle, $x_i = 1$. In order to use continuous methods, an "artificial-material" model is used where the volume fractions can temporarily take any values between x^{min} and 1. We can also define non-design regions, in which particle positions and/or material properties are known.

In this work, we adopt a "three-phase" material model, in which the material properties of each bead can be interpolated as follows:

$$C_i^H = \xi_i^p(\phi_i^p C^A + (1-\phi_i)^p C^B), \quad x = [\phi_1 \dots \phi_{N/2}\ \xi_1 \dots \xi_{N/2}], \tag{5.3}$$

where $C^{A,B}$ represents the compliance tensors of the two predefined homogeneous materials [137]. This yields:

$$E_i^H = \frac{\mu_i^H\left(3\lambda_i^H + 2\mu_i^H\right)}{\lambda_i^H + \mu_i^H}, \nu_i^H = \frac{\lambda_i^H}{2\left(\lambda_i^H + \nu_i^H\right)},$$
$$\text{with} \begin{cases} \mu_i^H & = \xi_i^p(\phi_i^p \mu^A + (1-\phi_i)^p \mu^B) \\ \lambda_i^H & = \xi_i^p(\phi_i^p \lambda^A + (1-\phi_i)^p \lambda^B). \end{cases} \tag{5.4}$$

The densities are interpolated in a similar manner:

$$\rho_i^H = \xi_i^q(\phi_i \rho^A + (1-\phi_i)\rho^B). \tag{5.5}$$

We investigate two optimization problems. In the first one, the beads area arranged in a square packing of $n \times n$ particles with known radii and material properties, forming the non-design space. Each interstitial site can be either a void or occupied by an intruder. Hence, the design vector is defined by the variables ξ_i and ϕ_i associated to each interstitial site i. In this chapter, we refer to this problem as the “intruder optimization”. In the general case, each design particle can either be a void or a particle made of material A or B (as explained before, intermediate values are also admitted in order to use a continuous method). Prescribing $\phi_i = 1$ for all i, the design vector reduces to the ξ_i and each design particle can be either a void or made of material A (two-phase material model).

The second optimization problem consists of an hexagonal packing without intruders. Here all the beads form the design space. Since the existence of a bead is no longer a variable, we set $\xi_i = 1$ for all i in Eqs. 5.4 and 5.5, and the design vector reduces to the ϕ_i only. Hence, each particle in the system is now made of material A or B (or any intermediate material given by Eqs. 5.4 and 5.5). We denote this problem as the “material optimization”.

For practical reasons, we are not interested in final designs containing gray areas (or “artificial” materials), but would like each design particle to be empty or occupied by baseline materials (denoted by the superscripts A and B). In order to steer the values of the volume fractions back to x^{min} and ones, three methods are implemented. The first one consists in adding a penalization term to the objective function, which can be expressed as:

$$\tilde{f} = f + w \sum_{i=1}^{N} \left(x_i(1-x_i)\right)^2 , \tag{5.6}$$

where w is a weight parameter which is tuned for each optimization problem. The SIMP method [133], originally developed for compliance minimization problems, is also implemented, with good results. Last, one can add an SRV constraint [135] which creates discrete designs with a specified number of occupied sites. This method will be described in more detail in the next section.

5.3.3 Constraints

In the intruder optimization problem, we may want to limit the maximum number of intruders (n_{max}) in the domain. This is particularly interesting when we want to compare the optimized designs with experiments, since configurations containing too many defect particles are significantly more difficult to reproduce experimentally. We limit the number of intruders by limiting the sum of volume fraction, i.e.

$$g_1(x) \leq \overline{g}_1. \tag{5.7}$$

where $\overline{g}_1 = n_{max} + (N - n_{max})x_{min}$.

As mentioned previously, we use the SRV constraint, in order to obtain discrete designs. The sum of reciprocal values function is given by:

$$g_2(x) = \sum_{i=1}^{N} \frac{1}{x_i}. \tag{5.8}$$

Fuchs et al. [135] showed that for a given design vector x that satisfies the equality constraint $g_1(x) = \overline{g}_1$, the function $g_2(x)$ is maximal when x is discrete, i.e., when all entries are equal to x_{min} or 1.

Therefore, in order to obtain a discrete design we set the equality constraint

$$g_1(x) = \overline{g}_1 \tag{5.9}$$

and the inequality constraint

$$g_2(x) \geq \overline{g}_2, \tag{5.10}$$

where $\overline{g}_2 = (1-\eta)\left(n_{max} + \frac{(N-n_{max})}{x_{min}}\right)$ and $\eta = 0.001$ (we use an inequality constraint instead of the equality $g_2(x) = \overline{g}_2$ to avoid numerical errors).

5.3.4 Sensitivity Analysis

To solve Eq. 5.1, we use gradient-based optimization algorithms and thus require the sensitivities of the cost function f with respect to the design parameters to search the design space. We adopt a discrete approach in which the problem is both spatially and temporally discretized, as can be seen from Eq. 5.2. We define the cost function f over the displacements, velocities and accelerations vectors $u^{(n)}$, $v^{(n)}$ and $a^{(n)}$ at every time step n. These response vectors are in turn functions of the design vector x and we write the explicit and implicit dependence of f on x as follows:

$$f(x) = f^*\left(u^{(1)}(x), ..., u^{(N_{step})}(x), v^{(1)}(x), ..., v^{(N_{step})}(x), a^{(1)}(x), ..., a^{(N_{step})}(x), x\right), \tag{5.11}$$

where N_{step} is the total number of time steps.

We express the sensitivity as:

$$\nabla f = Df^* + \sum_{n=1}^{N_{step}} \left(Du^{(n)^T} \frac{\partial f^*}{\partial u^{(n)}} + Dv^{(n)^T} \frac{\partial f^*}{\partial v^{(n)}} + Da^{(n)^T} \frac{\partial f^*}{\partial a^{(n)}} \right), \tag{5.12}$$

where we invoke the chain rule and use the notation DX to denote the derivative of X with respect to the design vector x, i.e., $DX = \frac{\partial X}{\partial x}$. The terms Df^*, $\frac{\partial f^*}{\partial u^{(n)}}$, $\frac{\partial f^*}{\partial v^{(n)}}$ and

$\frac{\partial f^*}{\partial a^{(n)}}$ are directly evaluated as the cost function f^* is explicity defined. The evaluation of the reponse derivatives terms $Du^{(n)}$, $Dv^{(n)}$ and $Da^{(n)}$ is more complicated due to the implicit dependence of the response variables on the design vector. The adjoint method [138] was used to eliminate the implicit derivatives $Du^{(n)}$, $Dv^{(n)}$ and $Da^{(n)}$ and we follow an approach similar to [139] in order to evaluate the left hand side of 5.12.

Adjoint sensitivities are obtained by augmenting the sensitivity expression in Eq. 5.12 with the derivatives of the governing equation and the derivatives of the Newmark update equations 2.3:

$$
\begin{aligned}
\nabla f = Df^* &+ \sum_{n=1}^{N_{step}} \left(Du^{(n)^T} \frac{\partial f^*}{\partial u^{(n)}} + Dv^{(n)^T} \frac{\partial f^*}{\partial v^{(n)}} + Da^{(n)^T} \frac{\partial f^*}{\partial a^{(n)}} \right) \\
&+ \sum_{n=1}^{N_{step}} \lambda_0^{(N_{step}-n+1)^T} \left((-DM)a^{(n)} - DS(u^n) \right) \\
&+ \sum_{n=1}^{N_{step}} \lambda_0^{(N_{step}-n+1)^T} \left(-K_2^{(n)} Da^{(n)} - \frac{\partial S^{(n)}}{\partial u^{(n)}} (1-2\beta) \frac{\Delta t^2}{2} - \Delta t \frac{\partial S^{(n)}}{\partial u^{(n)}} Dv^{(n-1)} - \frac{\partial S^{(n)}}{\partial u^{(n)}} Du^{(n-1)} \right) \\
&+ \sum_{n=1}^{N_{step}} \lambda_1^{(N_{step}-n+1)^T} \left(-Du^{(n)} + Du^{(n-1)} + \Delta t Dv^{(n-1)} + \frac{\Delta t^2}{2} (1-2\beta) Da^{(n-1)} + \beta \Delta t^2 Da^{(n)} \right) \\
&+ \sum_{n=1}^{N_{step}} \lambda_2^{(N_{step}-n+1)^T} \left(-Dv^{(n)} + Dv^{(n-1)} + \Delta t (1-\gamma) Da^{(n-1)} + \Delta t \gamma Da^{(n)} \right),
\end{aligned}
\tag{5.13}
$$

where $\lambda_0^{(n)}$, $\lambda_1^{(n)}$ and $\lambda_2^{(n)}$ are arbitrary adjoint vectors and $K_2^{(n)} = \left(M + \beta \Delta t^2 \frac{\partial S^{(n)}}{\partial u^{(n)}} \right)$.

We rearrange the above equation, factoring the implicit derivative terms and select the arbitrary adjoint vectors that make these terms vanish. We consequently obtain the simplified expression for the desired sensitivities:

$$\begin{aligned}\nabla f = Df^* &+ \sum_{n=1}^{N_{step}} DS(u^{(n)})^T \lambda_0^{(N_{step}-n+1)} \\ &+ \left(Da^{(0)}\right)^T \left(-\frac{\Delta t^2}{2}(1-2\beta)\frac{\partial S(u^{(1)})}{\partial u^{(1)}}^T \lambda_0^{(N_{step})} + \frac{\Delta t^2}{2}(1-2\beta)\lambda_1^{(N_{step})} + (1-\gamma)\Delta t\lambda_2^{(N_{step})} \right) \\ &+ \left(Dv^{(0)}\right)^T \left(-\Delta t\frac{\partial S(u^{(1)})}{\partial u^{(1)}}^T \lambda_0^{(N_{step})} + \Delta t\lambda_1^{(N_{step})} + \lambda_2^{(N_{step})} \right) \\ &+ \left(Du^{(0)}\right)^T \left(-\frac{\partial S(u^{(1)})}{\partial u^{(1)}}^T \lambda_0^{(N_{step})} + \lambda_1^{(N_{step})} \right), \end{aligned} \tag{5.14}$$

where $\lambda_0^{(n)}$, $\lambda_1^{(n)}$ and $\lambda_2^{(n)}$ are the solutions of the adjoint problem,

$$\begin{cases} \lambda_1^{(n)} & = \lambda_1^{(n-1)} + \frac{\partial f^*}{\partial u^{(N_{step}-n+1)}} - \frac{\partial S(u^{(N_{step}-n+2)})}{\partial u^{(N_{step}-n+2)}}\lambda_0^{(n-1)} \\ \lambda_2^{(n)} & = \lambda_2^{(n-1)} + \frac{\partial f^*}{\partial v^{(N_{step}-n+1)}} - \Delta t\frac{\partial S(u^{(N_{step}-n+2)})}{\partial u^{(N_{step}-n+2)}}\lambda_0^{(n-1)} + \Delta t\lambda_1^{(n-1)} \\ K_2^{(N_{step}-n+1)}\lambda_0^{(n)} & = \frac{\partial f^*}{\partial a^{(N_{step}-n+1)}} + \beta\Delta t^2\lambda_1^{(n)} + \gamma\Delta t\lambda_2^{(n)} + (1-2\beta)\frac{\Delta t^2}{2}\lambda_1^{(n-1)} + (1-\gamma)\Delta t\lambda_2^{(n-1)} \\ & \quad -(1-2\beta)\frac{\Delta t^2}{2}\frac{\partial S(u^{(N_{step}-n+2)})}{\partial u^{(N_{step}-n+2)}}\lambda_0^{(n-1)}. \end{cases} \tag{5.15}$$

$Du^{(0)}$, $Dv^{(0)}$ and $Da^{(0)}$ are easily determinated from the imposed initial conditions. We choose $\lambda_0^{(0)} = 0$, $\lambda_1^{(0)} = 0$ and $\lambda_2^{(0)} = 0$ to solve the terminal value problem 5.15.

Fig. 5.1 summarizes the organization of the numerical setup. After selecting an arbitrary initial design vector, we enter the optimization loop. The transient analysis precedes the evaluation of the sensitivities and/or value of cost function. The optimizer (the authors used the commercial nonlinear Knitro solver from Ziena Optimization LLC) then updates the design vector and a test decides if the termination criteria were met (final solution) or not (reenter the optimization loop).

The next section presents numerical results obtained using our numerical setup, focusing mainly on five sample problems.

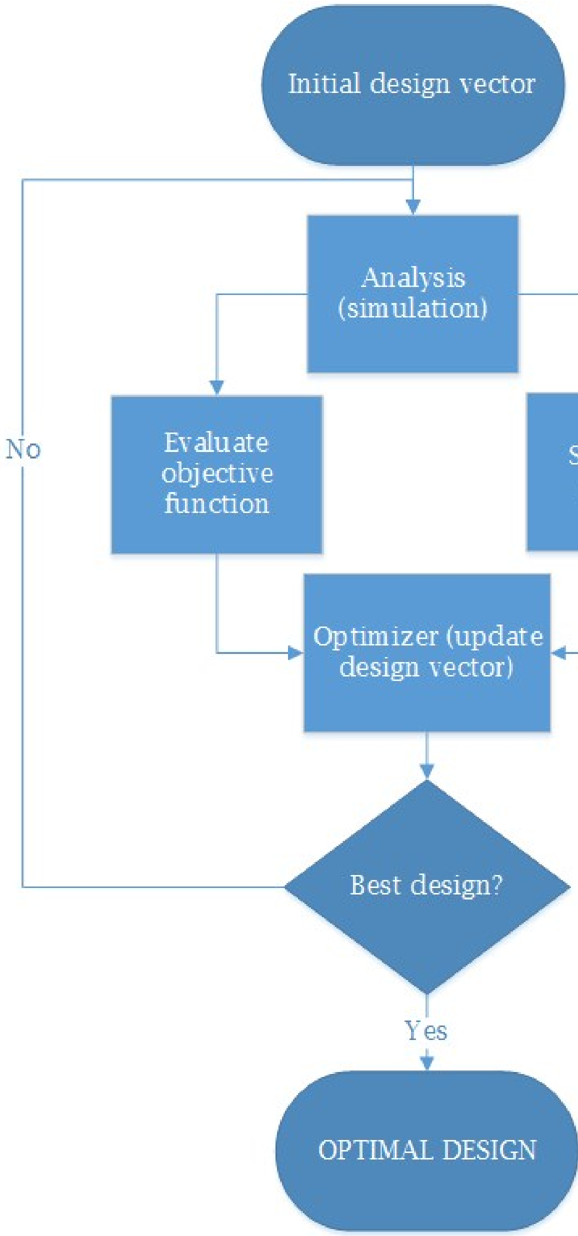

Figure 5.1: Block diagram presenting the structure of the numerical setup.

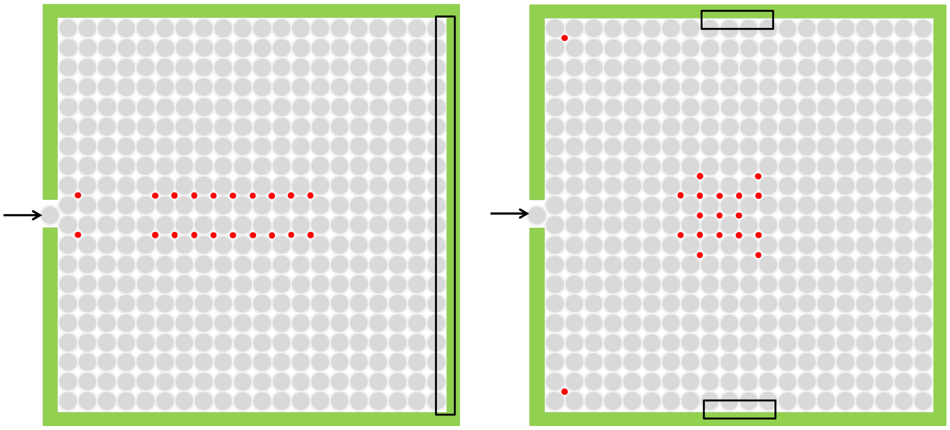

(a) (b)

Figure 5.2: Schematic diagrams of the two topology optimization problems investigated. Both consist of a 20 by 20 stainless steel square packing (grey particles, radius $R = 9.52$ mm) impacted from the left by a particle identical to the ones composing the square packing (black arrow). The tungsten carbide intruders are illustrated in red and the black boxes show the target areas. In 5.2(a), we minimize the peak energy that reaches the wall opposed to the impact. In 5.2(b), we maximize the average energy that reaches the two middle sections of the side walls. Both 5.2(a) and 5.2(b) are the optimized designs obtained when applying the SRV constraint where $n_{max} = 20$.

5.4 Numerical Results

5.4.1 Topology Optimizations (Intruder Problem)

5.4.1.1 Test Cases: Dispersion and Deflection Problems

Two different problems were investigated to test the efficiency of our numerical setup and are presented in Fig. 5.2. We study a square packing of 20 by 20 particles (radius $R = 9.52$ mm). The striker particle is identical to the ones composing the packing and is given some initial velocity v_0. The intruder particles have radius $r = (\sqrt{2} - 1)R$.

In the first problem, we want to minimize the peak force along the wall opposed to the impact (dispersion problem). In the second one, we want to maximize the average energy in the middle parts of the side walls (deflection/focusing problem). In both cases, every interstitial site in the square packing can potentially host a tungsten carbide defect particle. The system is impacted symmetrically from the left. For each case, we present results for unconstrained and constrained optimizations. The constrained designs are obtained for $n_{max} = 20$ and are depicted in Fig. 5.2. We also compare the optimized designs with three different benchmark configurations: no intruders, intruders in every interstitial site and an educated guess consisting of 20 intruders organized in a triangular shape. This choice of educated guess is motivated by the fact that triangular patterns are often seen in our numerical designs and are efficient at dispersing energy by redirecting it to the sides.

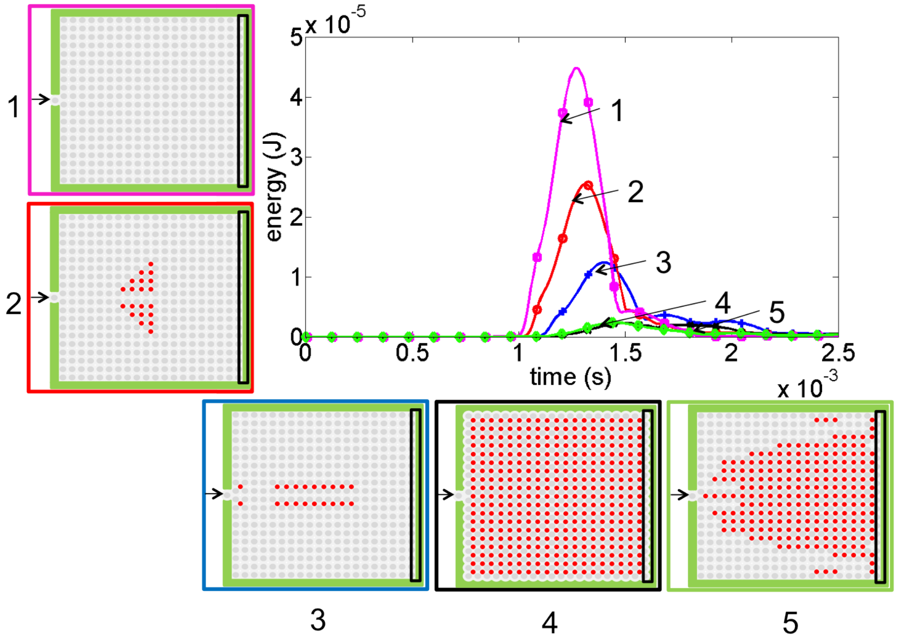

Figure 5.3: Numerical study for the dispersion problem. We plot the peak total energy (i.e. the maximum over the number of elements in the target area) as a function of time. Each curve shows the response of a different design when impacted by a steel particle with initial velocity $v_0 = 0.095$ m/s. The labeling and color of each curve corresponds to the labeling and box coloring of the various configurations around the plot. For each schematic, the gray particles compose the square packing, which is impacted from the left by an identical striker bead. The red dots are the defect particles, and the black boxes show the target area.

The numerical results for the dispersion problem are presented in Fig. 5.3. Starting from the top-left configuration and going counter-clockwise, we present the different designs from the worst configuration to the best. One notes that the numerical setup yields symmetric designs, as we have a symmetric problem (packing, impact and boundary conditions). After impact, two solitary waves of constant amplitude travel in the two central chains [102] (as well as two solitary waves traveling up and down in the first transverse chain). As expected, the worst case corresponds to the configuration without any intruders, as none of the input energy is scattered: the two solitary waves reach the end wall without being perturbed and the peak energy reaching the wall is 4.5×10^{-5} J. The educated guess is almost twice as good as the 20 intruders scatter part of the energy from the two solitary waves ($E_{max} = 2.5 \times 10^{-5}$ J). The constrained optimized design is itself 52% more efficient than the educated guess ($E_{max} = 1.24 \times 10^{-5}$ J). It is interesting to note that the optimizer places the first 20 intruders in two lines, corresponding to a symmetric case of the equipartition phenomenon previously observed in [131]. Placing intruders in every possible location, one obtains an efficient design where the input energy is geometrically diluted as a 2D wave front forms, similar to that described in [103]. This configuration performs almost as well as the unconstrained optimized designs, expected to be the best design, and which requires fewer intruders (in both cases, $E_{max} = 0.23 \times 10^{-5}$ J).

The numerical results for the deflection problem are presented in Fig. 5.4. Again, we organized the different configurations from the worst one (top-left) to the best one (bottom-right). In this problem, we are interested in the average deflected energy in time and space since we intend to maximize the total energy deflected, and not to see a short-lived signal localized in space (we consequently select $S = T = 1$). The configuration without any intruders is once again the least efficient for the same reason as precedently: no energy is scattered and no signal reaches the target area (middle sections of the side walls). The full configuration, as described previously, is good at dispersing the input energy. But it does so in an isotropic manner (with the formation of a circular wave front) and is hence not optimal when one wants to focus or redirect the input energy into a specific area of the system. Our educated guess, consisting of only 20 defect particles included in the square packing, performs 1.3 times better than the full configuration as the triangular pattern is strategically placed to scatter and redirect the input energy towards the target areas. Finally, the two optimized designs provided by our numerical setup perform best: 1.8 times (resp.

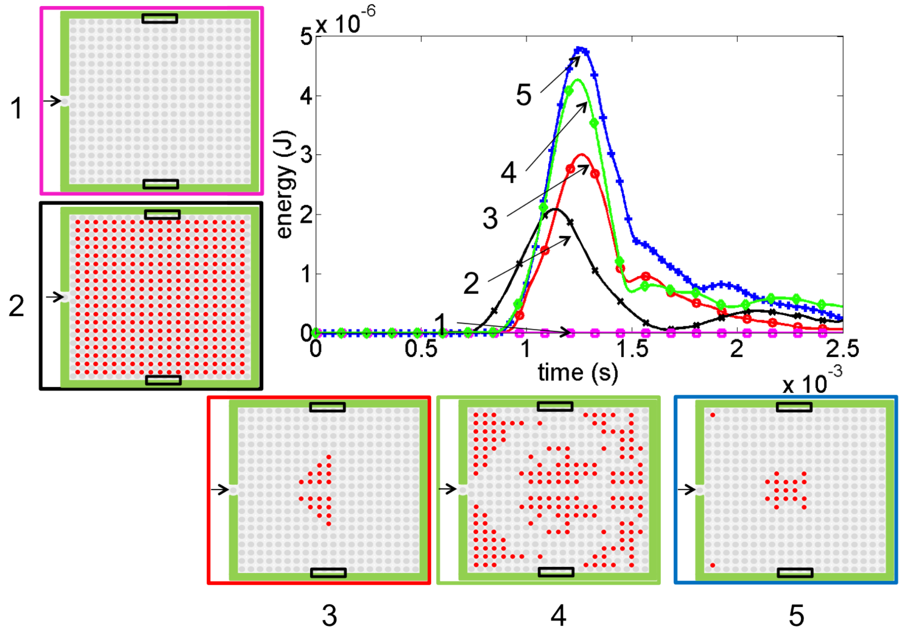

Figure 5.4: Numerical study for the focusing problem. We plot the average total energy (averaged over the number of elements in the target area) as a function of time. Each curve shows the response of a different design when impacted by a steel particle ($v_0 = 0.155$ m/s). The labeling and color of each curve corresponds to the labeling and box coloring of the various configurations around the plot. For each schematic, the gray particles compose the square packing, which is impacted from the left by an identical striker bead. The red dots are the defect particles, and the black boxes show the target area.

2.3 times) more efficient than the full design. One will note that the constrained design (blue curve, cross shaped markers) is slightly better than the unconstrained one. This is due to the fact that gradient-based methods seek local optima, and the final optimized design depends on the initial guess for all the initial volume fractions.

5.4.1.2 Other Examples: Layered Design, “3-Phase” Material Model and Combination of Cost Functions

In order to demonstrate all the available features of the numerical setup, we provide two more sample designs in this section. Fig. 5.5(a) presents an optimized design obtained when maximizing the reaction force at the top and bottom walls. A “two-phase” material model is used, in which the interstitial sites can be either empty or

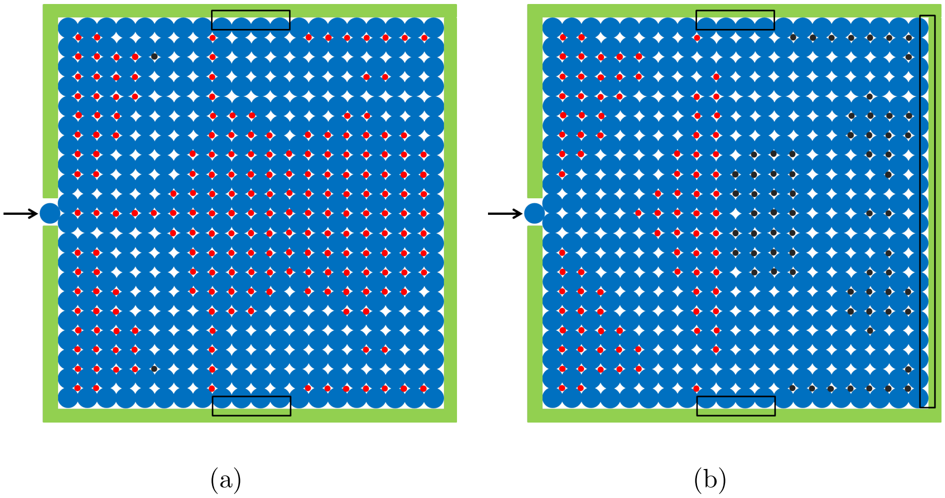

Figure 5.5: Schematic diagrams of two optimized designs obtained when 5.5(a) maximizing the reaction force at the top and bottom walls and minimizing the reaction force at the end wall, using a three-phase material in which the interstitial sites can be either empty or occupied by a steel intruder particle (red) or a brass intruder particle (black) and 5.5(b) maximizing the reaction force at the top and bottom walls, using a two-phase material model in which the interstitial sites can be either empty or occupied by a preselected material (tungsten carbide in the left half of the system and brass in the right half of the system). In both cases, a square packing of 20 × 20 steel particles (shown in blue, $R = 9.52$ mm) is impacted from the left by an identical steel striker particle. The black boxes show the target areas for each problem.

occupied by a spherical particle of a predetermined material. In this example, the left sites can potentially be occupied by steel intruders, whereas the right half can be occupied by brass intruders.

Fig. 5.5(b) presents an optimized design obtained when both maximizing the reaction force at the top and bottom walls and minimizing the reaction force at the end. A “3-phase” material model is used, in which each interstitial site can be either empty or occupied by a particle made of steel or brass. As one can see, the optimizer preferably selects the stiffest material (steel) for almost all sites where an intruder particle is placed. This is in agreement with the findings presented in chapter 3 or [121] in which it was shown that stiffer spherical interstitial defects are better at scattering energy in a square packing.

5.4.2 Material Problem

Three different problems were investigated to test the efficiency of the material optimization setup and are presented in Fig. 5.6. We study a hexagonal packing of 61 particles (radius $R = 9.52$ mm). As for the topology optimizations, a stainless steel particle of identical radius impacts the system symetrically from the left with some initial velocity v_0. Each particle in the system can take the properties of PTFE or steel or any intermediate value. However, these intermediate values are penalized through an extra term added in the objective function (see Eq. 5.6).

It was observed that material optimizations can require a number of iterations to reach convergence for which the propagation of numerical errors during the calculation of the sensitivities becomes significant, leading to non-symmetrical designs. This shortcoming was avoided by the symmetrization of the numerical setup.

In the first problem (Fig. 5.6(a)), we minimize the peak energy along the wall opposed to the impact. In the second problem (Fig. 5.6(b)), we minimize the peak energy at the center of the system. Finally, in our third sample problem (Fig. 5.6(c)), we maximize the peak energy at the back side walls. For each case, we present optimized designs obtained for different initial guesses and weight parameters w, and compare the response of the various optimized designs with the two extreme homogeneous cases (all PTFE and all steel hexagonal packings) by looking at the peak energy in the target area as a function of time.

The numerical results for the minimization of the peak energy at the end wall are presented in Fig. 5.7. The initial guess for the four designs was $\frac{1}{4}E_{steel}$ and different weight coefficients were tried (higher values for the initial guess were also investigated but results are not presented here). The weight parameter w was chosen so that the initial value of the penalty term stays between 0.5 and 15 % of the physical cost function. The weight parameters for the designs labeled 1, 2, 3 and 4 in Fig. 5.7 are equal to 2.0×10^{-14}, 1.0×10^{-13}, 3.0×10^{-13} and 5.0×10^{-13} respectively. For this particular problem, each value of w leads to a different looking solution corresponding to different local optima. Each design performs much better than the uniform cases:

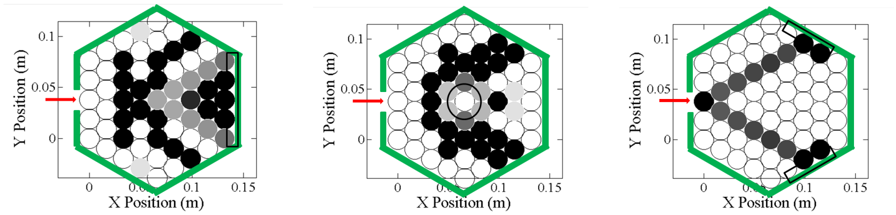

(a)

(b)

(c)

Figure 5.6: Schematic diagrams of the three material optimization problems investigated. Each consists of a 61 particle hexagonal packing (black, white and gray particles, radius $R = 9.52$ mm) impacted from the left by a stainless steel sphere (red arrow, $v_0 = 0.155$ m/s) and enclosed by a hexagonal wall (green). The black boxes represent the target areas. 5.6(a) Minimization of the peak energy at the wall opposed to the impact. 5.6(b) Minimization of the peak energy at the center particle. 5.6(c) Maximization of the peak energy at the back side walls.

the peak energy at the end wall is equal to 11.98%, 11.66%, 11.21% and 8.61% for design 1,2,3 and 4 respectively of that of the uniform steel case (15.00%, 14.60%, 14.03% and 10.79% respectively of that of the uniform PTFE case). It is interesting to note that even though the optimal cost function is roughly the same for each design, we obtain better solutions for lower values of w, which naturally correspond to designs consisting of larger gray areas. In all cases, the optimizer takes advantage of heavy/light stiff/soft interfaces to break down the incoming wave into a series of weaker signals. Similarly to what is observed in 1D systems [119], a heavy particle impacting a hexagonal system composed of light particles will create several successive wave fronts of smaller amplitudes than what is observed when impacting a hexagonal system composed of same-mass particles. This breaking down phenomenon appears every time a signal encounters a heavy/light interface. On the other hand, part of the incoming energy will be reflected at a light/heavy interface. This explains the presence of a soft PTFE area located just after the impact, followed by a group of heavy steel beads.

The same ideas are utilized in the designs presented in Fig. 5.8, when minimizing the peak energy at the center of the hexagonal packing. We once again show optimized designs obtained selecting different initial guesses and weight parameters w.

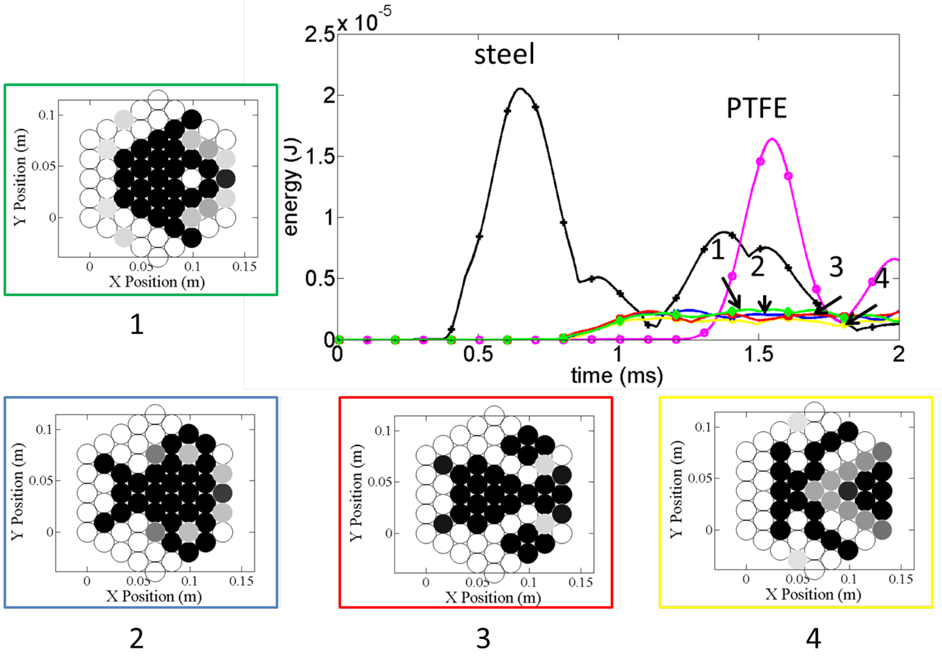

1

2

3

4

Figure 5.7: Numerical study for the first minimization problem (peak energy at the end wall). We plot the peak total energy (i.e. the maximum over the number of elements in the target area) as a function of time. Each curve shows the response of a different design when impacted by a steel particle ($v_0 = 0.155$ m/s). The labeling and color of each curve corresponds to the labeling and box coloring of the various configurations around the plot and a gray scale is used for each design in order to show the stiffness of each particle (white corresponding to PTFE and black to steel). (1) Optimized design obtained for $w = 2.0 \times 10^{-14}$ and $E_{init} = \frac{1}{4}E_{steel}$. (2) Optimized design obtained for $w = 1.0 \times 10^{-13}$ and $E_{init} = \frac{1}{4}E_{steel}$. (3) Optimized design obtained for $w = 3.0 \times 10^{-13}$ and $E_{init} = \frac{1}{4}E_{steel}$. (4) Optimized design obtained for $w = 5.0 \times 10^{-13}$ and $E_{init} = \frac{1}{4}E_{steel}$.

The designs labeled 1 and 2 were both obtained chosing $w = 1.2 \times 10^{-13}$ but with different initial design vectors: $\frac{3}{4}E_{steel}$ and $\frac{1}{4}E_{steel}$ respectively. The designs labeled 3 and 4 were obtained selecting the same initial guess as for the second design but decreasing w ($w = 5.0 \times 10^{-14}$ and $w = 2.0 \times 10^{-14}$ respectively). The efficiency of our numerical setup is evidenced again by this second sample problem: the optimal objective function values of designs 1, 2, 3, and 4 are 13.6%, 3.19%, 2.62% and 2.08% of that of the uniform steel system respectively (or 19.42%, 4.56%, 3.74% and 2.97% of that of the uniform PTFE system). We noticed that the optimizer performs better for low values of the initial design vector. However, a feature common to all the

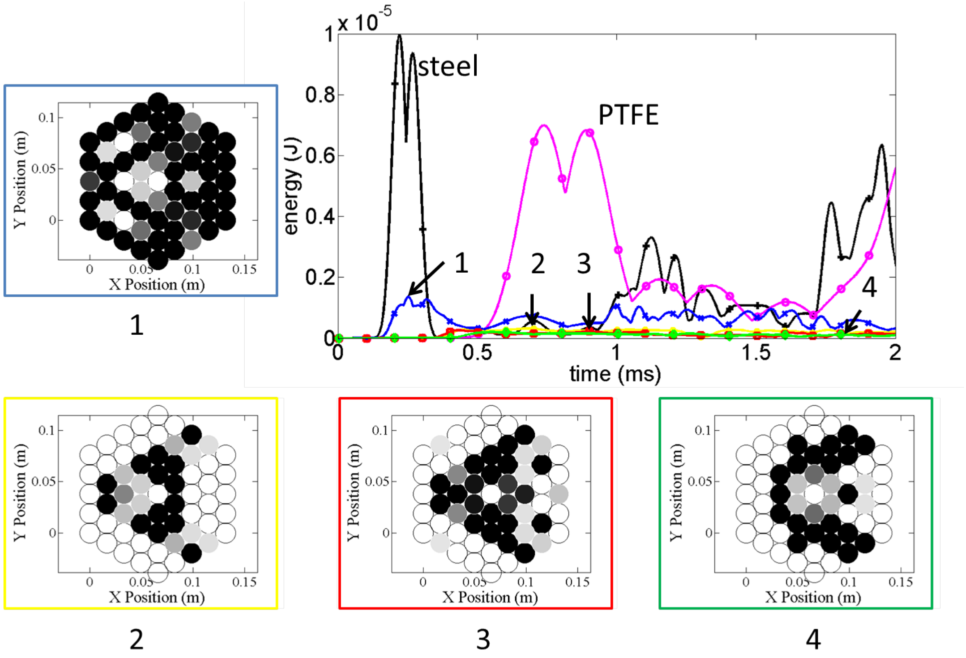

Figure 5.8: Numerical study for the second minimization problem (peak energy at the center). We plot the peak total energy (i.e. the maximum over the number of elements in the target area) as a function of time. Each curve shows the response of a different design when impacted by a steel particle ($v_0 = 0.155$ m/s). The labeling and color of each curve corresponds to the labeling and box coloring of the various configurations around the plot and a gray scale is used for each design in order to show the stiffness of each particle (white corresponding to PTFE and black to steel). (1) Optimized design obtained for $w = 1.2 \times 10^{-13}$ and $E_{init} = E_{init} = \frac{3}{4}E_{steel}$. (2) Optimized design obtained for $w = 1.2 \times 10^{-13}$ and $E_{init} = E_{init} = \frac{1}{4}E_{steel}$. (3) Optimized design obtained for $w = 5.0 \times 10^{-14}$ and $E_{init} = E_{init} = \frac{1}{4}E_{steel}$. (4) Optimized design obtained for $w = 2.0 \times 10^{-14}$ and $E_{init} = E_{init} = \frac{1}{4}E_{steel}$.

designs is the shielding of the center particle by the placement of heavier and stiffer steel particles around it, effectively reflecting the incoming wave as well as the later signals formed after reflection on the boundaries.

The numerical results for the last sample problem (maximization of the peak energy at the back side walls) are presented in Fig. 5.9. The designs labeled 1 and 2 were obtained selecting $w = 2.0 \times 10^{-14}$ for both, and different initial guesses ($\frac{1}{4}E_{steel}$ and $\frac{3}{4}E_{steel}$ respectively). Several other combinations have been investigated (not shown here) which resulted in equally efficient designs. This sample problem is simple enough that the same solution is consistently obtained. More precisely, the

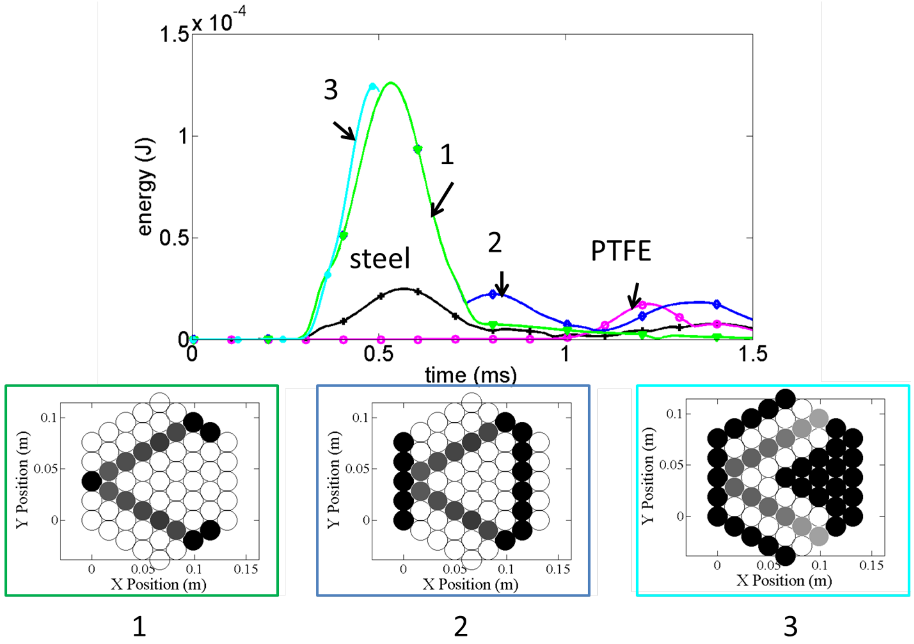

Figure 5.9: Numerical study for the maximization problem (peak energy at the center). We plot the peak total energy (i.e. the maximum over the number of elements in the target area) as a function of time. Each curve shows the response of a different design when impacted by a steel particle ($v_0 = 0.155$ m/s). The labeling and color of each curve corresponds to the labeling and box coloring of the various configurations around the plot and a gray scale is used for each design in order to show the stiffness of each particle (white corresponding to PTFE and black to steel). (1) Optimized design obtained for $w = 2.0 \times 10^{-14}$ and $E_{init} = \frac{3}{4}E_{steel}$. (2) Optimized design obtained for $w = 2.0 \times 10^{-14}$ and $E_{init} = \frac{1}{4}E_{steel}$. (3) Optimized design obtained for $w = 2.0 \times 10^{-14}$ and $E_{init} = \frac{3}{4}E_{steel}$.

optimizer always places stiff particles in the two chains originating from the impacted particle, surrounding them by PTFE particles with the exception of the last interior positions (see first design in Fig. 5.9). These locations are the only ones that affect the value of the peak energy reaching the target areas, and different initial guesses result in the placement of additional steel particles in the rest of the packing as can be seen for the last two designs if the initial value of the stiffness is closer to that of steel. This result is intuitive since these two chains offer straight paths of aligned contacts connecting the impact site to the middle of the target areas (where the amplitude is expected to be the largest) and stiffer particles will transmit a signal of larger amplitude than PTFE ones. Surrounding the two stiff chains with PTFE particles minimizes dispersion along them and maximizes the amplitude of the signal traveling through them. One could have expected to obtain a discrete design with two lines of steel (black) particles (stiffest contact). The fact that we see gray particles instead is due to the fact that we have a 2D system. To verify this hypothesis, a similar maximization problem was run for a 1D chain of particles and the obtained solution consists of steel particles only.

It is also important to note that the material chosen in the solution for the stiff particles is slightly dependent on the total time of the simulation since reflections at the boundary affect the value of the cost function. A example is provided (third design in Fig. 5.9) for which the length of the simulation was decreased in order to cancel such reflection phenomena. Interestingly, the solution provided in this case consists of two lines of stiff particles with progressively decreasing stiffnesses and densities (surrounded by lines of PTFE particles themselves surrounded by areas consisting of steel particles). However, the efficiency of the design stays almost unchanged, and all the optimized designs are 5.07 times (resp. 7.25 times) more efficient than the uniform steel case (resp. uniform PTFE case).

The next section describes the experimental setups and presents experimental reproduction of some of the optimized designs.

5.5 Experimental Results

5.5.1 Experimental Setups

A first 2D experimental setup was used to test topology optimization designs, described in section 2.1.1.1. It is presented in Fig. 2.2. We assembled a 20 by 20 square packing using $R = 9.52$ mm radius stainless steel spheres (nonmagnetic, 316 type). and custom-made tungsten carbide intruder particles were placed in some of the interstitial sites. A second setup was designed to test the material optimization designs and is described in section 2.1.1.3. It contains an hexagonal packing (five particles

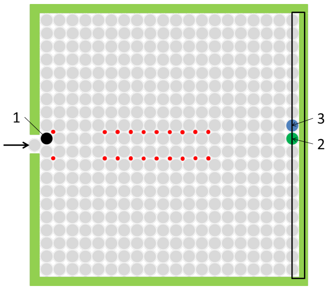

(a)

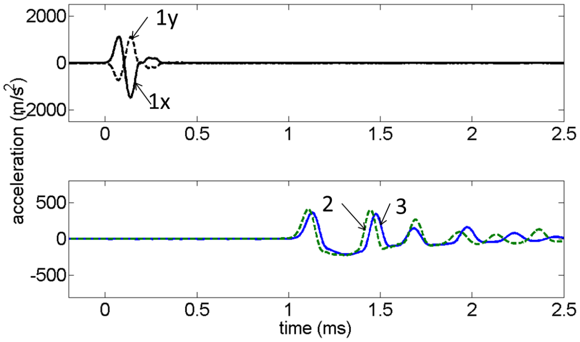

(b)

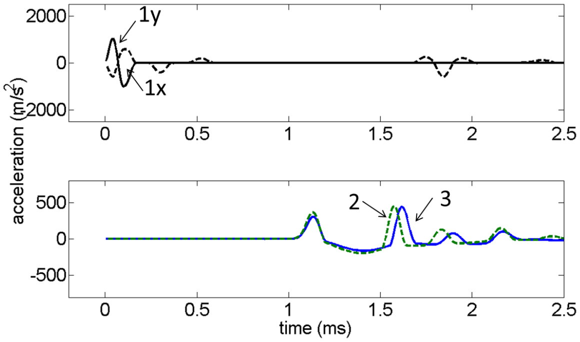

(c)

Figure 5.10: Comparison of the experimental acceleration vs time signals with the numerically obtained ones for the constrained dispersion problem 5.10(a). The system is composed of a steel square packing impacted (see black arrow) by a striker particle ($R = 9.52$ mm, $v_0 = 0.095$ m/s) with tungsten carbide interstitial intruders (red particles). 5.10(b) Experimental acceleration of the particles numbered in 5.10(a). The top panel shows the acceleration in both x and y directions for one of the two impacted particles. The bottom panel shows the acceleration in the x direction for the two particles labeled in the target area. 5.10(c) Numerical results corresponding to 5.10(b).

per side) made of PTFE and stainless steel particles with radius $R = 9.52$ mm. The material properties for the different materials used in this study are given in Table 2.1. In both cases, the system is impacted from a side by a stainless steel striker particle and its velocity is measured with an optical velocimeter. Custom-made sensor particles were used to measure local particle accelerations when perturbed by the traveling waves and compare them to their numerical counterparts. A complete description of the measurement method is provided in sections 2.1.2 and 2.1.3.

5.5.2 Comparison and Discussion

5.5.2.1 Topology Optimizations (Intruder Problem)

We experimentally investigate the optimized designs presented in Fig. 5.2. Each case being symmetrical, we only present the signals observed in one half of the systems.

In the dispersion problem (Fig. 5.10), the optimized design consists of two lines of intruders (except for the isolated ones near the impact site) and we consequently expect signals at only four elements in the target area (the four central ones). The two chains of defect particles radiate energy in the transverse direction and cause the leading pulses of the waves propagating in the two central chains of the square packing to progressively decrease. The top curves of each panel in Fig. 5.10(c) and 5.10(b) show the x and y acceleration versus time evolution for the first particle in the top central chain after impact, and serves as a time reference to compare the signals reaching the target area in the experiments and numerical simulations. The bottom panels show the x acceleration versus time for the last particles of the top two chains, out of the four where a signal is expected. We observe excellent qualitative agreement between the experiments and the numerical results, in terms of signal shape, amplitude and time of arrival.

For the deflection/focusing problem (see Fig. 5.11), the optimized design mainly consists of a mass of intruders located in the center of the square packing, that redirects part of the energy carried by the two incoming solitary waves towards the target area (centers of the side walls). The top panels in Fig. 5.11(b) and 5.11(c) show

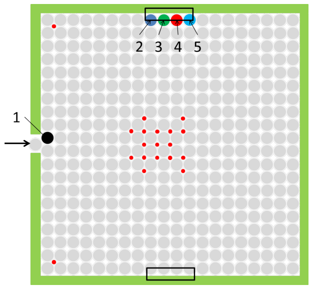

(a)

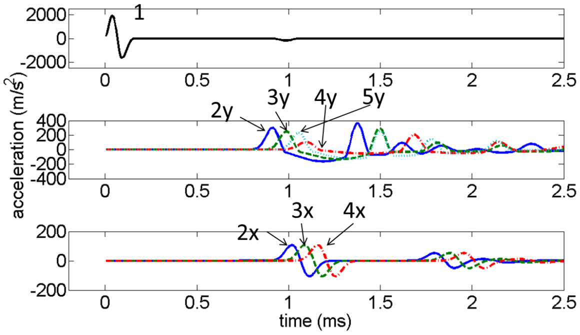

(b)

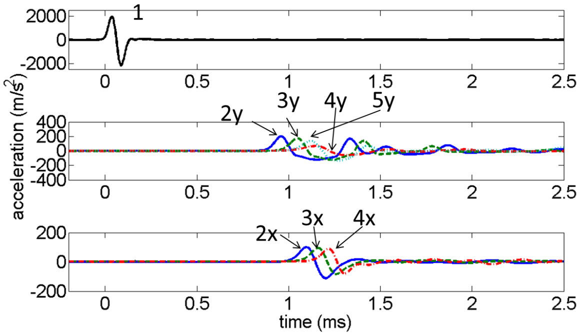

(c)

Figure 5.11: Comparison of the experimental acceleration vs time signals with the numerically obtained ones for the constrained deflection problem 5.11(a). The system is composed of a steel square packing impacted (see black arrow) by a striker particle ($R = 9.52$ mm, $v_0 = 0.155$ m/s) with tungsten carbide interstitial intruders (red particles). 5.11(c) Experimental acceleration of the particles numbered in 5.11(a). The top panel shows the acceleration in the x direction for one of the two impacted particles. The middle panel shows the y acceleration of the four particles in the top half of the target area. The bottom panel shows the acceleration in the x direction for the three first particles in that same target area. 5.10(c) Numerical results corresponding to 5.10(b).

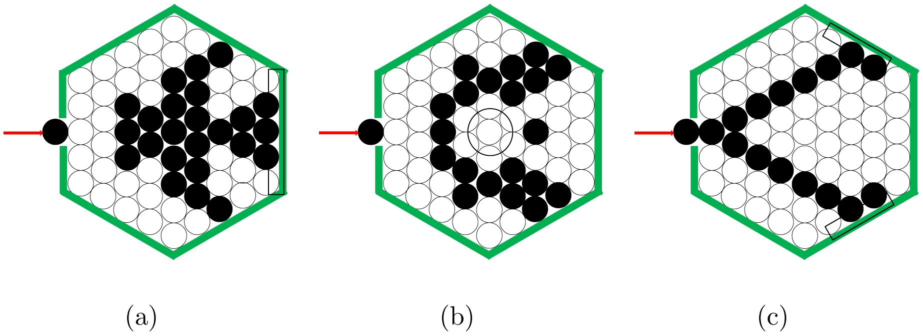

Figure 5.12: Schematic diagrams of the three systems investigated for experimental validation. Each one consists of a 61 particle hexagonal packing (steel in black and PTFE in white radius $R = 9.52$ mm) impacted from the left by a steel sphere (red arrow, $v_0 = 0.155$ m/s) and enclosed by a hexagonal wall. The black boxes represent the target areas. In 5.6(a), we minimize the peak energy that reaches the wall opposed to the impact. In 5.6(b), we minimize the peak energy at the center particle. In 5.6(c), we maximize the peak energy that reaches the two backside walls.

the acceleration in the x direction versus time for the first particle in the top central chain and as previously provides us with a time reference for the experimental runs. The bottom panels show the acceleration in the y direction for the four particles in the top half of the target area. The presence of the two intruders located in the top and bottom left corners is explained by the fact that they redirect a portion of the energy carried by the two solitary waves traveling up and down in the first transverse chain after impact into the top and bottom horizontal chains. This adds up to the energy reaching the target area after being scattered by the central group of intruders, as can be seen on the bottom panels of (b) and (c), that show the x acceleration versus time for the first three particles in the top half of the target area. We again observe excellent quantitative agreement between the numerical results and the experiments.

5.5.2.2 Material Problem

We experimentally investigate the three configurations presented in Fig. 5.12. Contrary to what was observed for the intruder optimizations, the optimized designs are not necessarily entirely discrete. As discussed previously in this chapter, this is in theory not problematic as we could find materials in nature corresponding to the

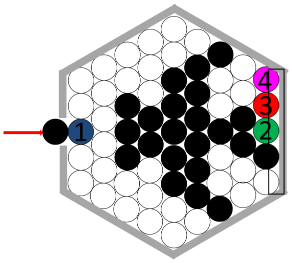

(a)

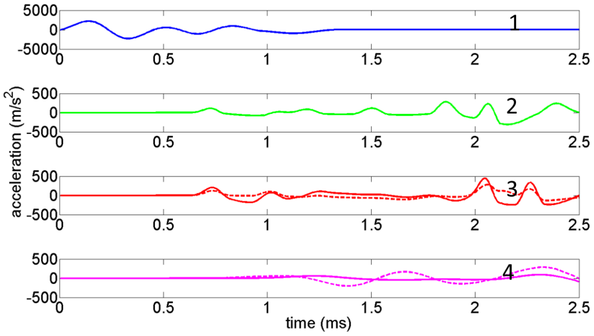

(b)

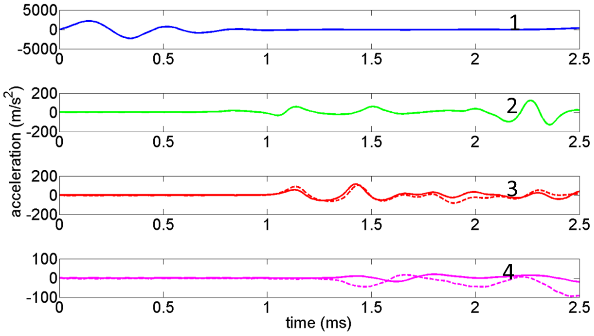

(c)

Figure 5.13: Comparison of the experimental acceleration vs time signals with the numerical ones for the first sample problem (minimization of the peak energy at the end wall) 5.13(a). The system is composed of a hexagonal packing impacted (see red arrow) by a steel striker particle ($R = 9.52$ mm, $v_0 = 0.155$ m/s). 5.13(b) Numerical accelerations of the particles labeled and colored in 5.13(a). 5.13(c) Experimental results corresponding to 5.13(b). In both 5.13(b) and 5.13(c), each panel shows the acceleration of the corresponding labeled and colored particle in 5.13(a). Solid curves correspond to x acceleration signals whereas dotted curves correspond to accelerations in the y direction. Note that when a particle is located on the axis of symmetry of the system, only the x acceleration is shown since the response of the system is symmetric.

grey areas. Nevertheless, for practical reasons, we want to test discrete designs made entirely of PTFE and steel particles. To this end, we experimentally studied discrete designs whose features are directly inspired by the non discrete optimized designs (or obtained through basic filtering) and compared the experimental outputs with the corresponding discrete numerical models. The results are shown in Figs. 5.13, 5.14 and 5.15.

For each configuration we monitored the acceleration of the impacted particle, which once again provides us with a time reference necessary to compare simulations and experiments, as well as the particles in the target areas. The symmetry argument invoked previously allows us to reduce the number of sensor locations: we present results for the signals observed at the labeled and colored particles shown in Figs. 5.13(a), 5.14(a) and 5.15(a).

We observe good quantitative agreement between the numerical simulations and the experiments. The main source of discrepancy is the presence of soft PTFE particles in the designs, which is at the origin of more dissipation than in systems composed of steel and tungsten carbide, or simply steel. This causes delays and smaller signal amplitudes in the experimental data. This is particularly visible far from the impact, where the geometric energy dilution inherent to hexagonal packings is combined with the dissipation effect. We consequently expect a better agreement for the first configuration, where all the sensors are located in the first half of the system, than for the second, where the target area is opposed to the impact. Note that for the third configuration (see Fig. 5.15) where the impact is transmitted through two linear chains of steel particles, the times of arrival and amplitudes are in excellent agreement as dissipation plays a weaker role.

5.6 Conclusion

In this chapter, we demonstrated that gradient-based optimization is an efficient tool for the design of new composite granular materials with specific wave propagation behaviors. Topology optimizations were performed and several sample problems were

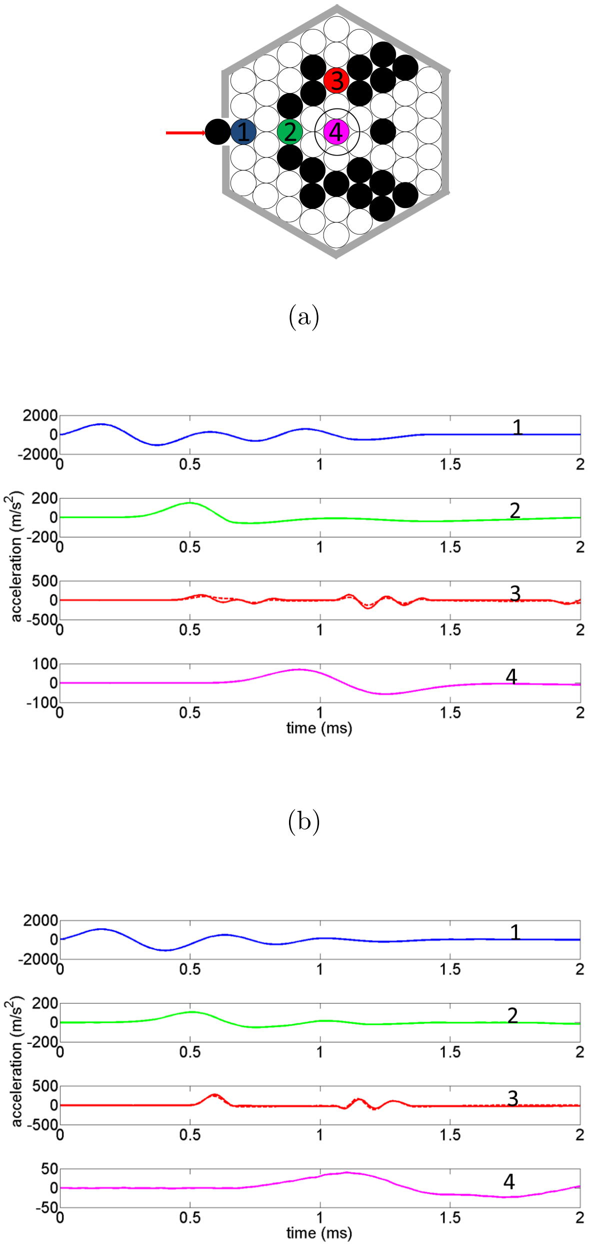

(a)

(b)

(c)

Figure 5.14: Comparison of the experimental acceleration vs time signals with the numerical ones for the second sample problem (minimization of the peak energy at the center) 5.14(a). The system is composed of a hexagonal packing impacted (see red arrow) by a steel striker particle ($R = 9.52$ mm, $v_0 = 0.155$ m/s). 5.14(b) Numerical accelerations of the particles labeled and colored in 5.14(a). 5.14(c) Experimental results corresponding to 5.14(b). In both 5.14(b) and 5.14(c), each panel shows the acceleration of the corresponding labeled and colored particle in 5.14(a). Solid curves correspond to x acceleration signals whereas dotted curves correspond to accelerations in the y direction. Note that when a particle is located on the axis of symmetry of the system, only the x acceleration is shown since the response of the system is symmetric.

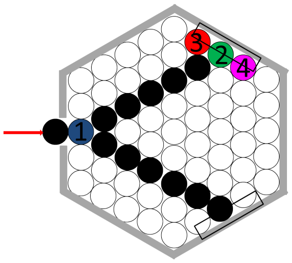

(a)

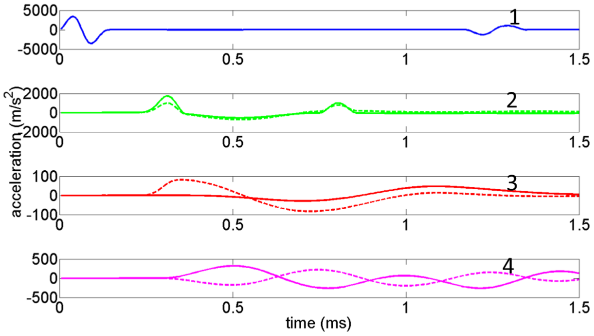

(b)

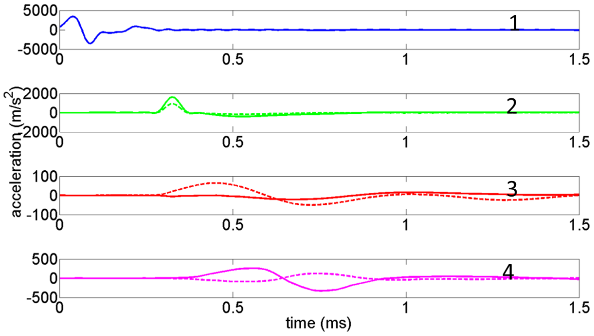

(c)

Figure 5.15: Comparison of the experimental acceleration vs time signals with the numerical ones for the second sample problem (minimization of the peak energy at the center) 5.15(a). The system is composed of a hexagonal packing impacted (see red arrow) by a steel striker particle ($R = 9.52$ mm, $v_0 = 0.155$ m/s). 5.15(b) Numerical accelerations of the particles labeled and colored in 5.15(a). 5.15(c) Experimental results corresponding to 5.15(b). In both 5.15(b) and 5.15(c), each panel shows the acceleration of the corresponding labeled and colored particle in 5.15(a). Solid curves correspond to x acceleration signals whereas dotted curves correspond to accelerations in the y direction. Note that when a particle is located on the axis of symmetry of the system, only the x acceleration is shown since the response of the system is symmetric.

studied that all evidenced the clear superiority of the numerical optimized designs over homogeneous configurations and non-optimized designs, improving their efficiency by up to a hundred times.

Several regularization techniques were implemented to guarantee the obtention of discrete designs. When using a three-phase material model, we noted that the stiffest material (TC) was almost always selected due to the better scattering properties of stiff defect particles in 2D granular crystals. When the material properties of each particle in the system can be selected from a stiff or a soft material, we observe that interfaces are advantageously placed to break down the initial impact signal into wider signals of much weaker amplitude effectively decreasing the peak amount of energy felt in any specified area.

Experimental validations were also conducted to reproduce the responses of the optimized designs. The acceleration outputs were compared and excellent agreement was observed. This is particularly important for future practical applications and the method presented in this chapter could lead to, for example, new optimized granular crystals with specific applications such as shock absorbers or waveguiding properties.

Chapter 6

Comparative Study of the Material Optimization of Granular Crystals Using a Gradient-Based Method and a Breeder Genetic Algorithm

In this chapter, we apply two optimization techniques to the design of new granular crystals with wave mitigation properties and compare their efficiency. Focusing on the particular material optimization problems of chapter 5, we compare the fitness of each design provided by a continuous gradient-based method to the ones obtained via a discrete breeder genetic algorithm. We also compare the computational time efficiency of each approach, and consistently observe that the breeder genetic algorithm yields fitter solutions at the expense of a much greater computational time.

6.1 Introduction

In this present work, we provide a comparative study of two different optimization techniques (gradient-based and non gradient-based) applied to the tailoring of the stress wave propagation in 2D granular crystals in which we seek to find the optimal distribution of material properties (material optimization) given a specific goal.

The wealth of dynamical regimes under which granular crystals can operate combined with the possibility of playing with a wide range of parameters (such as material properties, size, and geometry, for example) make the potential engineering applications of these systems numerous and great candidates for optimization and design. In chapter 5, several examples were given of granular crystal designs optimally handling the energy propagation following an impact, improving on the considerable effort that has been made in the past towards exploiting the strongly nonlinear dynamics of granular crystals to create new shock or energy absorbing devices [9–12, 59, 60, 77, 101, 140].

When conducting topology and material optimizations, a wide range of methods is available, which has been developed over the past 50 years. Evolutionary Algorithms (EAs) are non-gradient based methods first developed in the 1960s and refer to a family of probabilistic search methods inspired by the principle of natural selection [141–145]. Each parameter to optimize (volume fraction, material property in our case) corresponds to one “gene” of an “individual” (a granular crystal design in our case) whose performance is evaluated via the calculation of a fitness paramater or cost function. Breeder Genetic Algorithms (BGAs) are a specific type of EAs that use both a stochastic and deterministic selection scheme, in that the fittest “individuals” (solutions) are selected from a current generation and enter the “gene pool” to be recombined and mutated as the basis to form the new generation, fitter population, and arrive at an optimal solution [146, 147]. Non gradient-based (or heuristic) methods (see simulated annealing [148, 149], genetic algorithms [150–154], evolutionary computation [147, 155–158] among other examples) are well suited for problems where the solution space is multidimensional, multimodal, discontinuous, and noisy [159]. However, they require long computational time which may become prohibitive when studying a problem with many variables. Gradient-based topology optimization methods were introduced just over two decades ago [13, 132] for structural optimization and have since become a powerful tool commonly used in the industry. A variety of approaches exist to treat continuous problems (homogenization approach [132, 137], density approach [133, 134, 160], level-set approach [161, 162], evolutionary structural optimization approach [163] among others) and discrete final designs can be obtained through regularization techniques or post-processing, for example [133, 135, 136]. The use of first-order information about the fitness function (in addition to the fitness value) and sometimes second-order information makes the search much more efficient at the expense of the globality of the optimum reached.

In this chapter, we compare two approaches (BGA and gradient-based method), both applied in previous studies to the optimal design of granular crystals [9]. More specifically, we compare the designs and fitnesses obtained when performing material optimizations on 2D hexagonal packings. The rest of this study is organized as follows. In the next section, we describe the different optimization problems investigated. We then present the results obtained for each approach and each problem. Finally, we compare and discuss the results obtained from the two methods.

6.2 Model at Hand and Optimization Techniques

6.2.1 Numerical Modeling

The numerical model chosen to describe our granular crystals is presented in section 2.2. We numerically model our 2D granular crystals as an assembly of point masses lying in the same horizontal plane connected through nonlinear Hertzian springs, taking a finite element approach and integrate the discretized system of equations 2.3 according to a Newmark time integration scheme [107, 108].

6.2.2 Optimization Problem and Approaches

The formulation of the optimization problem is the same as in chapter 5. We perform material optimizations of 2D granular crystals and optimize the response of our system when impacted from one side by a spherical striker particle. We typically maximize or minimize the peak total energy in some area of the crystal and write the general form of the optimization problem as follows:

$$\begin{aligned} &\min_{x} f(x) \\ &\text{s.t. } x_i = x^{min} \text{ or } x^{max} \quad \forall i \in [1, ..., N] \end{aligned} \tag{6.1}$$

where x is the design vector, f is the cost (or fitness or objective) function, N is the number of design variables x_i. $f(x) = \left[\sum_{j=1}^{Nt}\left(\sum_{n=1}^{N_{step}}\left(\widehat{f}_{j,n}(x)\right)^T\right)^{S/T}\right]^{1/S}$ where $\widehat{f}_{j,n}$ represents the total energy at element j and time step n. The peak value of the objective function in time over the target area is approximated by nested p-norms with large enough values of the exponents S and T. We look for discrete designs and x_i is bound to take one of the two values x^{min} or x^{max}. Note that we do not have constraint inequalities in this study as we only consider material optimizations.

x contains the elastic moduli of each particle and $x_i = x^{min} = E_1$ corresponds to a particle made of material 1 whereas $x_i = x^{max} = E_2$ corresponds to a particle made of material 2. The rest of the material properties are then interpolated from the design vector.

6.2.2.1 Gradient-Based Method

A first approach was taken using a gradient-based continuous method (described in detail in chapter 5), which requires the relaxation of the initial problem into a non-discrete one where the design variables can take any value between the two extrema x_{min} and x_{max}. In order to start the optimization iterative process, a random configuration is selected and a first analysis is performed, followed by the evaluation of the fitness and sensitivity analysis which provides the first derivative of the cost function f with respect to the design vector x. The design vector is then updated and a new analysis and sensitivity analysis are performed. This procedure is repeated until termination criteria are met. We used the commercial nonlinear Knitro solver from Ziena Optimization LLC.

In order to obtain final discrete designs, we penalized the cost function by the addition of an artificial term (see Eq. 5.6). As one can see, discrete solutions minimize $\tilde{f}$ as the penalty term is always positive and equal to zero for fully discrete solutions. The weight parameter w needs to be tuned in order to obtain black and white designs but should not be too high in order to avoid local minima corresponding to unphysical solutions.

6.2.2.2 Breeder Genetic Algorithm

A second approach was taken using a breeder genetic algorithm (non gradient-based). Breeder genetic algorithms are more effective than other evolutionary algorithms as they use both a deterministic and a stochastic selection scheme and are well suited for discrete problems with a large search space.

A first random population (or collection of random design vectors) is evaluated and the individuals (designs) are ranked according to their fitness. Let us call λ the number of individuals in the population.

A first selection step consists of keeping the best μ individuals as the basis for the new generations. The truncation threshold $T = \frac{\mu}{\lambda}$ is usually in the 2% to 20% range and we selected $T = 0.15$ for this study, in agreement with [9]. A second step consists of creating a new generation by recombining genotypes belonging to two parents selected from the current generation. The best individual will always be conserved in the new generation. In order to create the other $\lambda - 1$ individuals of the new generation, parents are selected among the best μ individuals according to a uniform probability distribution, and recombined by means of an Extended Intermediate Recombination (EIT) scheme. Let us call $x^{Parent1}$ and $x^{Parent2}$ two such selected parents. The genotype of the offspring will be calculated as follows:

$$x_i^{Offspring} = x_i^{Parent1} + c_i \left(x_i^{Parent2} - x_i^{Parent1} \right), \forall i \in [1, .., N], \tag{6.2}$$

where c_i is a scaling factor uniformly chosen in the interval $[-d, 1+d]$. The selection of $d = 0.25$ is a good choice which allows the obtaining of new solutions located both within and outside the continuous interval defined by the two parents, exploring the search space more efffectively. Finally, a last step consists of mutating the offspring variables by the addition of small random values with low probability (inversely proportional to the number of parameters to optimize). Analyses are then performed for the new population which in turn is selected, recombined and mutated to obtain a fitter population. More detail on this method can be found in [19].

The next section describes the various optimization problems considered and presents the results obtained via each approach.

6.3 Optimized Designs and Dynamic Responses

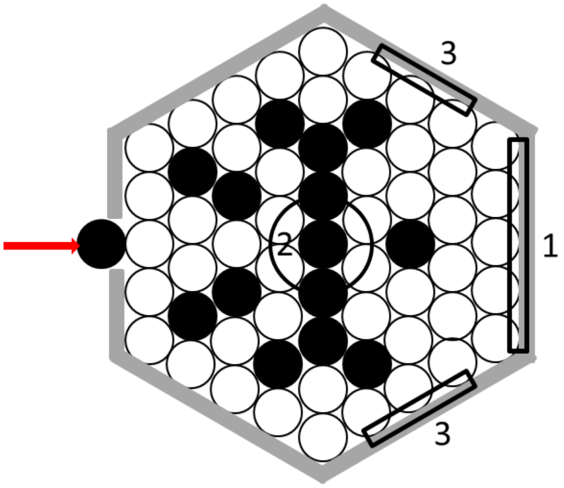

Figure 6.1: Schematic diagram of the various optimization problems considered in our study. Material optimizations of hexagonal packings impacted by a steel particle (arrow). Steel particles are represented in black, PTFE particles in white and the boxes show the locations of the target area for each case: (1) minimization of the total energy at the end, (2) minimization of the total energy at the center and (3) maximization of the total energy at the sides.

Three different problems were investigated to compare the efficiency of the two approaches. They are presented in Fig. 6.1.

We studied a hexagonal packing composed of 61 particles. Each particle in the system can be made of stainless steel or PTFE (material optimization) and the system is impacted from the left by a steel striker particle. We seek the optimal distribution of steel and PTFE beads such that:

1. we minimize the peak total energy at the end wall (target area labeled “1” in Fig. 6.1),

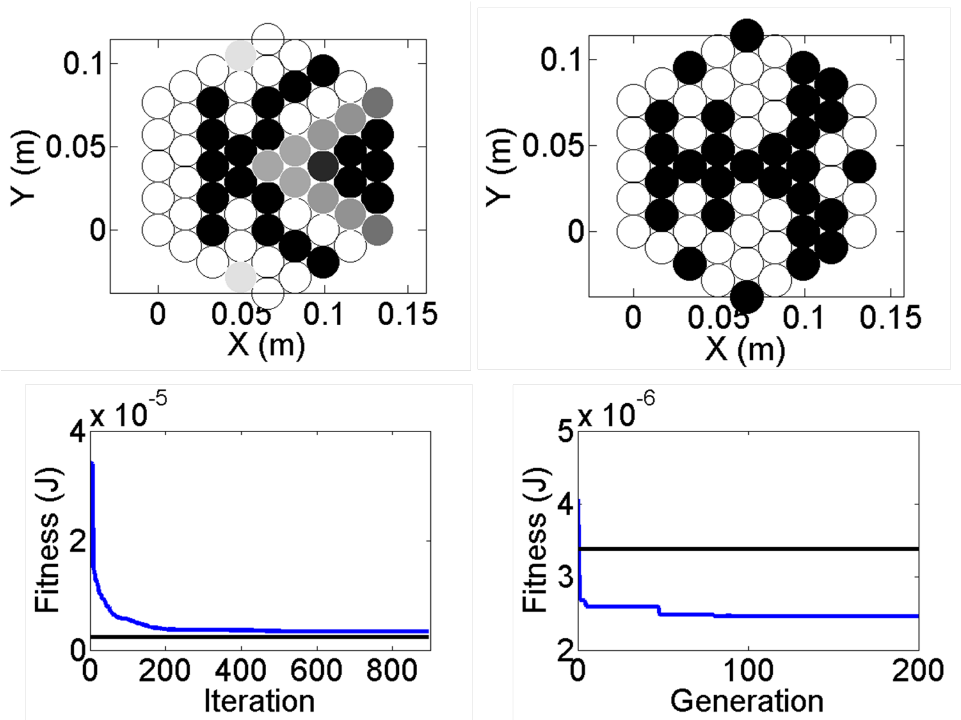

Figure 6.2: Comparison of the designs (top) and evolution of the fitness (bottom) obtained using the penalized gradient-based method (left) and the breeder genetic algorithm (right) when minimizing the energy at the end opposed to the impact ($v_{striker} = 0.155$ m/s). In each design, the black particles are made of steel and the white particles are made of PTFE. Note that the GA design is discrete whereas some grey areas can be found in the solution obtained using the gradient-based method. In each bottom plot, the black horizontal line shows the converged value of the fitness obtained using the other approach.

2. we minimize the peak total energy at the center (target area labeled “2” in Fig. 6.1), and

3. we maximize the peak total energy at the side walls (target area labeled “3” in Fig. 6.1).

The numerical setup was symmetrized in order to force the acquisition of meaningful designs since both the loading and boundary conditions are symmetric. This is particularly important when using the genetic algorithm approach as the stochastic processes involved in the creation of the new generations would lead to the formation of highly asymetric and hence unphysical solutions. We consequently have 33 design variables when running optimizations of hexagonal packings composed of 61 particles.

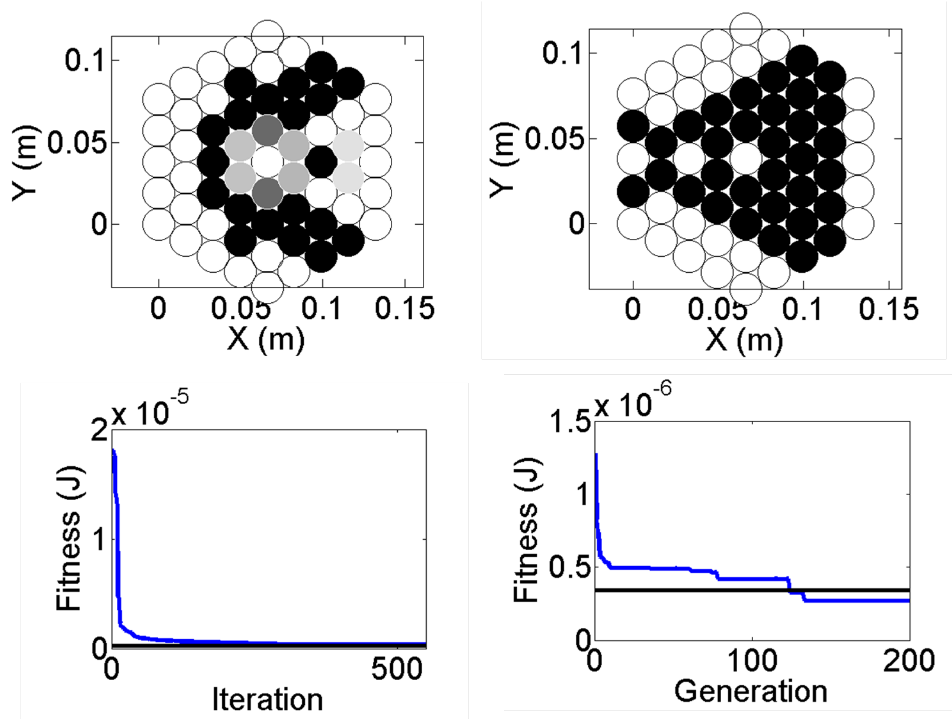

Figure 6.3: Comparison of the designs (top) and evolution of the fitness (bottom) obtained using the penalized gradient-based method (left) and the breeder genetic algorithm (right) when minimizing the energy at the center ($v_{striker} = 0.155$ m/s). In each design, the black particles are made of steel and the white particles are made of PTFE. Note that the GA design is discrete whereas some grey areas can be found in the solution obtained using the gradient-based method. In each bottom plot, the black horizontal line shows the converged value of the fitness obtained using the other approach.

When taking the evolutionary approach, the number of individuals contained in each population should be of the order of the number of genes or design variables of our problem. We selected $N_{population} = 50$.

The optimized designs as well as the plots showing the evolution of the fitness with the number of iterations (or generations when using the BGA approach) are presented in Figs. 6.2, 6.3 and 6.4.

6.3.1 Interpretation of the Optimized Designs

Although the two methods employed in this study are fundamentally different, we observe similar features in the solutions provided by each. For the two minimization

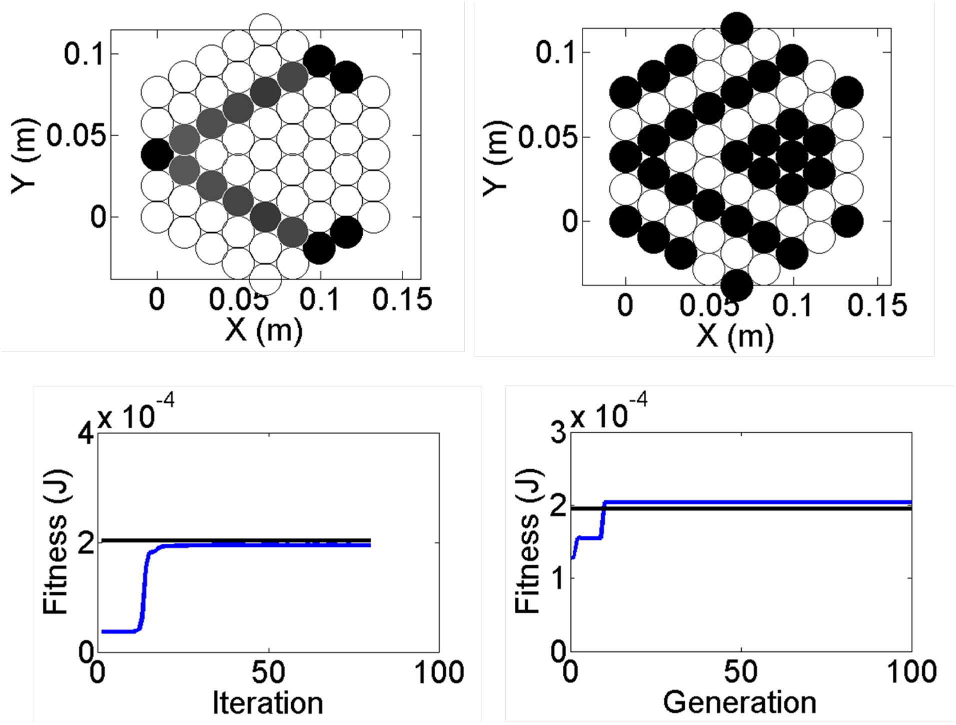

Figure 6.4: Comparison of the designs (top) and evolution of the fitness (bottom) obtained using the penalized gradient-based method (left) and the breeder genetic algorithm (right) when maximizing the energy at the sides ($v_{striker} = 0.155$ m/s). In each design, the black particles are made of steel and the white particles are made of PTFE. Note that the GA design is discrete whereas some grey areas can be found in the solution obtained using the gradient-based method. In each bottom plot, the black horizontal line shows the converged value of the fitness obtained using the other approach.

problems (see Figs 6.2 and 6.3) the particle impacted (and sometimes a patch of particles near the impact site) is made of PTFE. This is consistent with several previous studies that described how an impulse is broken down when reaching a light mass defect or a heavy/light interface (see [17, 119] for example). Several light/heavy/light interfaces are then placed between the impact location and the target area, adequately surrounding it. When maximizing the energy at the sides (see Fig. 6.4), both solutions are extremely similar and place two lines of steel particles directly connecting the impact site with the centers of the target areas, where the energy is expected to be maximal. These two lines are surrounded by soft PTFE particles, which minimizes the dispersion as the signals propagate down the stiff chains. In the solution generated via the breeder genetic algorithm, these neighboring PTFE chains are themselves surrounded by steel particles, which maximizes the energy reflected back towards the target areas (although this effect is small). The designs obtained for this specific problem are expected to be close to the global maximum.

In the next section, we compare the performance of each approach for each sample problem in terms of fitness and computational time.

6.4 Comparison and Discussion

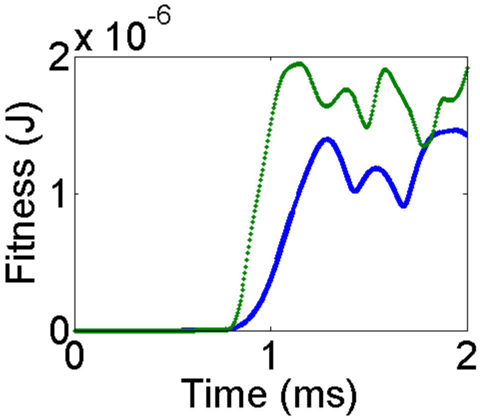

Figure 6.5: Evolution of the peak energy over the target area (approximated by the p-norm of the total energy) as a function of time for the material optimization problem consisting of minimizing the peak total energy at the end wall. The solid blue curve shows the response of the solution obtained via the BGA approach and the dotted green curve shows the response of the solution obtained via the gradient-based approach.

6.4.1 Performance

We present the dynamic responses of each solution in Fig. 6.5, 6.6 and 6.7. In order to measure the performance of each solution, we calculate the total energy at each location in the target area for each time step. Each figure shows the peak total energy in space as a function of time. The various fitnesses are also summarized in Table 6.4.1. As one can see, the genetic algorithm approach provides better solutions for every problem. This is expected as this method uses a global search strategy and

Approach	Material: min end	Material: min center	Material: max side
Genetic algorithm	2.47×10^{-6}	2.73×10^{-7}	2.03×10^{-4}
Gradient-based method	3.39×10^{-6}	3.43×10^{-7}	1.95×10^{-4}

Table 6.1: Comparison of the performance of the two approaches for each optimization problem.

is better at exploring the design space than the gradient-based approach that instead converges towards a local optimum located near the initial guess. In order to verify that the BGA approach indeed provides a global optimum, simulations were run using different initial populations, and we observed convergence to the same design solution. Depending on the problem, we estimate the BGA approach to be between 5% and 30% more efficient in terms of fitness. This seems to indicate that most of the local optima of the design space have performances similar to the global solution.

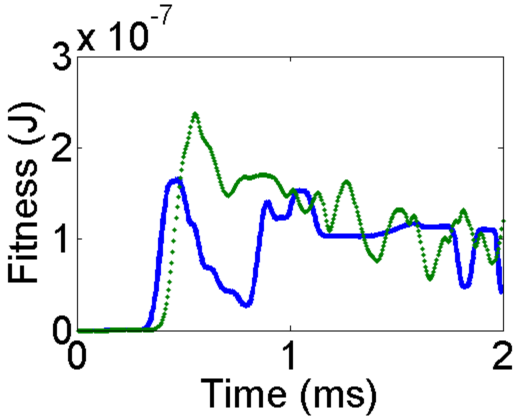

Figure 6.6: Evolution of the peak energy over the target area (approximated by the p-norm of the total energy) as a function of time for the material optimization problem consisting in minimizing the peak total energy at the center. The solid blue curve shows the response of the solution obtained via the BGA approach and the dotted green curve shows the response of the solution obtained via the gradient-based approach.

6.4.2 Computational Time

In order to accurately compare the computational times taken by each approach, the same numerical setup was used to evaluate the fitness of each design. If we denote by T the time taken to perform one transient analysis (or fitness evaluation), $N_{population}$

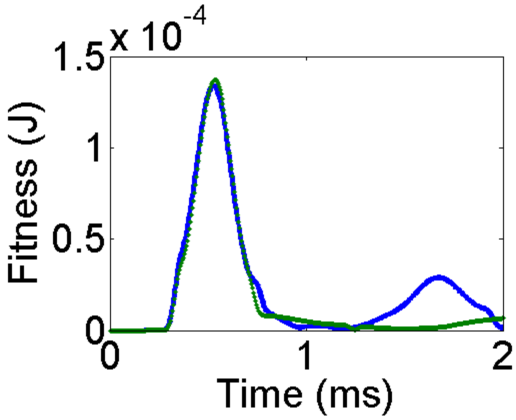

Figure 6.7: Evolution of the peak energy over the target area (approximated by the p-norm of the total energy) as a function of time for the material optimization problem consisting in maximizing the peak total energy at the side walls. The solid blue curve shows the response of the solution obtained via the BGA approach and the dotted green curve shows the response of the solution obtained via the gradient-based approach.

Approach	Material: min end	Material: min center	Material: max side
Genetic algorithm	10000 T	10000 T	5000 T
Gradient-based method	1000 T	750 T	100 T

Table 6.2: Comparison of the approximated computational times of the two approaches for each optimization problem.

the number of individuals in each generation and $N_{generation}$ the number of generations required, the total computational time of the BGA approach is approximately equal to $N_{population} \times N_{generation} \times T$. No optimality criterion is available with this method and we choose the maximum number of generations to be 200 (but less is sometimes required). $N_{population}$ is of the order of the number of design variables N. This is to be compared to the number of transient and sensitivity analyses performed when taking the gradient-based approach $N_{iteration} \times (1 + \epsilon M)T$, with M being the number of design variables and constraints and ϵ typically equal to 0.004 in our study. The number of design variables N is equal to 33 for the material optimization problems we consider. The computational times are compared in Table 6.4.1. In every case, the computational time is considerably larger when using the BGA (between 10 and 50 times larger).

6.5 Summary

In this chapter, we compared the optimized designs obtained when applying two conceptually different optimization methods to the design of granular crystals: a continuous gradient-based method that makes use of a sensitivity analysis to seek local optima and a discrete breeder genetic algorithm that searches for the global optimum using evolution and breeding principles and only requires fitness evaluations. We specifically looked at the performance and computational time for various test problems and consistently observed that the BGA yields better solutions at the expense of a much greater computational time. Despite the apparent suitedness of evolutionary methods for our discrete systems, we conclude that a gradient-based approach is preferable, all the more so when the number of controls of the problem reaches "large" values.

Chapter 7

Conclusion

This thesis described several new ways to control and tailor the mechanical energy associated with the propagation of stress waves in granular crystals through the use of heterogeneities (interstitial defect particles and material heterogeneities) in otherwise perfectly ordered systems. We primarily focus on square packed 2D granular crystals with interstitial spherical intruders and composite hexagonal packings. The potential applications of this work include novel shock and vibration absorber devices, delay lines, or wave guides.

In chapter 3, we used numerical simulations and experiments to investigate the interaction of a highly nonlinear solitary wave with spherical intruders in 2D uncompressed square packings. It was demonstrated that a defect particle scatters the impact energy and redistributes it in the various chains in contact with the intruder. The amount of energy dispersed is strongly related to the elastic modulus of the intruder, stiffer defects having a better scattering power, whereas other parameters such as the mass of the defect or the impact velocity have a much smaller effect on the impulse redirection. It was evidenced that several regimes occur depending on the stiffness of the intruder and a localization phenomenon was observed at the site were a soft defect is placed. The setting of two defects was also analyzed and we found that the redirection efficiency of the system is greatly enhanced when placing multiple defects in a line.

The study presented in chapter 4 demonstrated with simulations and experiments the mechanism of solitary wave equipartition in a strongly nonlinear crystal in which two chains are coupled by a line of light and stiff defects. The intially localized impulse is progressively transfered from one chain to the adjacent one over a short spatial distance (slighty larger than the distance needed for the stabilization of a solitary wave). The transfer of energy stops when the amplitude of the two waves traveling in each chain are equal, after which the defects are responsible for low radial leaks in the direction transverse to the direction of propagation. A simplified 1.5D analytical model was developed which captures well the principal features of this phenomenon.

In chapter 5, we described the first use of gradient-based optimization techniques applied to the design of engineered crystals with specific wave propagation behaviors. A new numerical setup was developed that includes several material-phase models and regularization methods in order to obtain practically feasible (discrete) solutions. Topology and material optimizations were performed and several sample problems were studied. In all cases, we demonstrated the clear superiority of our designs when compared to the homogeneous and other non-optimal benchmark configurations. Experimental validations were conducted and we were able to reproduce the responses of the numerical designs with excellent agreement.

Finally, in chapter 6 we provided a comparison of two conceptually different optimization methods. A breeder genetic algorithm was applied to the design of hexagonal packings in which we optimized the material distribution, and compared the efficiency of the solutions in terms of cost function and computational time, a posteriori justifying the approach taken in chapter 5.

The findings and methods presented in this research can be used as the starting point for the study and design of more complicated granular crystals (increasing the number of controls in the optimization for instance, but also looking at different impact conditions, combining material and topology optimization etc.) in more realistic applications and could potentially be applied to other discrete nonlinear systems. Another interesting and relevant continuation of this work would consist of studying the effect of different kinds of defect particles, including conformal matrix, which in addition to having tunable dispersion properties similar to spherical defect particles would bring integrity to the structure. It would also be of interest to further study 2D granular crystals in the linear and weakly nonlinear regimes, extending the ongoing research focusing on the phenomena taking place in linearized or weakly nonlinear 1D crystals.

Bibliography

[1] D.-M.Wang and Z.-W. Wang, “Experimental investigation into the cushioning properties of honeycomb paperboard,” *Packaging Technology and Science*, vol. 21, no. 6, pp. 309–316, 2008.

[2] C. Harris, *Shock and Vibration Handbook, Third Edition.* New York, NY: McGraw-Hill, 1988.

[3] V. F. Nesterenko, *Dynamics of Hetereogeneous Materials.* New York, NY: Springer, 2001.

[4] H. M. Jaeger, S. R. Nagel, and R. P. Behringer, “Granular solids, liquids, and gases,” *Rev. Mod. Phys.*, vol. 68, pp. 1259–1273, 1996.

[5] M. Faraday, “On a peculiar class of acoustical figures; and on certain forms assumed by groups of particles upon vibrating elastic surfaces,” *Philosophical Transactions of the Royal Society of London*, vol. 121, pp. 299–340, 1831.

[6] O. Reynolds, “Lvii. on the dilatancy of media composed of rigid particles in contact.,” *London, Edinburgh and Dublin Philosophical Magazine and Journal of Science*, vol. 20, p. 469, 1885.

[7] V. F. Nesterenko, “Propagation of nonlinear compression pulses in granular media,” *J. Appl. Mech. Tech. Phys.*, vol. 24, pp. 733–743, 1983.

[8] V. F. Nesterenko, C. Daraio, E. B. Herbold, and S. Jin, “Anomalous wave reflection at the interface of two strongly nonlinear granular media,” *Phys. Rev. Lett.*, vol. 95, p. 158702, 2005.

[9] F. Fraternali, M. Porter, and C. Daraio, “Optimal design of composite granular protectors,” *Mech. Adv. Mater. Struct.*, vol. 17, pp. 1–19, 2010.

[10] R. L. Doney and S. Sen, “Impulse absorption by tapered horizontal alignments of elastic spheres,” *Phys. Rev. E*, vol. 72, p. 041304, 2005.

[11] C. Daraio, V. F. Nesterenko, E. B. Herbold, and S. Jin, “Energy trapping and shock disintegration in a composite granular medium,” *Phys. Rev. Lett.*, vol. 96, p. 058002, 2006.

[12] J. Hong, “Universal power-law decay of the impulse energy in granular protectors,” *Phys. Rev. Lett.*, vol. 94, p. 108001, 2005.

[13] M. Bendsøe and O. Sigmund, *Topology optimization: theory, methods and applications*. Berlin: Springer-Verlag, 2004.

[14] P. W. Anderson, “Absence of diffusion in certain random lattices,” *Phys. Rev.*, vol. 109, pp. 1492–1505, 1958.

[15] S. Job, F. Santibanez, F. Tapia, and F. Melo, “Wave localization in strongly nonlinear Hertzian chains with mass defect,” *Phys. Rev. E*, vol. 80, p. 025602, 2009.

[16] L. Ponson, N. Boechler, Y. M. Lai, M. A. Porter, P. G. Kevrekidis, and C. Daraio, “Nonlinear waves in disordered diatomic granular chains,” *Phys. Rev. E*, vol. 82, p. 021301, 2010.

[17] E. Hascoët and H. Herrmann, “Shocks in non-loaded bead chains with impurities,” *The European Physical Journal B - Condensed Matter and Complex Systems*, vol. 14, pp. 183–190, 2000.

[18] G. Theocharis, M. Kavousanakis, P. G. Kevrekidis, C. Daraio, M. A. Porter, and I. G. Kevrekidis, “Localized breathing modes in granular crystals with defects,” *Phys. Rev. E*, vol. 80, p. 066601, 2009.

[19] F. Fraternali, A. Marino, T. E. Sayed, and A. D. Cioppa, “On the structural shape optimization through variational methods and evolutionary algorithms,” *Mechanics of Advanced Materials and Structures*, vol. 18, no. 4, pp. 225–243, 2011.

[20] O. Sigmund, “On the usefulness of non-gradient approaches in topology optimization,” *Struct. Multidiscip. Optim.*, vol. 43, no. 5, pp. 589–596, 2011.

[21] P. G. Kevrekidis, “Non-linear waves in lattices: Past, present, future,” *IMA Journal of Applied Mathematics*, no. 1-35, 2011.

[22] L. D. Landau and E. M. Lifshitz, *Theory of Elasticity.* Oxford-Boston: Butterworth-Heinemann, 1995.

[23] H. Hertz, “On the contact of elastic solids,” *J. Reine und Anges. Math.*, vol. 92, pp. 156–171, 1881.

[24] K. Johnson, *Contact Mechanics.* Cambridge University Press, 1987.

[25] W. Goldsmith, *Impact: The Theory and Physical Behaviour of Colliding Solids.* Dover Civil and Mechanical Engineering Series, Dover Publications, Incorporated, 2001.

[26] C. Coste and B. Gilles, “On the validity of Hertz contact law for granular material acoustics,” *The European Physical Journal B - Condensed Matter and Complex Systems*, vol. 7, no. 1, pp. 155–168, 1999.

[27] C. Coste, E. Falcon, and S. Fauve, “Solitary waves in a chain of beads under Hertz contact,” *Phys. Rev. E*, vol. 56, pp. 6104–6117, 1997.

[28] A. Molinari and C. Daraio, “Stationary shocks in periodic highly nonlinear granular chains,” *Phys. Rev. E*, vol. 80, p. 056602, 2009.

[29] N. Boechler, G. Theocharis, S. Job, P. Kevrekidis, M. Porter, and C. Daraio, “Discrete breathers in one-dimensional diatomic granular crystals,” *Phys. Rev. Lett.*, vol. 104, no. 24, p. 244302, 2010.

[30] G. Theocharis, N. Boechler, P. G. Kevrekidis, S. Job, M. A. Porter, and C. Daraio, "Intrinsic energy localization through discrete gap breathers in one-dimensional diatomic granular crystals," *Phys. Rev. E*, vol. 82, p. 056604, 2010.

[31] D. J. Korteweg and G. de Vries, "On the change of form of long waves advancing in a rectangular canal, and on new type of long stationary waves," *London, Edinburgh and Dublin Philosophical Magazine and Journal of Science*, vol. 39, pp. 422–443, 1895.

[32] J. S. Russel, "Report on waves," *Report of the 14th Meeting of the British Association for the Advancement of Science*, pp. 311–390, 1844.

[33] E. B. Herbold, J. Kim, V. Nesterenko, S. Wang, and C. Daraio, "Pulse propagation in a linear and nonlinear diatomic periodic chain: effects of acoustic frequency band-gap," *Acta Mechanica*, vol. 205, no. 85, 2009.

[34] S. Sen, J. Hong, J. Bang, E. Avalos, and R. Doney, "Solitary waves in the granular chain," *Physics Reports*, vol. 462, no. 2, pp. 21 – 66, 2008.

[35] C. Daraio, V. F. Nesterenko, E. B. Herbold, and S. Jin, "Tunability of solitary wave properties in one-dimensional strongly nonlinear phononic crystals," *Phys. Rev. E*, vol. 73, p. 026610, 2006.

[36] A. N. Lazaridi and V. F. Nesterenko, "Observation of a new type of solitary waves in a one-dimensional granular medium," *J. Appl. Mech. Tech. Phys.*, vol. 26, pp. 405–408, 1985.

[37] M. A. Porter, C. Daraio, E. B. Herbold, I. Szelengowicz, and P. G. Kevrekidis, "Highly nonlinear solitary waves in periodic dimer granular chains," *Phys. Rev. E*, vol. 77, no. 015601(R), 2008.

[38] M. A. Porter, C. Daraio, I. Szelengowicz, E. B. Herbold, and P. G. Kevrekidis, "Highly nonlinear solitary waves in heterogeneous periodic granular media," *Physica D*, vol. 238, no. 666, 2009.

[39] R. MacKay, "Solitary waves in a chain of beads under Hertz contact," *Physics Letters A*, vol. 251, no. 3, pp. 191 – 192, 1999.

[40] G. Friesecke and J. Wattis, "Existence theorem for solitary waves on lattices," *Commun. Math. Phys.*, vol. 161, no. 391, 1994.

[41] J.-Y. Ji and J. Hong, "Existence criterion of solitary waves in a chain of grains," *Physics Letters A*, vol. 260, no. 12, pp. 60 – 61, 1999.

[42] A. Chatterjee, "Asymptotic solution for solitary waves in a chain of elastic spheres," *Phys. Rev. E*, vol. 59, pp. 5912–5919, 1999.

[43] S. Sen and M. Manciu, "Solitary wave dynamics in generalized Hertz chains: An improved solution of the equation of motion," *Phys. Rev. E*, vol. 64, p. 056605, 2001.

[44] C.-H. Liu and S. R. Nagel, "Sound in sand," *Phys. Rev. Lett.*, vol. 68, pp. 2301–2304, 1992.

[45] C.-H. Liu and S. R. Nagel, "Sound in a granular material: Disorder and nonlinearity," *Phys. Rev. B*, vol. 48, pp. 15646–15650, 1993.

[46] J. D. Goddard, "Nonlinear elasticity and pressure-dependent wave speeds in granular media," *Proc. R. Soc. Lond. A*, vol. 430, pp. 105–131, 1990.

[47] P. G. de Gennes *Europhys. Lett.*, vol. 35, p. 145, 1996.

[48] P. G. de Gennes *"Lectures of the College de France held at "Ecole Centrale de Lyon"*, 1997.

[49] R. S. Sinkovits and S. Sen, "Nonlinear dynamics in granular columns," *Phys. Rev. Lett.*, vol. 74, pp. 2686–2689, 1995.

[50] S. Sen and R. S. Sinkovits, "Sound propagation in impure granular columns," *Phys. Rev. E*, vol. 54, pp. 6857–6865, 1996.

[51] M. Manciu, S. Sen, and A. J. Hurd, “Crossing of identical solitary waves in a chain of elastic beads,” *Phys. Rev. E*, vol. 63, p. 016614, 2000.

[52] M. Manciu, S. Sen, and A. J. Hurd, “The propagation and backscattering of soliton-like pulses in a chain of quartz beads and related problems. (i). propagation,” *Physica A: Statistical Mechanics and its Applications*, vol. 274, no. 3-4, pp. 588 – 606, 1999.

[53] M. Manciu, S. Sen, and A. J. Hurd, “The propagation and backscattering of soliton-like pulses in a chain of quartz beads and related problems. (ii). backscattering,” *Physica A: Statistical Mechanics and its Applications*, vol. 274, no. 3-4, pp. 607 – 618, 1999.

[54] S. Sen, M. Manciu, and J. D. Wright, “Solitonlike pulses in perturbed and driven Hertzian chains and their possible applications in detecting buried impurities,” *Phys. Rev. E*, vol. 57, pp. 2386–2397, 1998.

[55] S. Sen, M. Manciu, R. S. Sinkovits, and A. J. Hurd, “Nonlinear acoustics in granular assemblies,” *Granular Matter*, vol. 3, pp. 33–39, 2001.

[56] S. Sen, F. S. Manciu, and M. Manciu, “Thermalizing an impulse,” *Physica A: Statistical Mechanics and its Applications*, vol. 299, no. 3-4, pp. 551 – 558, 2001.

[57] D. T. Wu, “Conservation principles in solitary impulse propagation through granular chains,” *Physica A: Statistical Mechanics and its Applications*, vol. 315, no. 1-2, pp. 194 – 202, 2002.

[58] M. Nakagawa, J. H. Agui, D. T. Wu, and D. V. Extramiana, “Impulse dispersion in a tapered granular chain,” *Granular Matter*, vol. 4, pp. 167–174, 2003.

[59] R. Doney and S. Sen, “Decorated, tapered, and highly nonlinear granular chain,” *Phys. Rev. Lett.*, vol. 97, p. 155502, 2006.

[60] F. Melo, S. Job, F. Santibanez, and F. Tapia, “Experimental evidence of shock mitigation in a Hertzian tapered chain,” *Phys. Rev. E*, vol. 73, p. 041305, 2006.

[61] K. Lindenberg, U. Harbola, A. Romero, and A. Rosas, “Pulse propagation in granular chains,” vol. 1339, pp. 97–110, 2010.

[62] J. Hong, J.-Y. Ji, and H. Kim, “Power laws in nonlinear granular chain under gravity,” *Phys. Rev. Lett.*, vol. 82, pp. 3058–3061, 1999.

[63] J. Hong and A. Xu, “Nondestructive identification of impurities in granular medium,” *Applied Physics Letters*, vol. 81, no. 25, pp. 4868 –4870, 2002.

[64] S. Job, F. Melo, A. Sokolow, and S. Sen, “How Hertzian solitary waves interact with boundaries in a 1d granular medium,” *Phys. Rev. Lett.*, vol. 94, p. 178002, 2005.

[65] S. Job, F. Melo, F. Santibanez, and F. Tapia, “Nonlinear waves in Hertzian granular chains: Effects of inertial and stiffness heterogeneities,” 2007.

[66] A. Rosas and K. Lindenberg, “Pulse dynamics in a chain of granules with friction,” *Phys. Rev. E*, vol. 68, no. 041304, 2003.

[67] A. Rosas, A. Romero, V. F. Nesterenko, and K. Lindenberg, “Observation of two-wave structure in strongly nonlinear dissipative granular chains,” *Phys. Rev. Lett.*, vol. 98, no. 164301, 2007.

[68] A. Rosas and K. Lindenberg, “Pulse velocity in a granular chain,” *Phys. Rev. E*, vol. 69, no. 037601, 2004.

[69] U. Harbola, A. Rosas, M. Esposito, and K. Lindenberg, “Pulse propagation in tapered granular chains: An analytic study,” *Phys. Rev. E*, vol. 80, no. 031303, 2009.

[70] U. Harbola, A. Rosas, A. H. Romero, and K. Lindenberg, “Pulse propagation in randomly decorated chains,” *Phys. Rev. E*, vol. 82, no. 011306, 2010.

[71] Y. Starosvetsky and A. F. Vakakis, “Traveling waves and localized modes in one-dimensional homogeneous granular chains with no precompression,” *Phys. Rev. E*, vol. 82, p. 026603, 2010.

[72] K. R. Jayaprakash, Y. Starosvetsky, and A. F. Vakakis, "New family of solitary waves in granular dimer chains with no precompression," *Phys. Rev. E*, vol. 83, p. 036606, 2011.

[73] C. Daraio, V. F. Nesterenko, E. B. Herbold, and S. Jin, "Strongly nonlinear waves in a chain of teflon beads," *Phys. Rev. E*, vol. 72, no. 016603, 2005.

[74] C. Daraio and V. F. Nesterenko, "Strongly nonlinear wave dynamics in a chain of polymer coated beads," *Phys. Rev. E*, vol. 73, no. 026612, 2006.

[75] D. Khatri, C. Daraio, and P. Rizzo, "Coupling of highly nonlinear waves with linear elastic media," *Proc. SPIE*, vol. 6934, no. 69340U, 2008.

[76] R. Carretero-González, D. Khatri, M. Porter, P. Kevrekidis, and C. Daraio, "Dissipative solitary waves in granular crystals," *Phys. Rev. Lett.*, vol. 102, no. 024102, 2009.

[77] C. Daraio, D. Ngo, V. F. Nesterenko, and F. Fraternali, "Highly nonlinear pulse splitting and recombination in a two-dimensional granular network," *Phys. Rev. E*, vol. 82, p. 036603, 2010.

[78] A. Spadoni and C. Daraio, "Generation and control of sound bullets with a nonlinear acoustic lens," *Proc. Natl. Acad. Sci. USA*, vol. 107, no. 7230, 2010.

[79] A. C. Hladky-Hennion and M. de Billy, "Experimental validation of band gaps and localization in a one-dimensional diatomic phononic crystal," *J. Acoust. Soc. Am.*, vol. 122, no. 2594, 2007.

[80] A.-C. Hladky-Hennion, J. Vasseur, B. Djafari-Rouhani, and M. de Billy, "Sonic band gaps in one-dimensional phononic crystals with a symmetric stub," *Phys. Rev. B*, vol. 77, p. 104304, 2008.

[81] N. Boechler and C. Daraio, "An experimental investigation of acoustic band gaps and localization in granular elastic chains," *ASME Conference Proceedings*, vol. 2009, no. 48982, pp. 271–276, 2009.

[82] N. Boechler, J. Yang, G. Theocharis, P. G. Kevrekidis, and C. Daraio, "Tunable vibrational band gaps in one-dimensional diatomic granular crystals with three-particle unit cells," *Journal of Applied Physics*, vol. 109, no. 7, p. 074906, 2011.

[83] A. J. Sievers and S. Takeno, "Intrinsic localized modes in anharmonic crystals," *Phys. Rev. Lett.*, vol. 61, pp. 970–973, 1988.

[84] S. Takeno, K. Kisoda, and A. J. Sievers, "Intrinsic localized vibrational modes in anharmonic crystals: Stationary modes," *Progress of Theoretical Physics Supplement*, vol. 94, no. Supplement 1, pp. 242–269, 1988.

[85] J. B. Page, "Asymptotic solutions for localized vibrational modes in strongly anharmonic periodic systems," *Phys. Rev. B*, vol. 41, pp. 7835–7838, 1990.

[86] R. S. MacKay and S. Aubry, "Proof of existence of breathers for time-reversible or hamiltonian networks of weakly coupled oscillators," *Nonlinearity*, vol. 7, no. 1623, 1994.

[87] C. Hoogeboom, G. Theocharis, and P. G. Kevrekidis, "Discrete breathers at the interface between a diatomic and a monoatomic granular chain," *Phys. Rev. E*, vol. 82, p. 061303, 2010.

[88] Y. B. Jeon, R. Sood, J. H. Jeong, and S. G. Kim, "Mems power generator with transverse mode thin film PZT," *Sensors and Actuators A: Physical*, vol. 122, no. 16, 2005.

[89] F. Cottone, H. Vocca, and L. Gammaitoni, "Nonlinear energy harvesting," *Phys. Rev. Lett.*, vol. 102, p. 080601, 2009.

[90] H. Rossmanith and A. Shukla, "Photoelastic investigation of dynamic load transfer in granular media," *Acta Mechanica*, vol. 42, pp. 211–225, 1982.

[91] A. Shuckla, M. H. Sadd, Y. Xu, and Q. M. Tai, "Influence of loading pulse duration on dynamic load transfer in a simulated granular medium," *J. Mech. Phys. Solids*, vol. 41, no. 11, 1993.

[92] A. Shuckla, C. Y. Zhu, and M. H. Sadd, “Angular dependence of dynamic load transfer due to explosive loading in granular aggregate chains,” *Journal of Strain Analysis*, vol. 23, no. 3, 1988.

[93] A. Shukla, M. H. Sadd, R. Singh, Q. Tai, and S. Vishwanathan, “Role of particle shape and contact profile on the dynamic response of particulate materials,” *Optics and Lasers in Engineering*, vol. 19, no. 1-3, pp. 99 – 119, 1993.

[94] R. Singh, A. Shukla, and H. Zervas, “Effect of flaws on the stress wave propagation in particulate aggregates: Near and far field observations,” *International Journal of Solids and Structures*, vol. 32, no. 17-18, pp. 2523 – 2546, 1995.

[95] S. G. Bardenhagen and J. U. Brackbill, “Dynamic stress bridging in granular material,” *Journal of Applied Physics*, vol. 83, no. 11, pp. 5732–5740, 1998.

[96] R. Mindlin, “Compliance of elastic bodies in contact,” *J. Appl. Mech.*, vol. 16, pp. 259–268, 1949.

[97] B. Velický and C. Caroli, “Pressure dependence of the sound velocity in a two-dimensional lattice of Hertz-Mindlin balls: Mean-field description,” *Phys. Rev. E*, vol. 65, p. 021307, 2002.

[98] C. Coste and B. Gilles, “Sound propagation in a constrained lattice of beads: High-frequency behavior and dispersion relation,” *Phys. Rev. E*, vol. 77, p. 021302, 2008.

[99] B. Gilles and C. Coste, “Low-frequency behavior of beads constrained on a lattice,” *Phys. Rev. Lett.*, vol. 90, p. 174302, 2003.

[100] K. T. M. Nishida and T. Ishida, “Dem simulation of wave propagation in two-dimensional ordered array of particles,” vol. 26, pp. 815–820, 2009.

[101] M. Nishida and Y. Tanaka, “Dem simulations and experiments for projectile impacting two-dimensional particle packings including dissimilar material layers,” *Granular Matter*, vol. 12, pp. 357–368, 2010.

[102] A. Leonard, F. Fraternali, and C. Daraio, "Directional wave propagation in a highly nonlinear square packing of spheres," *Experimental Mechanics*, pp. 1–11, 2011.

[103] A. Leonard and C. Daraio, "Stress wave anisotropy in centered square highly nonlinear granular systems," *Phys. Rev. Lett.*, vol. 108, p. 214301, 2012.

[104] Ball-tec, http://www.precisionballs.com/.

[105] E. Hinch and S. Saint-Jean, "The fragmentation of a line of balls by an impact," *Proc. R. Soc. Lond. A*, vol. 455, pp. 3201–3220, 1999.

[106] Y. Zhu, A. Shukla, and M. H. Sadd, "The effect of microstructural fabric on dynamic load transfer in two dimensional assemblies of elliptical particles," *Journal of the Mechanics and Physics of Solids*, vol. 44, no. 8, pp. 1283 – 1303, 1996.

[107] N. Newmark, *A Method of Computation for Structural Dynamics.* American Society of Civil Engineers, 1959.

[108] T. J. R. Hughes, *The Finite Element Method: Linear Static and Dynamic Finite Element Analysis.* New York: Dover Publications, 2000.

[109] S. Luding, E. Clément, A. Blumen, J. Rajchenbach, and J. Duran, "Studies of columns of beads under external vibrations," *Phys. Rev. E*, vol. 49, pp. 1634–1646, 1994.

[110] S. Luding, H. J. Herrmann, and A. Blumen, "Simulations of two-dimensional arrays of beads under external vibrations: Scaling behavior," *Phys. Rev. E*, vol. 50, pp. 3100–3108, 1994.

[111] W. A. M. Morgado and I. Oppenheim, "Energy dissipation for quasielastic granular particle collisions," *Phys. Rev. E*, vol. 55, pp. 1940–1945, 1997.

[112] N. V. Brilliantov, F. Spahn, J.-M. Hertzsch, and T. Pöschel, "Model for collisions in granular gases," *Phys. Rev. E*, vol. 53, pp. 5382–5392, 1996.

[113] S. McNamara and E. Falcon, "Simulations of vibrated granular medium with impact-velocity-dependent restitution coefficient," *Phys. Rev. E*, vol. 71, p. 031302, 2005.

[114] A. Rosas, J. Buceta, and K. Lindenberg, "Dynamics of two granules," *Phys. Rev. E*, vol. 68, p. 021303, 2003.

[115] E. B. Herbold and V. F. Nesterenko, "Shock wave structure in a strongly nonlinear lattice with viscous dissipation," *Phys. Rev. E*, vol. 75, p. 021304, 2007.

[116] E. Falcon, C. Laroche, S. Fauve, and C. Coste, "Behavior of one inelastic ball bouncing repeatedly off the ground," *The European Physical Journal B - Condensed Matter and Complex Systems*, vol. 3, no. 1, pp. 45–57, 1998.

[117] R. Mindlin and H. Deresiewicz, "Elastic spheres in contact under varying oblique forces," *J. Appl. Mech.*, vol. 20, pp. 327–344, 1953.

[118] K. Duffaut, M. Landr, and R. Sollie, "Using mindlin theory to model friction-dependent shear modulus in granular media," *GEOPHYSICS*, vol. 75, no. 3, pp. E143–E152, 2010.

[119] V. Nesterenko, A. Lazaridi, and E. Sibiryakov, "The decay of soliton at the contact of two acoustic vacuums," *Journal of Applied Mechanics and Technical Physics*, vol. 36, pp. 166–168, 1995.

[120] L. Vergara, "Scattering of solitary waves from interfaces in granular media," *Phys. Rev. Lett.*, vol. 95, p. 108002, 2005.

[121] I. Szelengowicz, P. G. Kevrekidis, and C. Daraio, "Wave propagation in square granular crystals with spherical interstitial intruders," *Phys. Rev. E*, vol. 86, p. 061306, 2012.

[122] A. Leonard, A. Aswathi, P. Guebelle, and C. Daraio, "Tailoring stress waves in 2-D highly nonlinear granular crystals: Simulations and experiments," pp. 148–194, 2011.

[123] G. T. N. Boechler and D. C., “Bifurcation-based acoustic switching and rectification,” *Nat. Mater.*, vol. 10, pp. 665–668, 2011.

[124] M. Hasan, Y. Starosvetsky, A. Vakakis, and L. Manevitch, “Nonlinear targeted energy transfer and macroscopic analogue of the quantum landauzener effect in coupled granular chains,” *Physica D: Nonlinear Phenomena*, no. 0, pp. –, 2013.

[125] Y. Starosvetsky, M. Hasan, A. Vakakis, and L. Manevitch, “Nonlinear pulse equipartition in weakly coupled ordered granular chains with no precompression,” *J. Comp. Nonlinear Dyn.*, vol. 8, no. 3, p. 034504, to be published.

[126] Y. Starosvetsky, M. Hasan, A. Vakakis, and L. Manevitch, “Strongly nonlinear beat phenomena and energy exchanges in weakly coupled granular chains on elastic foundations,” *SIAM Journal on Applied Mathematics*, vol. 72, no. 1, pp. 337–361, 2012.

[127] P. Kevrekidis and B. Malomed, “Solitons in coupled toda lattices,” *Physics Letters A*, vol. 303, no. 56, pp. 328 – 336, 2002.

[128] Y. Jiang, B. Tian, W.-J. Liu, K. Sun, M. Li, and P. Wang, “Soliton interactions and complexes for coupled nonlinear Schrödinger equations,” *Phys. Rev. E*, vol. 85, p. 036605, 2012.

[129] A. Trombettoni, H. Nistazakis, Z. Rapti, D. Frantzeskakis, and P. Kevrekidis, “Soliton dynamics in linearly coupled discrete nonlinear Schrödinger equations,” *Mathematics and Computers in Simulation*, vol. 80, no. 4, pp. 814 – 824, 2009.

[130] B. A. Malomed and J. Yang, “Solitons in coupled Ablowitz-Ladik chains,” *Physics Letters A*, vol. 302, no. 4, pp. 163 – 170, 2002.

[131] I. Szelengowicz, M. A. Hasan, Y. Starosvetsky, A. Vakakis, and C. Daraio, “Energy equipartition in two-dimensional granular systems with spherical intruders,” *Phys. Rev. E*, vol. 87, p. 032204, 2013.

[132] M. P. Bendsøe and N. Kikuchi, “Generating optimal topologies in structural design using a homogenization method,” *Computer Methods in Applied Mechanics and Engineering*, vol. 71, no. 2, pp. 197 – 224, 1988.

[133] M. Bendsøe, “Optimal shape design as a material distribution problem,” *Struct. Optim.*, vol. 1, pp. 193–202, 1989.

[134] M. Zhou and G. Rozvany, “The COC algorithm, part II: Topological geometrical and generalized shape optimization,” *Comput. Meth. Appl. Mechs. Eng.*, vol. 89, pp. 309–336, 1991.

[135] M. Fuchs, S. Jiny, and N. Peleg, “The srv constraint for 0/1 topological design,” *Structural and Multidisciplinary Optimization*, pp. 320–326, 2005.

[136] X. Zhou, L. Chen, and Z. Huang, “The simp-srv method for stiffness topology optimization of continuum structures,” *International Journal of CAD/CAM*, vol. 7, 2007.

[137] O. Sigmund and S. Torquato, “Design of materials with extreme thermal expansion using a three-phase topology optimization method,” *Journal of the Mechanics and Physics of Solids*, vol. 45, no. 6, pp. 1037 – 1067, 1997.

[138] D. Tortorelli and P. Michaleris, “Design sensitivity analysis: overview and review,” *Inverse Problems in Engineering*, vol. 1, pp. 71–103, 1994.

[139] M. Silva, P. B. Nakshatrala, and D. A. Tortorelli, “A robust topology optimization approach to energy tailoring,” *International Journal of Solid and Structures*, (to be published).

[140] P. J. Wang, J. H. Xia, Y. D. Li, and C. S. Liu, “Crossover in the power-law behavior of confined energy in a composite granular chain,” *Phys. Rev. E*, vol. 76, p. 041305, 2007.

[141] T. Back and H.-P. Schwefel, “Evolutionary computation: an overview,” in *Evolutionary Computation, 1996., Proceedings of IEEE International Conference on*, pp. 20 –29, 1996.

[142] L. J. Fogel, A. J. Owens, and M. J. Walsh, *Artificial Intelligence through Simulated Evolution.* New York: John Wiley, 1966.

[143] D. E. Goldberg and J. H. Holland, “Genetic algorithms and machine learning,” *Machine Learning*, vol. 3, pp. 95–99, 1988.

[144] J. H. Holland, “Outline for a logical theory of adaptive systems,” *J. ACM*, vol. 9, no. 3, pp. 297–314, 1962.

[145] M. Mitchell and S. Forrest, “Genetic algorithms and artificial life,” *Artificial Life*, vol. 1, pp. 267–289, 1994.

[146] H. Mühlenbein and D. Schlierkamp-Voosen, “Predictive models for the breeder genetic algorithm i. continuous parameter optimization,” *Evolutionay Computation*, vol. 1, pp. 25–49, 1993.

[147] H. Mühlenbein and D. Schlierkamp-Voosen, “The science of breeding and its application to the breeder genetic algorithm (bga),” *Evolutionay Computation*, vol. 1, pp. 335–360, 1993.

[148] R. Balling, “Optimal steel frame design by simulated annealing,” *Journal of Structural Engineering*, vol. 117, no. 6, pp. 1780–1795, 1991.

[149] P. Y. Shim and S. Manoocherhri, “Generating optimal configurations in structural design using simulated annealing,” *International Journal for Numerical Methods in Engineering*, vol. 40, no. 6, pp. 1053–1069, 1997.

[150] W. Jenkins, “Plane frame optimum design environment based on genetic algorithm,” *Journal of Structural Engineering*, vol. 118, no. 11, pp. 3103–3112, 1992.

[151] P. Hajela, E. Lee, and C.-Y. Lin, "Genetic algorithms in structural topology optimization," in *Topology Design of Structures* (M. Bendse and C. Soares, eds.), vol. 227 of *NATO ASI Series*, pp. 117–133, Springer Netherlands, 1993.

[152] S. Rajan, "Sizing, shape, and topology design optimization of trusses using genetic algorithm," *Journal of Structural Engineering*, vol. 121, no. 10, pp. 1480–1487, 1995.

[153] D. Goldberg and M. Samtani, "Engineering optimization via genetic algorithm," in *Proc. 9th Conf. Electronic Conputation, ASCE*, pp. 471–482, 1986.

[154] C. Chapman, K. Saitou, and M. Jakiela, "Genetic algorithms as an approach to configuration and topology design," *J. Mech. Design*, vol. 116, pp. 1005–1012, 1994.

[155] G. Steven, O. Querin, and M. Xie, "Evolutionary structural optimisation (eso) for combined topology and size optimization of discrete structures," *Comput. Methods Appl. Mech. Eng.*, vol. 188, pp. 743–754, 2000.

[156] R. Kicinger, T. Arciszewski, and K. D. Jong, "Evolutionary computation and structural design: A survey of the state-of-the-art," *Comput. Struct.*, vol. 83, no. 23-24, pp. 1943–1978, 2005.

[157] I. D. Falco, R. D. Balio, A. D. Cioppa, and E. Tarantino, "A comparative analysis of evolutionary algorithms for function optimisation," *Comput. Struct.*, vol. 83, no. 23-24, pp. 1943–1978, 2005.

[158] I. D. Falco, R. D. Balio, A. D. Cioppa, and E. Tarantino, "Optimising constrained continuous multivariable functions with breeder genetic algorithms," *Journal of Evolutionary Optimization*, vol. 1, no. 1, pp. 53–64, 1999.

[159] K. De Jong, "Evolutionary computation: a unified approach," in *Proceedings of the 2007 GECCO conference companion on Genetic and evolutionary computation*, GECCO '07, (New York, NY, USA), pp. 3158–3171, ACM, 2007.

[160] H. Mlejnek, "Some aspects of the genesis of structures," *Structural optimization*, vol. 5, pp. 64–69, 1992.

[161] G. D. Wang M., Wang X., "A level set method for structural topology optimization," *Comput. Methods Appl. Mech. Eng.*, vol. 192, no. 1-2, pp. 227–246, 2003.

[162] G. Allaire, F. de Gournay, F. Jouve, and A. Toader, "Structural optimization using topological and shape sensitivity via a level set method," Internal report 555, Ecole Polytechnique, 2004.

[163] M. Xie and G. P. Steven, *Evolutionary structural optimisation.* Springer-Berlin, 1997.